2010

Experimental and numerical analysis of fuel cells

Abul Bashar Mahmud Hasan
Louisiana State University and Agricultural and Mechanical College

EXPERIMENTAL AND NUMERICAL ANALYSIS OF FUEL CELLS

A Dissertation

Submitted to the Graduate Faculty of the
Louisiana State University and
Agricultural & Mechanical College
in partial fulfillment of the
requirements for the degree of
Doctor of Philosophy

in

The Interdepartmental Program in
Engineering Science

by
Abul Bashar Mahmud Hasan
B.S., Bangladesh University of Engineering & Technology (BUET), 2001
M.S., LSU, 2005
M.Eng., Virginia Tech, 2007

May, 2010

ACKNOWLEDGMENTS

I would like to express my deepest and most sincere gratitude to my supervisor Dr. M. A. Wahab, Associate Professor, Mechanical Engineering Department, LSU for his continuous guidance, encouragement, and sharing valuable time throughout the work. It is also much pleasure to acknowledge his untiring help by supplying valuable references, information and financial support, without which this work could not have been completed.

I am grateful to Dr. S.M.Guo, Associate Professor, Mechanical Engineering Department, LSU, co-chair of my advisory committee for his active mentorship and constant encouragement. With his knowledge, experience, and research capabilities he continuously guided me towards my goal of completing this work.

It has been my cherished honor to work with such brilliant, considerate, and friendly scholars. My thanks to my two advisors cannot be enough in mere words. I shall always remember my learning from them.

I would like to thank Dr. Guoqiang Li, Associate Professor of Mechanical Engineering Department, Dr. Li-yeng Sung, Professor of Mathematics Department (minor committee member), and Dr. Donghui Zhang, Assistant Professor of Chemistry Department (Dean's Representative) for serving in Graduate Advisory Committee and their valuable comments and suggestions, which have certainly improved the quality of this work. I also appreciate and acknowledge Dr. Ekkad and Dr. Ellis for serving in my master's committee.

I extend my gratitude to my wife Dr. Samia Sharmin Hoque for her sincere encouragement and inspiration that enabled me to complete my research work in a foreign country. I appreciate her affectionate support and patience.

I greatly acknowledge for the financial support of this work by NASA/EPSCoR grant under

grant number NASA/LEQSF (2007-10)-Phase3-01.

This work is dedicated to my father Late Alhaj Md. Habibur Rahman who always inspired me and unfortunately, passed away in the beginning of my PhD study at LSU.

TABLE OF CONTENTS

ACKNOWLEDGEMENTS ii

LIST OF TABLES vi

LIST OF FIGURES vii

NOMENCLATURE xiii

ABSTRACT xix

CHAPTER-1: INTRODUCTION 1
1.1 Fuel Cells Overview 1
1.2 History of Fuel Cell 2
1.3 Components of Fuel Cell 3
1.4 Fuel Cell Chemistry 3
1.5 Types of Fuel Cell 4
1.5.1 Proton Exchange Membrane Fuel Cell (PEMFC) 4
1.5.2 Solid Oxide Fuel Cell (SOFC) 5
1.5.2.1 Working Principle of Fuel Cell 6
1.5.3 Alkaline Fuel Cell (AFC) 7
1.5.4 Phosphoric Acid Fuel Cell (PAFC) 8
1.5.5 Molten Carbonate Fuel Cell (MCFC) 8
1.5.6 Direct Methanol Fuel Cell (DMFC) 9
1.5.7 Biological Fuel Cell 10
1.6 Fuel Cell Numerical Analysis 15
1.7 Research Objectives 16
1.8 Scope of the Dissertation 17

CHAPTER-2: LITERATURE SURVEY 18
2.1 Fuel Cell Operation and Experimental Analysis 18
2.1.1 Application of APS to SOFC Manufacturing 18
2.1.2 Anode and Cathode Adhesion with Electrolyte Membrane 28
2.1.3 Gas Flow Channel Configurations 30
2.1.4 PEMFC Poisoning and Recovery 33
2.2 Numerical Analysis 33
2.2.1 Single Channel Analysis 33
2.2.2 Transient Temperature during Pulse Heating in Fuel Cell Poisoning Analysis 35
2.2.3 Thermal Stress in SOFC Fabrication 36
2.2.4 Liquid Droplet Dispersion at the Interface of GDL-GFC 37
2.3 Conclusion of Literature Survey 45

CHAPTER-3: FUEL CELL OPERATION AND EXPERIMENTAL ANALYSIS 47
3.1 Application of APS to SOFC Manufacturing 47

3.2 Anode and Cathode Adhesion with Electrolyte Membrane 50
3.2.1 Conclusion on Anode and Cathode Adhesion with Electrolyte Membrane 73
3.3 Gas Flow Channel Configurations 73
3.3.1 Conclusion on Gas Flow Channel Configurations 82
3.4 PEMFC Poisoning and Recovery 82
3.4.1 Conclusion on PEMFC Poisoning and Recovery 89

CHAPTER-4: FUEL CELL NUMERICAL ANALYSIS 91
4.1 PEMFC Single Channel 91
4.1.1 Conclusion on PEMFC Single Channel 108
4.2 Transient Temperature during Pulse Heating in Fuel Cell Poisoning Analysis 108
4.3 Thermal Stress in SOFC Fabrication 110
4.3.1 Conclusion on Thermal Stress in SOFC Fabrication 119
4.4 Liquid Droplet Dispersion at the Interface of GDL-GFC 119
4.4.1 Conclusion on Liquid Droplet Dispersion at the Interface of GDL-GFC 143

CHAPTER-5: CONCLUSIONS 144

CHAPTER-6: RECOMMENDATIONS FOR FUTURE WORK 147

REFERENCES 149

APPENDIX-A:PERMISSION 160

APPENDIX-B:LIST OF PUBLICATIONS ARISING FROM THIS RESEARCH 163

VITA 164

LIST OF TABLES

Table 3.1: Bonding strength data 59

Table 3.2: Grit size relation with average particle diameter 65

Table 3.3: Ni etchant 66

Table 3.4: Al etchant 67

Table 3.5: Low carbon steel mechanical characteristics 67

Table 3.6: Low carbon steel specifications 67

Table 3.7: Velocity, Reynolds number and total pressure loss data for various reactants and bipolar plates 80

Table 3.8: Water flooding in the cathode side gas flow channels for various gas flow channel configurations 81

Table 4.1: HTVTF design parameters by MTI Corporation manual 112

Table 4.2: Constants and parameters used in simulation 114

Table 4.3: Electrochemical data 126

Table 4.4: Physical property data 127

Table 4.5: Inlet conditions 128

Table 4.6: Constants used in simulation 132

LIST OF FIGURES

Figure 1.1: Fuel cell with gas flow channel by Fuel Cell Technologies 2

Figure 1.2: MEA (Membrane Electrode Assembly) 3

Figure 1.3: Working stage of a Proton Exchange Membrane Fuel Cell 4

Figure 1.4: Details working stage of a Proton Exchange Membrane Fuel Cell 5

Figure 1.5: Working stage of a SOFC 7

Figure 1.6: Working stage of an AFC (Alkaline Fuel Cell) 8

Figure 1.7: MCFC (Molten carbonate fuel cell) 9

Figure 2.1: Air bleeding effect on PEMFC CO poisoning (left) & recovery (right) process, 3000 ppm CO at a 61.8 μmol dose 33

Figure 2.2: Normalized PEMFC (i_{CO-H2}/i_{H2}) performance at different temperatures, based on 35

Figure 3.1: Electrospinning 47

Figure 3.2: YSZ(yttrium stabilized zirconia) cloth made by electrospinning 48

Figure 3.3: Atmospheric plasma spray 48

Figure 3.4: Manufactured alumina using APS 48

Figure 3.5: XRD machines to analyze crystalline structure 49

Figure 3.6: XRD of Al_2O_3 powder 49

Figure 3.7: XRD of Al_2O_3 thin film after APS 50

Figure 3.8: ZrO_2 powder 50

Figure 3.9: Lap shear 51

Figure 3.10: Butt joint 52

Figure 3.11: Clevage 52

Figure 3.12: Blister 52

Figure 3.13: Peel 53
Figure 3.14: Peel test 53
Figure 3.15: Before application of APS ceramic coating (microfeatures above substrate) 54
Figure 3.16: After application of ceramic coating (microfeatures above substrate) 54
Figure 3.17: Before application of APS ceramic coating (microfeatures as Groove) 54
Figure 3.18: After application of ceramic coating (microfeatures as groove) 54
Figure 3.19: Dog bone sample with microfeatures over/grooved surface 54
Figure 3.20: Fixture for pull test 55
Figure 3.21: Photolithography techniques 56
Figure 3.22: Cylindrical fixture for pull test 57
Figure 3.23: Process of photolithography positive photoresist for making groove 58
Figure 3.24: Photomask drawing by AutoCAD2008 60
Figure 3.25: AutoCAD drawing after conversion for pattern generator 60
Figure 3.26: Photomask from Nanofilm 60
Figure 3.27: Pattern generator for pattern making 61
Figure 3.28: Hood for developing mask 61
Figure 3.29: Spinner for uniform photoresist making 61
Figure 3.30: Photoresist 61
Figure 3.31: Hot plate station 62
Figure 3.32: Convection oven 62
Figure 3.33: UV exposure station 62
Figure 3.34: Acid station for etching 62
Figure 3.35: Microscopic observation 63

Figure 3.36: Microscopic view of 10 microns square photomask 63

Figure 3.37: Actual design with 5 microns square patterns 64

Figure 3.38: Bench top hand grinding machine 64

Figure 3.39: Drum type bench top grinding machine 64

Figure 3.40: Ni and Al etchants 66

Figure 3.41: Al and MS rod before and after etching 68

Figure 3.42: Al foil before and after etching 68

Figure 3.43: Al plate before and after etching 69

Figure 3.44: MS dog bone and plate etching 70

Figure 3.45: Roughness value 70

Figure 3.46: 10 microns groove over Al substrate plate (10X magnification) 71

Figure 3.47: 10 microns groove over Al substrate plate (25X magnification) 71

Figure 3.48: Stylus probe to measure roughness of substrate 72

Figure 3.49: Stylus profiler is used for surface roughness 72

Figure 3.50: MTS testing machine 72

Figure 3.51: (a) Interdigitated (b) Serpentine (c) Straight bipolar plate 74

Figure 3.52: Test station 75

Figure 3.53: Voltage versus current density curve for Serpentine-Serpentine gas flow channel configuration under different hydrogen flow rates at 21°C 78

Figure 3.54: V-I curve at 20 sccm H_2 flow rate using different gas flow channel configurations .. 79

Figure 3.55: V-I curve under 60 sccm H_2 flow rate for different gas flow channel configurations 79

Figure 3.56: V-I curve under 80 sccm H_2 flow rate for different gas flow channel configurations 80

Figure 3.57: Water flooding patterns of cathode side bipolar plates 81

Figure 3.58: Experimental result for Voltage vs. Current Density curve for various flow rates for the single channel test cell 82

Figure 3.59: The design concept of the embedded heating device 84

Figure 3.60: BOPP stainless Mesh and the schematic test setup 84

Figure 3.61: Fuel Cell with mesh heater in operating condition 85

Figure 3.62: Power Density versus current Density curve using pure hydrogen 86

Figure 3.63: Voltage versus current density curve using pure hydrogen 86

Figure 3.64: Performance of PEMFC using 100ppm and 1000ppm CO concentration H_2 under fuel flow rates of 20 sccm and 40 sccm 87

Figure 3.65: PEMFC poisoning and recovery due to pulsed heating (3 pulses at ~80s, 128s and 152s) 87

Figure 3.66: PEMFC Poisoning and recovery due to pulsed feeding 88

Figure 3.67: Poisoning and recovery of PEMFC due to pulsed feeding 88

Figure 4.1: Meshing of the single channel model 102

Figure 4.2: 3D Simulation, (a) water pattern indicated by water mass fraction, (b)hydrogen partial pressure, P_{H2}(bar) at 0.5V 102

Figure 4.3: 3D Simulation, (a) water pattern indicated by water mass fraction, (b) hydrogen Partial pressure, P_{H2}(bar), at 0.7V 103

Figure 4.4: Simulation of (a) water pattern indicated by water mass fraction (b) Hydrogen partial pressure, P_{H2}(bar) at 0.9V 103

Figure 4.5: Water mass fraction along the channel 104

Figure 4.6: Grid of 2D model 105

Figure 4.7: 2D numerical simulation of water pattern for 20sccm hydrogen flow rate at 0.7V with contour lines 106

Figure 4.8: Voltage vs. Current Density curve for 2D and 3D simulation result for a 20sccm hydrogen flow rates 106

Figure 4.9: Simulation of Voltage vs. Current Density curve for various hydrogen flow rates .. 107

Figure 4.10: Comparison of experimental and simulation result of Voltage vs. Current Density data for 20 sccm hydrogen flow rate for one channel 107

Figure 4.11: Membrane and catalyst temperature (T) rise at 10 ms under $2x10^6$ W/m^2 heating pulse 109

Figure 4.12: HTVTF showing different parts (from MTI corporation, Inc.) 111

Figure 4.13: Various components of HTVTF 111

Figure 4.14: Fractured tube with actual tube in front of the HTVTF 112

Figure 4.15: Vacuum tube furnace with porous blocks inside tube geometry at both entrances 113

Figure 4.16: Meshing of the different furnace domains 114

Figure 4.17: Temperature profile due to natural convection inside the furnace without porous cylindrical alumina blocks 115

Figure 4.18: Temperature profile with cylindrical blocks and no inlet gas flow condition 116

Figure 4.19: Experimental and simulation result of inside temperature of the tube between HAZs 117

Figure 4.20: Temperature profile for the furnace while a small copper pipe is inserted inside the block 118

Figure 4.21: Fuel cell geometry 120

Figure 4.22: Polarization curve of PEMFC 128

Figure 4.23: Effect of saturation (s) as well as porosity (ε) on polarization curve 129

Figure 4.24: Diagram of 2D finite element GDL showing boundary conditions 133

Figure 4.25: Saturation plot for $s = 0$ for constant capillary pressure slope 135

Figure 4.26: Saturation plot for $s = 0.05$ for constant capillary pressure slope 135

Figure 4.27: Saturation plot for $s = 0.25$ for constant capillary pressure slope 136

Figure 4.28: Saturation plot for $s = 0.5$ for constant capillary pressure slope 136

Figure 4.29: Liquid water flux inside GDL for $s = 0.5$ at the interface of GDL-GFC using varying capillary pressure slope 137

Figure 4.30: Saturation distribution inside GDL for $s = 0.05$ using varying capillary pressure slope 138

Figure 4.31: Saturation plot for $s = 0.5$ for constant capillary pressure slope 138

Figure 4.32: Saturation distribution inside GDL for $s = 0.5$ using varying capillary pressure slope 139

Figure 4.33: Saturation plot with contour plot for a periodic function for constant capillary pressure slope 139

Figure 4.34: Saturation plot for a periodic function of s at the interface of GDL-GFC with contour plot using varying capillary pressure slope 140

Figure 4.35: Saturation inside GDL for periodic boundary condition at the interface of GDL-GFC (a) constant (b) varying capillary slope 142

NOMENCLATURE

Notations	Meaning
1D	one dimension
2D	two dimension
3D	three dimension
α	thermal expansion coefficient of alumina tube
ACL	anode catalyst layer
AFC	alkaline fuel cell
Al	aluminum
Al_2O_3	alumina
amp	ampere
APS	atmospheric plasma spray
B-V	Butler-Volmer equation
C	centigrade
c^{ref}	dissolved gas concentration at a reference state
c^{agg}	dissolved gas concentration at the surface of the agglomerates
CCL	cathode catalyst layer
CL	catalyst layer
CO	carbon monoxide
$c_{p,alu\,\min}$	heat capacity of alumina
$c_{p,air}$	heat capacity of air
CO_2	carbon dioxide

c^g	total molar concentration of the gas phase
$D_{H_2H_2O}$	diffusivity of H_2 in H_2O vapor
$D_{N_2H_2O}$	diffusivity of N_2 in H_2O vapor
$D_{O_2H_2O}$	diffusivity of O_2 in H_2O vapor
$D_{O_2N_2}$	diffusivity of O_2 in N_2
D^{agg}	diffusion coefficient of the dissolved gas inside the agglomerate
δ_l	active layer thickness of the electrode
DMFC	direct methanol fuel cell
e^-	electron
ε	porosity
$E_{Alumina}$	modulus of Elasticity of alumina
$\vec{E}$	electric field intensity
F	Fahrenheit
Far	Faraday's constant
FEM	finite element method
$\Delta\phi_a$	phase potential at anode side
$\Delta\phi_c$	phase potential at cathode side
FVM	finite volume method
γ	surface tension
g	gravitational acceleration
GDL	gas diffusion layer

GDL-GFC	gas diffusion layer and gas flow channel interface
GFC	gas flow channel
H	Henry's constant
HAZ	heat affected zone
HTVTF	high temperature vacuum tube furnace
H_2	hydrogen
HOR	hydrogen oxidation reaction
H_2O	water
i	current
i_o	exchange current density
i_{oa}	exchange current density at anode side
i_{oc}	exchange current density at cathode side
κ	permeability
$\kappa_{alu\ \min,\ furnace}$	thermal conductivity of alumina in furnace
κ_p	permeability of gas diffusion layer
κ^{eff}	effective conductivity
κ_{ea}^{eff}	electronic conductivity of anode side catalyst layer
κ_{ec}^{eff}	electronic conductivity of cathode side catalyst layer
κ_{ia}^{eff}	ionic conductivity of catalyst layer in anode side
κ_{ic}^{eff}	ionic conductivity of catalyst layer in cathode side
κ_i	ionic conductivity of membrane

KOH	potassium hydroxide
LSM	lanthanum strontium manganite
MCFC	molten carbonate fuel cell
micron	10^{-6} m
MEA	membrane electrode assembly
MS	mild steel (low carbon steel)
M_{H_2}	molecular weight of hydrogen
M_{mixa}	molecular weight of mixture at anode side
M_{mixc}	molecular weight of mixture at cathode side
M_{N_2}	molecular weight of nitrogen
M_{O_2}	molecular weight of oxygen
M_{H_2O}	molecular weight of water
μ_a	viscosity of anode side gas
μ_c	viscosity of cathode side air
μ_{H_2O}	viscosity of water
n	number of electron transferred
n_{drag}	electro-osmotic drag coefficient
N_2	nitrogen
NO_x	nitrogen oxides
ORR	oxygen reduction reaction
ω_j	mass fraction of component j,

O_2	oxygen
PAFC	phosphoric acid fuel cell
ppm	parts per million
Pt	platinum
P	power density
p_{ref}	reference pressure
p_{in}	inlet pressure at anode side
PDE	partial differential equation
%	percentage
PEMFC	proton exchange membrane fuel cell
Q	sink or source term
R	universal gas constant
R^{agg}	agglomerate radius
ρ	density
$\rho_{alu\,\min}$	density of alumina
ρ_{∞}	density of air at ambient temperature
SOFC	solid oxide fuel cell
S	specific surface area of the electrode
s	saturation
s	second
sccm	standard cubic center meter
T	temperature

T_{heater}	temperature of heater
T_{ref}	reference temperature
θ	contact angle
u	velocity vector
UV	ultra violet
v	voltage
V_{ina}	anode side inlet velocity
V_{inc}	cathode side inlet velocity
W	watt
x_{H_2}	hydrogen mole fraction at anode side
x_{N_2}	mole fraction of nitrogen at cathode side
x_{O_2}	mole fraction of oxygen at cathode side
x_{H_2Oa}	mole fraction of water at anode side
x_{H_2Oc}	mole fraction of water at cathode side
XRD	X-ray diffraction
Y123	$YBa_2Cu_3O_7$ metal film
YSZ	yttrium stabilized zirconia
ZrO_2	zirconia
ζ_a	anode side stoichiometry
ζ_c	cathode side stoichiometry

ABSTRACT

Fuel Cells are attractive power source for use in electronic applications. Physical phenomena (water generation, saturation effect in fuel cell, poisoning, and thermal stress) are studied that governs the operation of a Proton Exchange Membrane Fuel Cell (PEMFC) and Solid Oxide Fuel cell (SOFC). Additionally, experimental studies and numerical simulations on PEMFC gas flow channel, the determination of the impact of the single channel fuel cell are presented. Furthermore, preliminary study is done for the application of APS (Air Plasma Spray) to SOFC and adhesion of anode and cathode with electrolytes for the determination of parameters involved in manufacturing the components of fuel cell.

The new aspects on physical phenomena are significantly different from the currently popular relationships used in fuel cells as they are simplified from simulation and experimental results. In prior work, the physical phenomena such as water generation, saturation effect in fuel cell, poisoning, and thermal stress etc. are either assumed or used as adjustment parameters to simplify them or to achieve best fits with polarization data. In this work, physical phenomena are not assumed but determined via newly developed experimental and numerical techniques.

The experimental fixtures and procedures were used to find better ways to control parameters of gas flow channel configurations for optimizing gas flow rates and performance, and gas flow channel pressure swing for CO poisoning recovery. The experimental results reveal controlling parameters for the mentioned cases and innovative design for Fuel cells.

Numerical modeling were used to 2D and later 3D for simplification of single channel fuel cell model, transient localized heating to the catalyst layer for CO recovery, thermal stress that developed during SOFC fabrication by High Temperature vacuum Tube Furnace (HTVTF), and Gas Diffusion Layer and Gas Flow Channel (GDL-GFC) interfacial conditions with results based

on commonly used relationships from the PEMFC literature. The modeling works reveal substantial impact on predicted GDL saturation, and consequently cause a significant impact on cell performance. Computational parametric relations and polarization curve results are compared to experimental polarization behavior which achieved a comparable relation.

C H A P T E R - 1

INTRODUCTION

Diminishing petrochemical oil reserves and global warming due to air pollution by carbon dioxide and unburned carbon, have initiated intensive research to identify new energy sources, more efficient technologies for energy conversion as well as clean energy. Fuel cells are one of the most promising energy conversion technologies due to a variety of approaches for producing hydrogen and the high efficiency of fuel cell systems compared to internal combustion engine. On the other hand, it is a clean or green energy to mitigate global warming.

In order to improve fuel cell performance and efficiency, it is necessary to optimize as well as understand properly the phenomena that take place in the fuel cell. In addition to experimental works, mathematical modeling is also a useful tool for improving this understanding as well as guiding fuel cell design and performance. In the present work, experimental studies and numerical simulations on Proton Exchange Fuel Cell (PEMFC) gas flow channel flows, thermal stresses in Solid Oxide Fuel Cells (SOFC), application of APS (Air Plasma Spray) to SOFC, anode and cathode adhesion with electrolyte have been conducted. In addition to these works, details analyses have been conducted on PEMFC poisoning and recovery, single gas flow channel analysis, model pulse heating and transient temperature rise in fuel cell, and modeling on thermal stress in SOFC fabrication. At the end, Independent mathematical models are also developed for gas and liquid phase transports in the Membrane Electrode Assembly (MEA) and gas diffusion media of a PEMFC. The following section will discuss components involve in fuel cell with functions of each components.

1.1 Fuel Cell Overview

In fuel cell hydrogen (H_2) and oxygen (O_2) chemical reactions forms water (H_2O), as well as electricity and heat by this process. Figure 1.1 shows simplified figure of a fuel cell with different

components. Efficiency of Hydrogen fuel cell generally varies from 50 up to 60%. This fuel cell efficiency is considerably higher than conventional power systems for many applications. The environmental impact is also lower than conventional systems because of the fuel source (hydrogen) and the relatively low operating temperature that avoids formation of NO_x.

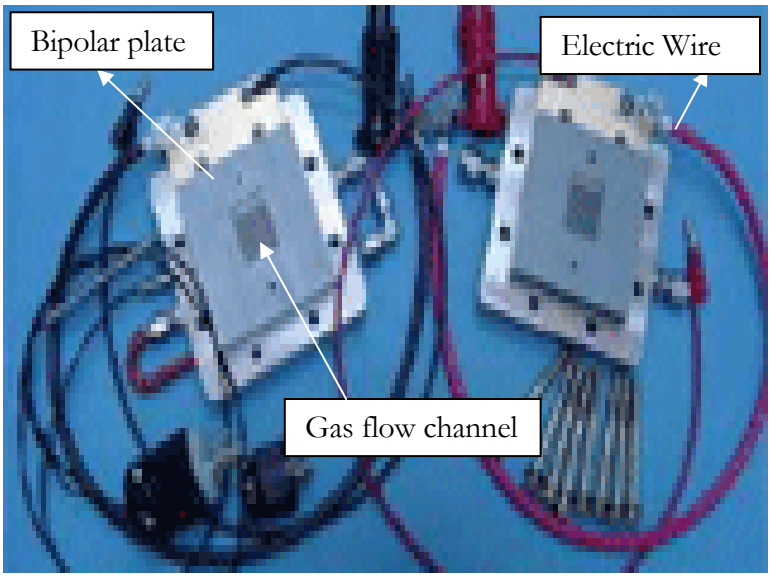

Figure 1.1: Fuel cell with gas flow channel by Fuel Cell Technologies

1.2 History of Fuel Cell

The history of fuel cell dated back from seventh century. Christian Friedrich Schönbein [Johnson Matthey plc (2007)], Swiss scientist, discovered the principle of the fuel cell in 1838 and published the principle of his idea on the January 1839 edition of the "Philosophical Magazine". Based on this work, the first fuel cell was developed by Welsh scientist Sir William Grove and a sketch of his fuel cell was published in 1843. In 1959, Bacon and his colleagues demonstrated a practical 5 kW fuel cell unit capable of powering a welding machine. Fuel cells, based on these technologies, were used in the 1960s to supply electricity during the U.S. space program. Further technological advances occurred in the period of 1980s to 1990s including the use of Nafion™ as the electrolyte as well as reductions in the quantity of expensive platinum(Pt) catalyst that is required to

manufacture fuel cell. These also help to incorporate fuel cell in automobiles application.

1.3 Components of Fuel Cell

Fuel cell is made up of gas diffusion layer (GDL) and catalyst layer (CL) on both side of electrolyte. The cell is covered by gas flow channel (GFC) also known as interconnector and bipolar plate. Gas diffusion layer, catalyst layer, and electrolyte combination known as MEA (Membrane Electrode Assembly).

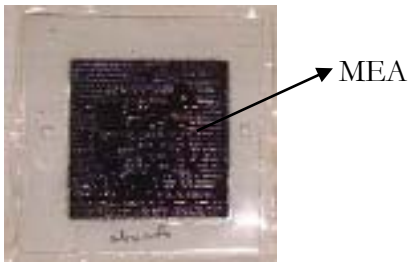

Figure 1.2: MEA (Membrane Electrode Assembly)

1.4 Fuel Cell Chemistry

In a fuel cell, hydrogen (H_2) molecules are supplied to the anode where hydrogen molecules react on the surface of a platinum catalyst. The hydrogen is oxidized into electrons and protons. The positively charged protons cross or pass the electrolyte to the cathode while the electrons pass from the anode to the cathode through an external circuit which provides power to electrical bulb. At the cathode, the platinum catalyst facilitates the reaction of electrons, protons, and oxygen (from the air), to form water. The chemical reactions for these steps are the following:

The combined reaction is:

$$2H_2 + O_2 \rightarrow 2H_2O \qquad \text{Eq. (1.1)}$$

Cathode side:

$$O_2 + 4H^+ + 4e^- \rightarrow 2H_2O \qquad \text{Eq. (1.2)}$$

Anode side:

$$2H_2 \rightarrow 4H^+ + 4e^- \qquad \text{Eq. (1.3)}$$

Although the reversible thermodynamic potential for this reaction is approximately 1.2V, however, due to irreversibilities or "overpotentials" in the cell the actual operating voltage is closer to 0.7V. To achieve useful voltage levels, multiple cells are connected in series.

1.5 Types of Fuel Cell

1.5.1 Proton Exchange Membrane Fuel Cell (PEMFC)

The PEMFC is regarded as one of the most likely to reach full-scale commercialization while considering all kinds of fuel cells. PEMFCs use a thin polymer membrane as the electrolyte. For each cell, an anode and a cathode are situated on both side of the electrolyte layer as shown in Figure 1.3. Each electrode is composed of a catalyst layer (CL) adjacent to the electrolyte and a gas diffusion layer (GDL) adjacent to the CL. The oldest and most commonly used membrane is Nafion^{TM} by Dupont. This membrane is thin and light, and it works at relatively low temperatures (about 80^0C). The catalyst layers are a mixture of carbon supported platinum catalyst and electro-

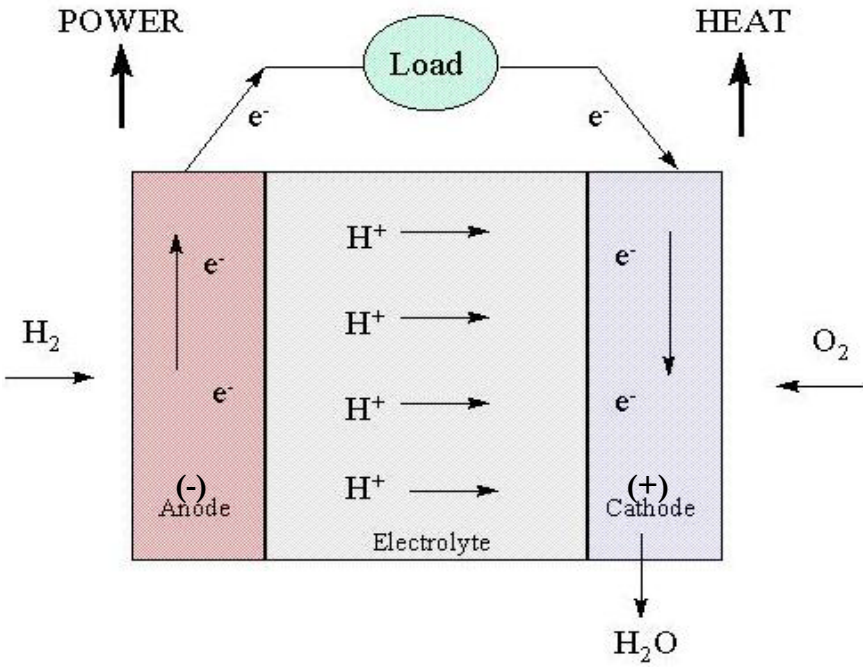

Figure 1.3: Working stage of a Proton Exchange Membrane Fuel Cell [NASA, 2007]

lyte. The GDL is a porous carbon cloth or paper. Figure 1.1 shows the essential components of a PEMFC.

PEMFCs are compact, have a low operating temperature (about 80^0C) and exhibit efficiency about 50-60 percent. For these reasons, PEMFCs are prime candidate for vehicle and portable power applications of all sizes up to mobile phones.

A Proton Exchange Fuel Cell (PEMFC), as shown in Figure 1.4, works in a similar way like other fuel cells with the exception that hydrogen ion passes through the membrane and interacts with the oxygen ion to from water and electricity. For this kind of fuel cell, water forms on cathode side, which is the opposite of other cells especially on Solid Oxide Fuel Cell (SOFC). Water droplet formation and dispersion after electrochemical reaction is a prime research area in Proton Exchange Fuel Cell (PEMFC).

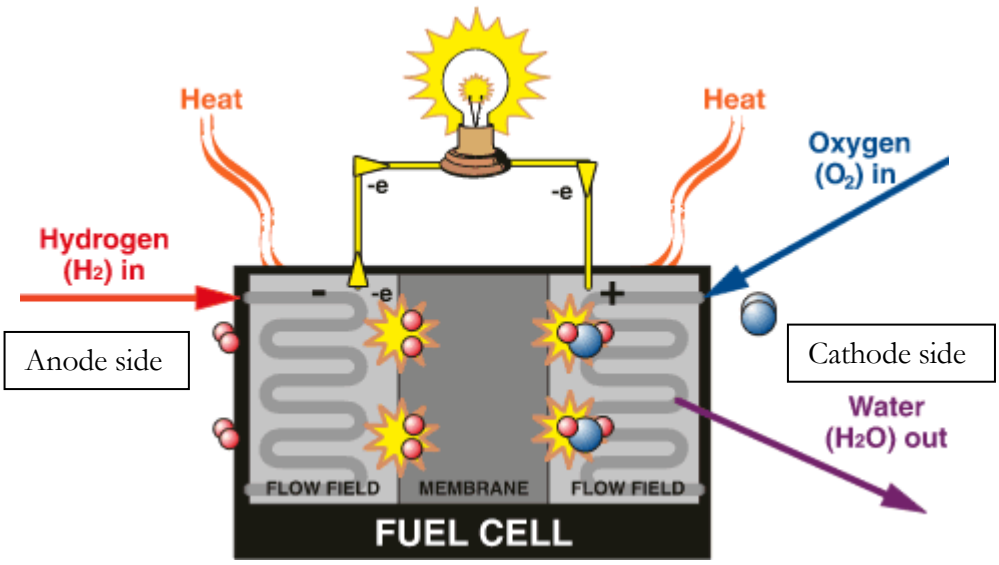

Figure 1.4: Details working stage of a Proton Exchange Fuel Cell [American History, 2007]

1.5.2 Solid Oxide Fuel Cell (SOFC)

Due to its solid electrolyte, it is known as solid oxide fuel cell. It operates at very high temperatures (nearly $1,832^0$F or $1,000^0$C). High temperature makes reliability a problem, but it also

has an advantage: the steam produced by the fuel cell, can be channeled into turbines to generate more electricity. SOFCs are suited for large-scale stationary power generators. In addition, this improves the overall efficiency of the system. Due to the high operating temperature of SOFCs, they do not need expensive catalyst to accelerate the chemical reaction.

SOFCs can have multiple geometries e.g. cylindrical (tube) and planar. SOFCs can be made in tubular geometries where either air or fuel is passed through the inside of the tube and the remaining gas is passed along the outside of the tube. The tubular design is advantageous because it is much easier to seal and separate the fuel from the air, in comparison to the planar design. The planar geometry is the typical sandwich type geometry involved by most of fuel cells where electrolyte is sandwiched in between the electrodes. The performance of the planar design is currently better than the performance of the tubular design, because the planar design has a lower resistance comparing to the tubular design.

Thermal expansion demands a uniform and slow heating process at startup that will cause very long startup duration: typically, eight (8) hours or more, although micro-tubular geometries promise much faster start up timing. Research is going on to reduce the start-up time for mobile applications. Ongoing research focuses on achieving lower-temperature of SOFC (600ºC) in order to decrease the materials cost, which will enable the use of metallic materials with better mechanical properties and thermal conductivity.

1.5.2.1 Working Principle of Fuel Cell

The Figure 1.5 represents working stage of a Fuel Cell with different stages of reactions and components formed after the reactions. This fuel cell consists of three components: (1) cathode, (2) anode, and (3) electrolyte, which is sandwiched between the two. Oxygen (O_2) from the air flows through the cathode and a fuel gas containing hydrogen (H_2) flows through the anode. Negatively

charged O_2 ions migrate through the electrolyte and react with the H_2 to form water (H_2O), which reacts with the methane (CH_4) fuel to form CO_2 and H_2. This electrochemical reaction generates electrons, which flow from the anode to an external load and back to the cathode, the final step that completes the circuit and supplies electric power. In electrochemistry, (galvanic cell) anode is where oxidation occurs and cathode is where reduction occurs. Therefore, in electrochemistry anode is negatively charged electrode and cathode is positively charged electrode.

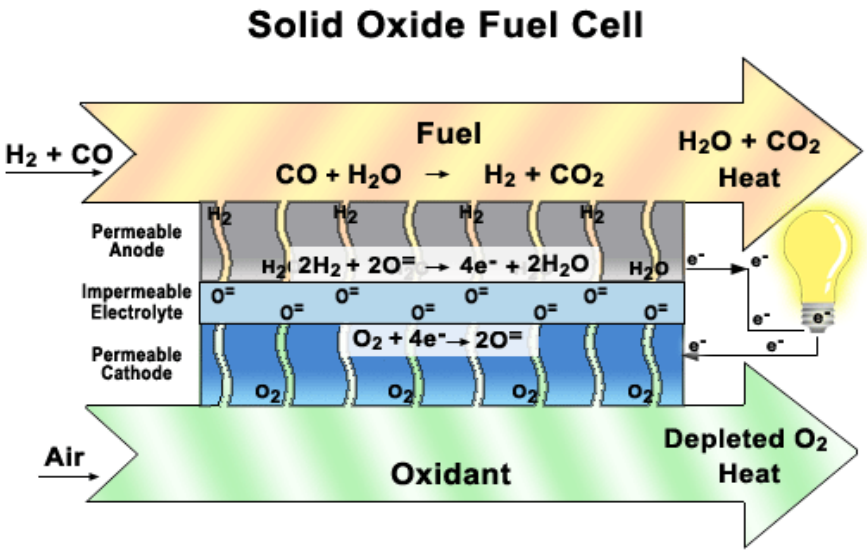

Figure 1.5: Working stages of a SOFC [CSA Company, 2005]

1.5.3 Alkaline Fuel Cell (AFC)

The AFCs consume pure hydrogen (H_2) and pure oxygen (O_2) and produce water, heat, and electricity. The two electrodes (anode and cathode) are separated by a porous matrix saturated with an aqueous alkaline solution, such as potassium hydroxide (KOH). The following figure 1.6 shows various working stages of Alkaline Fuel Cell. Aqueous alkaline solutions do not remove or reject carbon dioxide (CO_2), therefore, the fuel cell is easily poisoned by CO_2. Because of this problem, the fuel cell requires pure oxygen, or at least purified air. On the other hand, the catalyst that is required for the electrodes can be a chemical that is relatively inexpensive compared to the

Proton Exchange Membrane Fuel Cell (PEMFC). NASA has used alkaline fuel cells since the mid-1960s, during Apollo-series missions and on the Space Shuttle. It is also very expensive which hinders its commercialization. They are among the most efficient fuel cells, having the potential to reach an efficiency up to 70%.

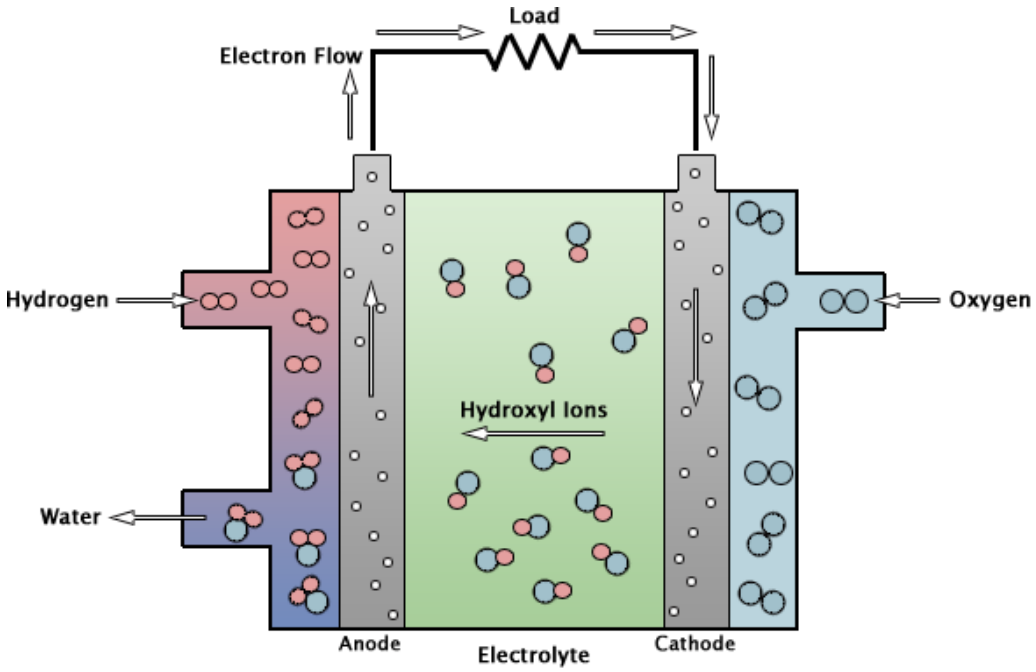

Figure 1.6: Working stage of an AFC [Wikipedia, 2009]

1.5.4 Phosphoric Acid Fuel Cell (PAFC)

The Phosphoric Acid Fuel Cell (PAFC) operates at a higher temperature than PEMFC, so it has a longer warm-up time. The PAFC is a mature technology and it is commercially available. The PAFC has all the important potentials for use in the small stationary power-generation systems. The phosphoric acid solidifies less than 40ºC that makes startup very difficult. Therefore, it is unsuitable for use in cars.

1.5.5 Molten Carbonate Fuel Cell (MCFC)

A simple Molten Carbonate Fuel Cell (MCFC) is shown in figure 1.7. Large stationary power generators are added with MCFC nowadays. Their operation temperature is at 1112^0F (600^0C), so

they also generate steam that can generate more power. They have a lower operating temperature than the SOFC, which means they do not need expensive materials to design.

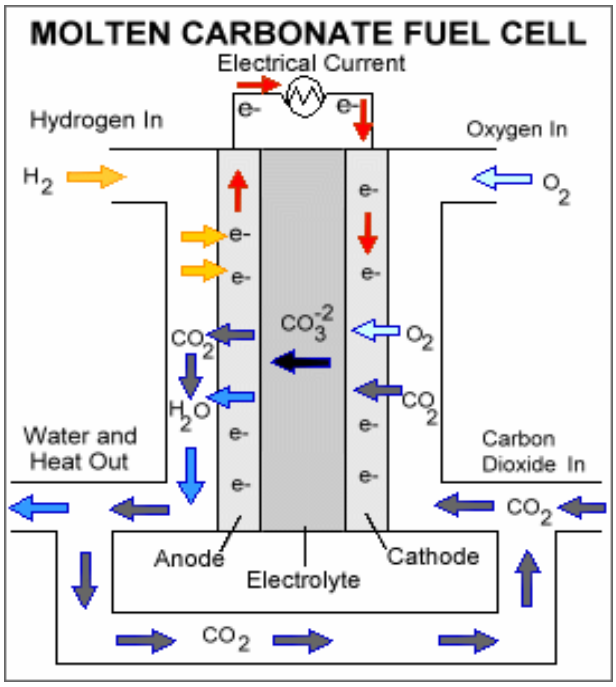

Figure 1.7: MCFC (Molten Carbonate Fuel Cell) [Catalyst and Surface Chemistry Lab, 2009]

1.5.6 Direct Methanol Fuel Cell (DMFC)

A different kind of PEMFC is the Direct Methanol Fuel Cell (DMFC). Here, the methanol is not reformed, but fed directly to the fuel cell. Therefore, does not need catalytic reforming, and the storage of methanol is much easier than that of hydrogen because it does not need to be done at high pressures. The energy density of methanol (the amount of hydrogen/volume) in orders of magnitude is greater than even highly compressed hydrogen. However, efficiency of MCFC is low, due to the high permeation of methanol through the membrane, and the dynamic behavior is sluggish. In addition, methanol is also extremely poisonous. Because of these strengths and problems, DMFCs produce limited power but can still store a lot of energy in a small space. This means they can produce a small amount of power over a long period of time, which makes them well suited to cell

phones and laptops but not in automotive companies.

1.5.7 Biological Fuel Cell

Bacteria reform glucose into hydrogen, or directly extract energy from glucose. This concept is used in operation of biological fuel cell. On the other hand, a microbial fuel cell exploits electrical currents generated by bacteria.

For this work, at first this study has been conducted on manufacturing of fuel cell different components. Application of Atmospheric Plasma Spray (APS) to SOFC manufacturing of different components of fuel cell is widely used by different researchers over the years. Bipolar plate or Gas Flow channel (GFC) are made of metallic or ceramic layer, Nickel- and steel-based alloys, doped lanthanum chromites, and cermet. Electrolyte is made of Yttria Stabilized Zirconia (YSZ) and gadolinium doped ceria (GDC). Due to its high thermal stability and purely oxide ionic conductivity, YSZ is the most commonly used electrolyte material for SOFCs. Anode is made of cermet (Ni mixed with the ceramic material). Cathode is made of lanthanum strontium manganite (LSM), LSM YSZ, and perovskite LSCF. There have been different techniques for SOFC electrolyte fabrications: spraying, extrusion, electrospinng, and tapecasting.

Due to convenient to manufacture fuel cell, APS is widely used by different researchers. Air Plasma Spray (APS) coating process, a form of thermal spray, uses ionized gas plasma to melt and propel the powdered coating material toward the substrate. This technique is used to manufacture solid alumina. However, knowledge that is gained from this process can be applied to the manufacturing of zirconia (ZrO_2) electrolyte membrane in SOFC.

Once assemble the whole fuel cell by different component parts, it is very important to keep adhesion between anode or cathode and electrolyte. Delamination and debonding between anode and cathode with electrolyte leads to low performance of fuel cell due to gas leak of reactant gases.

Different ways have been described by researchers for adhesion test. At present, adhesion tests to quantify mechanical failure are of two types: (1) Strength tests (2) Fracture tests. In addition to that, needle or wedge probe adhesion tests can also be used. Probe test is a quantitative tool for measuring adhesion. In this process, inclined needle-like conical tip probe is used to initiate debond. Interfacial fracture energy (G_i) (critical strain energy release rate) are used as quantitative measure of adhesion. Dow Chemical epoxy resin DER 331 with various levels of rubber concentration as an adhesive, and for aluminum, 6061-T6 alloy with different surface pretreatments as adherends [Chen, 1999] have been extensively used. Based on the literature review it is found that, very few works have been done providing complex information for adhesion at the interface of anode or cathode and electrolyte. It becomes clear that all the current literatures has lack completeness to address adhesion. To study the adhesion, this work has been started with the view to look at the phenomena of adhesion at the interface of anode or cathode and electrolyte.

Different parts of fuel cells have been developed over the span of years and details of that development have been discussed [Prater (1994)]. Single PEMFC only produces limited voltage and power. Therefore, lots of cells need to be connected together by arrangement of gas flow channels or bipolar plates in order to form a practical fuel cell stack. Bipolar plates work as the distribution of fuel and air uniformly over the entire active areas, the removal of heat from the stack, the conduction of current density from cell to cell, and the prevention of leakage. In general, a PEMFC involves complex species transport, chemical reactions, thermal and electrochemical processes. Concentration overpotential [Zhu and Kee (2003) and Fukunaga, Ihara, Sakaki, and Yamada (1996)] is led by transport resistances of the gaseous species in the gas flow channels and the porous electrodes. The concentration of fuel and oxidant in the local region is affected by the mixing of multiple gases in the gas flow channels, the mass transfer inside the porous anode or cathode, the reaction of fuel and

oxygen, and the transportation of fuel and electrochemical products, mainly water, near the triple-phase boundary. The consequence for this local concentration difference could limit the cell power density. The reactant gases have to be humidified to maintain high membrane water content along the channel. On the other hand, more water is generated at cathode side than anode due to the electrochemical reactions. However, when the pores of the porous cathode are filled with excess liquid water, the diffusion of reactant gas through the cathode becomes difficult and the liquid water may block the oxygen to contact with catalyst thus the PEMFC cannot work efficiently. For a PEMFC, a delicate balance between adequate humidification and flooding of water at the cathode has to be carefully controlled. Li and Chyu (2004) have shown the enhanced mass transfer in terms of different gas flow channel designs. Goodman, Trent, McNeil, Zee, Shimpalee, and Khan (2004), have designed various gas flow channels and tried to find out the best performance in terms of minimum flow rate, temperature distribution, heat flux distribution, output power and cooling in bipolar plate. Lim and Wang (2004) have used hydrophobic polymer content in the gas diffusion layer (GDL) to deal with water flooding and found an enhanced performance of cell. However, very less research works have been done systematically by others to demonstrate that how the gas flow channel configurations could affect the PEMFC performance. In this study, work has been conducted with the view that PEMFC gas flow channel design is a key factor for its normal operation. For a high performance PEMFC, choosing the best gas flow channel configuration is one of the possible ways to mitigate the water-flooding problem.

The ideal fuel for a PEMFC is pure hydrogen (H_2). Because of the difficulties inherent to storing hydrogen on board, there is an increasing interest in using hydrogen-rich gases produced by reforming methanol or even gasoline. Dry reformate is typically composed of hydrogen, carbon dioxide, a balance of nitrogen and up to 10,000 ppm carbon monoxide depending on the fuel

processing system as discussed by Inbody, Vanderborgh, Hedstrom, and Tafoye (1996), and Cheng, Chen, and Seaba(1999). If the hydrogen fuel is to be produced from a hydrocarbon-fuel reformer, the PEMFC may expose to transient pulses of high CO concentration (up to 10000 ppm).

It has been reported extensively that CO poisons the platinum or platinum alloy catalyst of PEMFC systems as discussed by Dhar, Christner, Kush, and Maru (1986), Bellows, Marucchi-Soos, and Buckley (1996), and Grgur, Markovic, and Ross (1999). In the poisoning process, carbon monoxide chemically adsorbs on to available Pt catalyst sites. Urian, Gulla, and Mukerjee (2003), have reported that the overpotential loss due to 10 ppm CO contamination at the current density of 0.5 A/cm^2 was close to 0.27V for platinum (Pt)/C catalyst. They have used a reformate composition: 45% H_2, 10 ppm CO, 15% CO_2, 1% CH_4 balanced with N_2.

To simulate a full fuel cell it cost time and limited by computational facility. Fuel cell simulation is dominated by serpentine or different designs of gas flow channels. However, the same mulitphysics involve in the whole cell can be transferred to single straight channel. Um and Wang, (2000), have presented a 3D single domain finite volume analysis of an interdigitated cathode flow field. A 3D numerical simulation of a 36 channel and $50cm^2$ PEMFC has been conducted by Wang, Wang, and Chen (2001). However, very few works have been done by researchers to simplify and transferring the concept of whole cell to single straight fuel cell channel.

Transient temperature rise on the catalyst layer can mitigate carbon monoxide poisoning. Operating PEMFCs at elevated temperatures (>100°C) reduces the effect of CO poisoning by Song, Fenton, Kunz, Bonville, and Williams (2005), and Song, Xu, Wei, Kunz, Bonville, and Fenton (2006). It has been reported that by increasing the PEMFC temperature to 110-120ºC, the CO tolerance improves to approximately 50 ppm at low anode catalyst loading (0.1-0.2 mg noble metal/cm^2). For a system operating at 140-160°C range, an increase of CO-tolerance level to 0.1- 0.5% is expected,

which could simplify the fuel reformer design. Dhar, Christner, and Kush (1987), have presented a detailed study on the CO adsorption during H_2 oxidation, to understand the polarization loss due to the poisoning by CO of a porous Pt anode under various conditions. Based on Dhar, Christner, and Kush (1987), a fuel cell could maintain the cell performance at 190°C when a 1000 ppm CO fuel is used. In contrast to this, at a cell temperature of 60°C, the cell is completely dead.

Thermal stress generates during Solid Oxide Fuel cell (SOFC) fabrication while using a precision bench-top High Temperature Vacuum Tube Furnace (model number GSL1600X, manufactured by MTI Corporation, USA). The furnace is widely used for processing materials (such as ceramics), developing new materials and sintering various types of material under vacuum or gaseous condition. Using a vacuum technique, Y123 metal films were obtained on CeO_2-buffered sapphire substrates by Yamaguchi., Sohma, Tsukada, Kondo, Kamiya, Mizuta, Kumagai, and Manabe (2006). The production of sodium carbonate via flash calcinations of Turkish trona ore in a drop tube furnace is described by Demirbas (2002). Analysis of HTVTF has been conducted by different researchers. To develop the method for analyzing transient characteristics of the combined radiative and conductive heat transfer in the industrial furnaces, heat transfer in vacuum furnaces is numerically analyzed by Mochida, Kudo, Mizutani, Hattori, Nakamura (1997). They developed a 3D computer program to solve radiative heat transfer within enclosure, which includes the transient conductive transfer of heat through the surrounding system of the insulation wall. Segall (2006) analyzes a post-mortem failure analysis of a silicon-carbide tube that failed after cyclic operation in a vacuum furnace. Very few works have been addressed to analyze fracture in HTVTF. In this work, study has been conducted to find exact location and causes of thermal stress during manufacturing of SOFC.

Fuel cell once starts operating or running, form liquid water due to electrochemical reaction

of hydrogen and oxygen. This water starts growing from unsaturated condition to saturated condition and then over saturated condition. Different parts of fuel cells which includes Membrane, Catalyst Layer, Gas Diffusion Layer and Gas flow channel are affected by this liquid saturation. In order to achieve better PEMFC performance, high membrane conductivity is one of the key parameters. The proton conductivity of Nafion^{TM} (Dupont) membrane, a most commonly used membrane, increases with the water content as discussed by Springer, Wilson, and Gottesfeld (1993). Although to effectively run the membrane saturation is needed, however too much water inside the fuel cell can damage performance of the fuel cell. Saturation of liquid that generates from the layer of catalyst layer eventually comes to gas flow channel. Water that generates at first without any shape from catalyst layer eventually can have shape of a droplet when comes from gas diffusion layer to gas flow channel. This process of droplet or bubble formation and breaking up of bubbles at the interface of GDL and Gas Flow channel is very important. Liquid droplet dispersion at the interface of GDL-GFC indicates possible saturation of that region. A transient isothermal simulation of a two dimensional PEMFC model using the finite volume method was developed by Um, Wang, and Chen (2000), while considering vapor form of water. The model did not consider saturation in the cell. The CFD simulation is compared to the experimental polarization curve of Ticianelli, Derouin, and Srinivasan (1988), without consideration of saturation. Very few works have been done by researchers to consider saturation for various dispersion of liquid water at the interface GDL-GFC. In this study, work has been conducted to find the scenarios of saturation inside GDL for different saturation values at the GDL-GFC interface. Also, droplet dispersion has been discussed.

1.6 Fuel Cell Numerical Analysis

Numerical analysis to find out performance of fuel cell, is one of the most challenging problems in fuel cell research. To simulate by using a software is a powerful way to understand the

fundamental physical and chemical processes of a fuel cell.

Numerical analysis of fuel cell involves three steps. For the first step, physical phenomena involved in fuel cell are analyzed. In the second step, a mathematical description of those phenomena is reflected in a set of equations that relate the significant variables. In final step, the system of equations is solved to predict the response of the system for a particular set of parameters, boundary and initial conditions.

There are lots of software programs are currently available in the market to numerically analyze fuel cells. Softwares that are available for fuel cells numerical analysis included COMSOL, FEMLAB User's guide (2005), Fluent, and Star-CD etc. These software packages solve the complicated 3-D partial differential equations by different techniques (finite element method, finite volume method etc.) that describe fuel cell phenomena. Current fuel cells literature [He, Yi and Nguyen (2000), Marr and Li (1999), Futerko and Hsing (2000), and Bernardi and Verbrugge (1991)] contains different ways of numerical analyses, with different focus and degrees of complexity. For this study, the performance of a PEMFC was simulated using a partial-differential equation solver, COMSOL. The analysis and date obtained from the simulation study using COMSOL will be beneficial for further and more complete analyses of the performance of fuel cells.

1.7 Research Objectives

In this study, experimental and numerical studies have been conducted for PEMFC and SOFC. The main objectives of the research presented here are to:

- Study physical phenomena (water generation, saturation, poisoning, and thermal stress) that govern the operation of a PEMFC and SOFC fuel cells.
- Conduct experimental studies and numerical simulations on PEMFC gas flow channel flows, operations, and thermal stresses in SOFCs.

- Study on application of APS (Air Plasma Spray) to SOFC manufacturing.
- Study on anode and cathode adhesion with electrolyte.

In addition to these works, detailed analyses have been conducted on:

- PEMFC poisoning and recovery
- PEMFC gas flow channel analysis
- Model pulse heating and transient temperature rise in fuel cell
- Modeling on thermal stress in SOFC fabrication.

1.8 Scope of the Dissertation

The first chapter of this work will provide a brief introduction to PEMFCs. The second chapter will focus on prior work related to application of APS to SOFC manufacturing, anode and cathode adhesion with electrolyte membrane, gas flow channel configurations, PEMFC poisoning and recovery, PEMFC single channel, transient temperature during pulse heating in Fuel Cell poisoning analysis, thermal stress in SOFC fabrication, and liquid droplet dispersion at the interface of GDL-GFC. Chapter 3 will present new experimental and operation methods for determining application of APS to SOFC manufacturing, anode and cathode adhesion with electrolyte membrane, gas flow channel configurations, and PEMFC poisoning and recovery, while Chapter 4 will present the numerical framework in which the characteristics are applied to describe PEMFC single channel, transient temperature during pulse heating in Fuel Cell poisoning analysis, thermal stress in SOFC fabrication, and liquid droplet dispersion at the interface of GDL-GFC. In these two chapters (the third and fourth), the results of the experiments are discussed, implemented in the analytical model, and used to make predictions which are then experimentally verified. Conclusions will be drawn from the experimental and numerical results and will be presented in the fifth chapter. Finally, the sixth chapter will provide recommendation for future work.

C H A P T E R - 2

LITERATURE SURVEY

Literature review has been conducted in the view of application of APS to SOFC, Anode and Cathode adhesion with electrolyte membrane, Gas Flow Channel configurations, Fuel cell poisoning and recovery, Single Channel analysis, and Thermal stress in SOFC fabrication. A variety of water transport models attempting to capture the effects of both liquid and vapor phase transport of water in proton exchange membrane fuel cells (PEMFCs) exist in the fuel cell literature. Many of these models include the entire structure of a single cell including the bipolar plates or the gas flow channels (GFCs), the gas diffusion layers (GDLs), the catalyst layers (CLs), and the polymer electrolyte membrane (PEM). However, simplified assumptions and inadequate material characterization generally limit the effectiveness of these models as engineering design tools. Some of the reviewed literature was aimed exclusively at the modeling of water in the GDL while much of it was aimed toward the modeling of the entire PEMFC. In addition, general approaches to modeling the transport processes in porous media are reviewed for their applicability to PEMFCs. Finally, some experimental techniques applied to fuel cells are reviewed. The following section will discuss literature review of operation and experimental analysis of fuel cell.

2.1 Fuel Cell Operation and Experimental Analysis

2.1.1 Application of APS to SOFC Manufacturing

Application of Atmoshperic Plasma Spray (APS) to SOFC manufacturing of different components of fuel cell is widely used by different researchers. Due to its high thermal stability and purely oxide ionic conductivity, YSZ is the most commonly used electrolyte material for SOFCs. Vaßen, Kaßner, Stuke, Hauler, Hathiramani, and Stöver (2008), have described APS technologies to produce coatings, which include NiO/YSZ for anodes, YSZ for electrolytes and different functional

coatings as Cr-evaporation layer on interconnects for solid oxide fuel cells (SOFCs). However, there is no information about the possibility of manufacturing YSZ from alumina using APS.

Benoveda, and Kesler (2009), have described APS that has been used to produce porous composite anodes based on $Ce_{0.8}Sm_{0.2}O_{1.9}$ (SDC) and Cu for use in solid oxide fuel cells (SOFCs). Fine CuO and SDC powders have been used to produce homogeneously mixed anode coatings with higher surface area microstructures.

White, Kesler, and Rose (2008), have described APS that has been used to produce porous composite cathodes containing $(La_{0.8}Sr_{0.2})_{0.98}MnO_3$ (LSM) and yttria-stabilized zirconia (YSZ) for use in SOFCs.

Rose, Kesler, Tang, and Burgess (2007), have described wet ceramic techniques such as tape casting or screen-printing. They investigates the use of spin coated sol gel derived YSZ precursor solutions to fill the pores present in APS YSZ layers, and to enhance the surface area for reaction at the electrolyte-cathode interface, without using the high-temperature firing steps for sintering.

Yang, Wen, Tu, Wang, and Yang, 2000, have described LaSrCrO powder that was used to make a 0.8, 0.2, 3 coating layer on the substrate of Cr plate by plasma flame spraying technique. LSC coated Cr could be used as the interconnector for SOFC.

Kang, Taylor, and Lee (2003), have described APS that was used for a mixture of La_3O_3, $SrCO_3$, and $MnCo_3$ to produce a porous cathode layer for potential application in planar SOFCs.

Waldbilling, and Kesler (2009), have described a method for manufacturing metal-supported SOFCs with APS in order to minimize contact resistance, and to allow the introduction of added porosity. Substrates with finer porosity resulted in lower kinetic losses in the fuel cell polarization. Kwon, Kumar, Park, and Lee, 2007, have described APS deposition for obtaining high power density from a SOFC. A conventional, micron-sized NiO, nickel-coated YSZ graphite

blend feedstock leads to a non-uniform layered coating microstructure.

Khor, Yu, Chan, and Chen (2003), have described numerous inter-granular defects in yttria stabilized zirconia (YSZ) electrolyte while SOFC manufacturing by APS. These defects will lead less gas tight and consequently, the energy efficiency of the cell is severely curtailed.

Benyoucef, Klein, Coddet, Benyouce (2008), have described alternative (Ni, Cu, Co)–YSZ and Cu-Co-YSZ anode cermets materials that are coated by APS. The spray parameters which include carrying gas flow rate, spraying distance, argon flow rate and hydrogen flow rate were investigated.

Kim, Kwon, Kumar, Xiong, and Lee (2008), have described preparation and characterization of porous anode layers with uniform phase distribution for SOFC application. The Ni/8YSZ cermet coatings were fabricated by APS process using oxidized nickel coated graphite (Ni-graphite) and 8 mol% yittria-stabilized zirconia (8YSZ) blend as feedstock.

Caron, Bianchi, and Me´thout have discussed efficient air tightness between two SOFC cells. In their study, a solid seal composed of a ceramic matrix charged with glass particles has been developed by APS.

Schiller, Henne, Lang, Ruckdaschel, and Schaper (2000) have described the reduction of the operating temperature of planar SOFCs to an intermediate temperature regime of 650-800^{0}C by APS, when deposition of the entire MEA is done onto a porous metallic substrate within a very short process time.

Zhang, Li, Liao, Planche, Li, and Coddet (2008), have described the effect of particle velocity on the characteristics of APS made YSZ that was investigated through adjusting auxiliary helium flow rate.

Ning, Li, Li, and Yang (2006), have described electrolyte coatings by APS that were

prepared by 4.5 mol% YSZ powders.

Li, Li, and Wang (2005), have described lanthanum strontium manganate (LSM) perovskite oxide that has been widely employed as cathode materials for SOFCs at different plasma powers and spray distances. The annealing treatment at a high temperature led to the elimination of the metastable phase and improved the electrical conductivity.

Changjing, Kening, Derui (2006) have described SUS430 that can be used as interconnects for SOFCs that operate at lower temperatures by APS.

Fu, Sun, Chen, Zhang, and Zhou (2008), have described a protective nickel layer that was prepared on the SUS430 alloy substrate by APS. The current collector between the interconnect and the anode was optimized during manufacturing process in this paper.

Brandner, Bram, Froitzheim, Buckremer, and Stöver (2008), have described metal-supported SOFCs that are considered to have a high potential for use in mobile applications. In sintering experiments at 1100°C for 3 hours in argon atmosphere $Ce_{0.8}Gd_{0.2}O_2$ and CeO_2 displayed promising results by completely avoiding any interdiffusion.

Lang, Franco, Schiller, and Wagner (2002), have focused on the electrochemical characterization, such as current–voltage measurements and long-term operation of completely APS SOFC assemblies for a planar metallic substrate-supported thin film concept.

Fu, Sun, Zhang, Chen, and Zhou (2008), have described an $La_{0.8}Sr_{0.2}FeO_{3-\delta}$ (LSF20) protective layer that has been prepared on SUS430 alloy substrate using the APS combined with nitrate solution impregnation and its effectiveness was evaluated.

Kim, Songa, Songa, Hyunb, Shin, and Yokokawa (2003), have described an anode-supported flat-tube SOFC that is developed to increase the cell power density and thermal stability by combining tubular and planar cell structures. An electrolyte of YSZ and a multi-layered cathode

of a $(La_{0.85}Sr_{0.15})_{0.9}MnO_3$ (LSM)/YSZ composite, LSM, and $La_{0.6}Sr_{0.4}Co_{0.2}Fe_{0.8}O_3$ (LSCF) are coated on the anode tube by slurry dip coating.

Nguyen, Honda, Kato, Iimura, Kato, Negishi, Nozzki, Shiono, Kobayashi, Hosoda, Cai, and Dokiyab (2004), have described an anode-supported tubular SOFC with a thin electrolyte film for reduced temperature operation. Better performances of the anode-supported tubular SOFCs has been achieved by their work for further optimizations for the zirconia/ceria interface, control of both porosity and thickness of the anode substrate, as well as improvement of the $(La_{0.6}Sr_{0.4})$ CoO_3 cathode.

Yang, Zhang, Wang, and Xia (2007) have described APS that was used to prepare the planar positive/electrolyte/negative (PEN) and mono-block layer built (MOLB) type PEN SOFCs. Their results show that graded layers formed between the electrodes and electrolyte.

Hwang, and Yu (2007), have described YSZ/Ni for making the anode of a SOFC. Agglomerated nanostructured YSZ/NiO powders and APS are applied to produce nanostructured YSZ/NiO coatings on porous support substrates. Their work also claimed that this new YSZ/Ni anode provides larger triple phase boundaries for hydrogen oxidation reactions.

Xia, Zhang, Wang. and Yang (2009), have described thermal spray that was applied by gradually changing the compositions of powders. To improve the electrochemical performance and mismatch between different layers both the graded anode layer containing NiO/YSZ and YSZ and the cathode graded layer containing LSCF and YSZ were plasma sprayed by fifteen (15) sublayers.

Te´ne`ze, Caron, and Alexandre (2008) have described SOFCs plasma spraying processes that allow to elaborate coatings with singular microstructures while depending strongly on the initial material and plasma operating conditions.

Huia, Berghausb, Petit, Qua, Yicka, Legouxb, and Moreaub (2009), have described metal-

supported SOFCs that consist of porous NiO–SDC as anode, thin SDC as electrolyte, and SSCo as cathode on porous stainless steel substrate. The anode and electrolyte layers were consecutively deposited as discussed by their work, onto porous metal substrate by thermal spray, using standard industrial thermal spray equipment, operated in an open-air atmosphere.

White and Kesler (2008) have described electronic short circuiting of the electrolyte in a SOFC arising from flaws in the APS fabrication process that has been found to have a significant effect on the perceived performance of the electrodes. Their study lead to the presence of a short circuit that has been found to lead to the underestimation of the electrode polarization resistance (R_p) and hence an overestimation of electrode performance.

Gitzhofer and Jia (2008) have described APS that has been successfully applied to the synthesis of nanomaterials, and the sintering of electrolytes. According to their study, this APS can also be directly used to synthesize anodes, electrolytes, and cathodes which was established on reformer-supported SOFC, in addition to the synthesis of the reformer component or structure.

To´tha, Fqlea, Veresa, Selmanb, Arconc, Po´csika, and Koo´sa (2005), have described electric double layer supercapacitor electrodes that were prepared from a mixture of carbon black, amorphous carbon nano-particles and binder to obtain higher capacitance. According to their study, the active material was laid on it by APS.

Lim, Lim, Oh, and Lyo (2005), have described temperature range of 600–700°C that allows the use of cheaper and more conductive metallic interconnect materials instead of ceramics. In this study, an LSM ($La_{0.8}Sr_{0.2}MnO_3$) coating was deposited by APS. Uniform and dense coatings of LSM were deposited on stainless steel by plasma spraying by this study.

Xing, Li, Li, and Yang (2008), have described the development of a cost-effective fabrication method for stabilized zirconia electrolyte for the most advanced tubular SOFC. Continuous growth

of columnar grains across splat–splat interfaces has been achieved through control of the substrate surface temperature, which affects spreading of molten droplets and lead to improved bonding between lamellae have been studied.

Li, Li, Xing, Gao, and Yang (2006), have described novel Ni–Al_2O_3 cermet-supported tubular SOFC cell that was fabricated by thermal spraying and act as support tube and anode current collector. In their study, Y_2O_3-stabilized ZrO_2 (YSZ) electrolyte was deposited by APS. Their study found that the reduction of YSZ thickness from 100 μm to 40 μm led to the increase of the maximum output power density from 0.47 W/cm^2 to 0.76 W/cm^2 at 1000°C.

Nie, Huang, Wen, Tu, and Zhan (2002), have described porous LSM cathodes that can be successfully prepared by APS. Their study indicated the cathode layer improvement in conductivities as well as cathodic overpotential performance after heat treatment in air at 1000^0C.

Zhang, Li, Liao, Li, Li, and Coddet (2007) have described the YSZ/LSM composite coating that was deposited by APS using the mechanical blending LSM and YSZ with ratios of 50:50, 40:60, and 20:80 wt.%. The anisotropy of the electrical conductivity is found to the phases of different properties in the composite coating and the APS coating structure characteristics. The results also showed that the electrical conduction of the composite was strongly influenced by the YSZ content.

Ning, Li, Li, and Yang (2006), have described 4.5 mol% YSZ coating that was deposited by APS as an electrolyte for SOFCs applications. Their study found that the nanocontacts between lamellae resulted in high contact resistance and limit improvement of electrical conductivity of the coating after densification.

Wantanabe, Yamashita, Chen, Yamanka, Kotobuki, Suzuki, and Uchida (2007), have described nickel nanoparticulate catalysts supported on hollow Al_2O_3 ball that have been prepared by spraying a mixed solution of nickel and aluminum nitrates in APS. Their study showed that the

catalyst possessed superior performances for the reaction in the activity and the resistance to coke deposition even under a low H_2O/CH_4 molar ratio condition.

Wang and Coyle (2007) have described the solution precursor plasma spray process, in which a solution precursor of the desired resultant material is fed into a plasma jet by atomizing gas or high pressure. In their study, the processing parameters investigated include: hydrogen flow rate, current, solute flow rate, solution concentration, distance between nozzle and gun, and stand off distance.

Fox and Clyne (2004) have described the specific permeability of oxygen (O_2) in plasma sprayed zirconia with some dependence on microstructure, and hence on spraying conditions. According to their study, permeability rises with increasing temperature and differences of a factor of approximately four (4) were observed between room temperature and 600^0C.

Fauchais, Salas, Rat, Coudert, Caron, and Te´ne`ze (2008) have described plasma spraying in order to achieve finely or nano-structured coatings. Their study describes the different plasma torches that are used, the way liquid jet is injected, and the different measurements techniques.

Li, Li, Long, Xing, and Yang (2008), have described Ni–Al_2O_3 cermet supported tubular SOFC that was fabricated by thermal spraying. In their study, the test cell was assembled employing scandia stabilized zirconia (ScSZ) and YSZ deposits as the electrolyte. Their study also indicates that the design and preparation of effective electrode in the SOFC assembly using thin electrolyte are more important to improve cell performance.

Li, Li, and Ning (2004), have described YSZ that was deposited by plasma spraying to develop a cost-effective processing method for the fabrication of electrolyte layer in SOFCs. A densification process to plasma-sprayed YSZ coating was conducted by their study with the aim of achieving a dense coating of necessary gas-tightness and an improved ionic conductivity.

Gao, Liao, and Coddet (2008), have described the apatite-type lanthanum silicate films that

were successfully synthesized by modified APS using lanthanum oxide and silicon oxide mixed powders and precalcined hypereutectic powders, respectively, as starting feedstock materials. A detail describing the evolution of microstructure has been discussed by this study.

Hwang, Tsai, Lo, and Sun (2008), have described SOFCs supported by a porous Ni-substrate and based on Sr and Mg doped lanthanum gallate (LSGM) electrolyte, lanthanum strontium cobalt ferrite (LSCF) cathode and nanostructured yttria stabilized zirconia–nickel (YSZ/Ni) cermet anode fabricated successfully by APS. According to their study, the cathode keeps right phase structure and porous network microstructure for conducting electrons and negative oxygen ions.

Huang, Berghuas, Yang, Yick, Wang, Wang, and Hui (2008), have described polarization characteristics of metal-supported SOFCs, fabricated by APS. According to their study, results from experiments and simulation indicate that fabrication processes and operation temperatures play an important role in the electrochemical mechanism for linear polarization characteristics of metal-supported SOFCs.

Badillo, Ageorges, Chartier, Coudert, and Fauchais (2006), have described perovskite type doped $LaMnO_3$ as cathode material for the SOFC. Their study discussed that, the process conditions, including plasma-forming gases, mass flow rates, and current intensity and the powder characteristics including particle size and, percentage of MnO_2 doping were found strongly influence on perovskite coating composition.

Nie, Wen, and Tu (2003), have described plasma spraying and subsequent heat/reduction treatment $(La_{0.8}Sr_{0.2})_{0.9}MnO_3$ and Ni protection coatings for Cr-based interconnect. Their study show that $(La_{0.8}Sr_{0.2})_{0.9}MnO_3$ and Ni coatings adhered well to the interconnect and were effective in protecting the interconnect from oxidation and corrosion.

Fehringer, Janes, Wildersohn, and Clasen (2004), have described the synthesis, preparation

and examination of the cathode lanthan–strontium–manganite (ULSM) as bulk material, the BCN electrolyte and the cermet anode (BCN/Ni) as coating. On the surface of ULSM the BCN electrolyte was prepared by APS as shown in their study.

Wang and Coyle (2008) have described conventional plasma spray of SOFC components which are the large NiO and YSZ particles used, that reduce the density of three-phase sites for electrode reaction. Their study indicated that the deposits were composed of tower-like, irregularly shaped agglomerates and smooth surface deposits. The sizes of the agglomerates increase with the decrease of the plasma-torch power and most are not completely molten during the impact as shown by their study.

Larringz and Norby (2000), have described degradation of the interface between Plansee Ducrolloy alloy (Cr-5 wt % Fe-1 wt %Y_2O_3) (PD) and $(La_{0.85}Sr_{0.15})_{0.91}MnO_3$ (LSM) ceramic. Their study shown that coatings forming $MnCr_2O_4$ spinel and using $La_{0.8}Sr_{0.2}CoO_3$ as a contacting layer showed a low estimated degradation of 0.04-0.06 V cm^2 after 10,000 h.

Fauchais, Salas, Delbos, Rat, Coudert and Chartier (2007), have described APS that allows achieving finely structured coatings. Their study showed that, it requires a dense stabilized zirconia electrolyte with two porous electrodes: cathode made of perovskite prone to decomposing upon spraying and anode made of two materials (nickel and zirconia) with very different melting points.

Nishida, Kakinuma, Nishino, Kamino, Yamashita, Watanabe, and Uchida (2009), have described APS at SOFC anode applications, nanometer-sized nickel catalysts supported on hollow spherical particles of samaria-doped ceria (Ni/SDC) by spraying a mixed solution of nickel, samarium, and cerium nitrates into an APS.

Waldbillig and Kesler (2009), have described APS that uses small (=2 μm) particles to fabricate coatings with fine microstructures and controlled porosity and without the need for post-

deposition heat treatments. Their study indicated that, in order to be able to manufacture layers with microstructures, the properties of the feedstock suspension must be optimized to enhance particle dispersion and improve feedability.

2.1.2 Anode and Cathode Adhesion with Electrolyte Membrane

The effect of thermal cycling on a state of stress in polymeric materials bonded to stiff elastic substrates was investigated by Humfeld (1997). All coupled, numerical techniques were used to acquire approximate solutions due to complexity of developing a closed-form solution for a system with time, temperature, material properties, and boundary conditions. According to this study, tensile and peel stresses develop over a long period of time as a result of viscoelastic response to thermal stresses induced in polymeric layer. In addition, applied strain energy release rate at crack tip of layered specimens has shown similar increase. This study of numerical work indicate that, the residual stresses in an elastic-viscoelastic bimaterial system incrementally shift over time when subjected to thermal cycling. This study also showed that the rate of change of stress state is dependent upon the thermal cycling profile and adhesive's thermo-mechanical response. This study also indicate that incrementing tensile residual stresses induced in an adhesive bond subjected by thermal cycling may lead to damage and debonding which reduce durability.

A simple and cost-effective finite element model (FEM) has been used to analyze adhesive bonds in actual structures by Andruet (1998). Stress and durability analyses of crack patch geometries are possible applications of this finite element model. In this study, special 2/3D adhesive elements have been developed for stress and displacement analyses in adhesively bonded joints. Both 2- and 3-D elements are used in this study to model the whole adhesive system: adherends and adhesive layer. In 2-D elements, adherends are represented by Bernoulli beam elements with axial deformation and adhesive layer by plane stress or plane strain elements. The nodes of plane stress-strain elements that

lie in adherend-adhesive interface are rigidly linked with nodes of beam elements. 3-D elements consist of shell elements that represent adherends and solid brick elements to model adhesive. This technique results in smaller models with faster convergence than ordinary finite element models. According to their study, the resulting mesh can represent arbitrary geometries of adhesive layer and include cracks. Since large displacements are often observed in adhesively bonded joints, geometric nonlinearity is modeled. 2- and 3-D stress analyses of single lap joints are presented by this study. Stress analysis of a crack patch geometry is presented. Numerical simulation of debonding of patch is also included in this study.

Using Dow Chemical epoxy resin DER 331 with various levels of rubber concentration as an adhesive, and aluminum 6061-T6 alloy with different surface pretreatments as adherends by Chen (1999). Both symmetric and asymmetric double cantilever beam (DCB) specimens are prepared and tested under mixed mode fracture conditions in this study. Post-failure analyses conducted on failure surfaces indicate that failure tends to be more interfacial as the mode-II component in fracture increases, whereas, more advanced surface preparation techniques can prevent failure at interface. Through mechanically stretching DCB specimens uniaxially stretched until adherends are plastically deformed, various levels of T-stress are achieved in the specimens by this study. Test results of specimens with various T-stresses demonstrate that directional stability of cracks in adhesive bonds depends on T-stress level. This study also indicated that cracks tend to be directionally stable when T-stress is compressive whereas directionally unstable when T-stress is tensile. However, direction of crack propagation is mostly stabilized when more than 3% mode-II fracture component is present in loading regardless of T-stress levels in the specimens. In this study, since fracture sequences in adhesive bonds are closely related to energy balance in the system, an energy balance model is developed to predict directional stability of cracks and results are consistent with experimental

observations. Using finite element method (FEM), T-stress has shown to be closely related to specimen geometry, indicating a specimen geometry dependence of directional stability of cracks. This prediction by this study is verified through testing DCB specimens with various adherend and adhesives thicknesses. By testing the specimens under both quasi-static and low-speed impact conditions, and using a high-speed camera to monitor fracture sequence, this study indicated the influences of debond rate on the locus of failure and the directional stability of cracks are investigated. Post-failure analyses suggest that failure tends to be more interfacial when debond rate is low and tends to be more cohesive when debond rate is high. However, this study found that, rate dependence of locus of failure is greatly reduced when more advanced surface preparation techniques are used in preparing the specimens. The post-failure analyses also reveal that cracks tend to be more directionally unstable as the debond rate increases. According to their study, employing interface mechanics and extending criteria for direction of crack propagation to adhesively bonded joints, crack trajectories for directionally unstable cracks are predicted and results are consistent with overall features of crack paths observed experimentally.

Based on the literature review it is found that, very few works have been done providing information for adhesion at the interface of thin metal and substrate. Although some papers and works have important information but it becomes clear that all these lack completeness. Research has been conducted with the view to look at the complex phenomena of adhesion at the interface of thin film and substrate.

2.1.3 Gas Flow Channel Configurations

The major functions of a PEMFC gas flow channel includes distribution of fuel and oxidant uniformly over the entire MEA (Membrane Electrode Assembly) active areas, removal of heat from the cell, conduction of current from cell to cell and prevention of gas leakage. Typically, the function

of a PEMFC involves complex species transport, chemical reactions, thermal and electrochemical processes. The Transport resistances of gaseous species in the gas flow channels and the porous electrodes, studied by Zhu and Kee (2003), also by Fukunga, Ihara, Sakai, and Yamada (1996), lead to the so-called concentration overpotential. The local concentration of fuel cell and oxidant is affected by the mixture of multiple gases in the gas flow channels. It is well known that, the mass transfer processes could limit the cell power density. For a high performance PEMFC, choosing the best gas flow channel configuration is one of the possible ways to mitigate the water-flooding problem. Weng, Su, Hsu, and Lee (2006), as well as Su, Weng, Hsu, and Chen (2006), made prototypes of fuel cell and tried to observe the water flooding phenomena. However, their study did not properly address water generation in the original fuel cell because a prototype cell will show different behavior than an original or actual cell. Moreover, this study did not deal with straight and interdigitated flow channels. Li and Chu (2004), have shown the enhanced mass transfer in terms of different gas flow channel designs without market available designs. Thus, manufacturing these designs will lead to a problem. Yoon, Lee, Park, Yang, and Kim (2004), have investigated effects of widths of rib and channel of a flow field plate on the performance of a PEMFC in an effort to optimize the dimensions of rib and channel using four different kinds of plates. This work did not deal with market-available and other flow channel designs. Zee, Shimpalee, and Khan (2004), have designed various gas flow channels and tried to determine the best performance in terms of minimum flow rate, temperature distribution, heat flux distribution, output power and cooling. However, issues concerning thermal and fluid flow in PEMFCs were not studied.

In research literature, very little work has been done to demonstrate systematically, how gas flow channel configurations could affect the PEMFC performance. Therefore, experimental studies of the effect of gas flow channel design on the performance of PEMFC are still lacking in the

literature. In this study, the influence of gas flow channel design on the performance of PEMFC was studied experimentally. The objective of this study is to find the best performance of a cell using a combination of three basic gas flow channel designs: straight, serpentine and interdigitated. Performance is analyzed in terms of percentage of water in the gas flow channel, the flooding pattern of water, the fuel utilization rate, the different reacting gas flow rates, and the cell voltage versus current density curve.

Transport resistances of gaseous species in the gas flow channels and the porous electrodes lead to the so-called concentration overpotential [Zhu and Kee (2003), Fukunaga, Ihara, Sakaki, and Yamada (1996)]. The local concentration of fuel and oxidant is affected by mixing of multiple gases in the gas flow channels. It is well known that the mass transfer processes could limit the cell power density. For a high performance PEMFC, choosing the best gas flow channel configuration is one of the possible ways to mitigate the water-flooding problem. Li and Chyu (2004), showed the enhanced mass transfer in terms of different gas flow channel designs. Zee, Shimpalee, and Khan have designed various gas flow channels and tried to determine the best performance in terms of minimum flow rate, temperature distribution, heat flux distribution, output power and cooling in those gas flow channels. Lim and Wang (2004) have used hydrophobic polymer content in the gas diffusion layer (GDL) to deal with water flooding problem and found an enhanced performance of the cell. Although Zhang F.Y., Yang X.G. and Wang (2006), and Lu and Wang (2004), worked on DMFC but their works can be implemented in PEMFC area and had some information. Weng, Su, Hsu, Lee (2006), and Su, Weng, Hsu, Chen (2006), have made prototype of fuel cell and tried to observe the water flooding phenomena. However, their study does not properly address water generation inside cell. Very few works have been done systematically by researchers to demonstrate that how the gas flow channel configurations could affect the PEMFC performance.

2.1.4 PEMFC Poisoning and Recovery

There exist three methods to mitigate the CO poisoning: (i) the use of a platinum alloy catalyst, (ii) higher cell operating temperature, and (iii) introduction of oxygen (O_2) into the fuel stream. Pt/Ru (Ruthenium) alloy has been found to improve the CO tolerant level [Gasteiger, Markovic, and Ross (1995), and Bellows, Marucchi-Soos, and Reynolds (1998)]. At a temperature between 70 to 85°C, the Pt/Ru (1:1 atomic ratio) alloy catalyst may tolerate CO concentrations up to 100 ppm. Another way to increase the CO tolerance is to inject oxygen into the fuel stream [Schmidt, Oetjen, and Divisek (1997)]. However, this would inevitably reduce the fuel utilization rate. The injection of oxygen or air into the fuel stream at high CO concentration may not reduce the poisoning effect over long run. Figure 2.1 from Lee, Zee, and Murthy (2003), demonstrated the air bleeding could significantly reduce the CO poisoning rate. However, over the transition process, the cell is still poisoned. The following section will discuss literature review of numerical analysis of fuel cell.

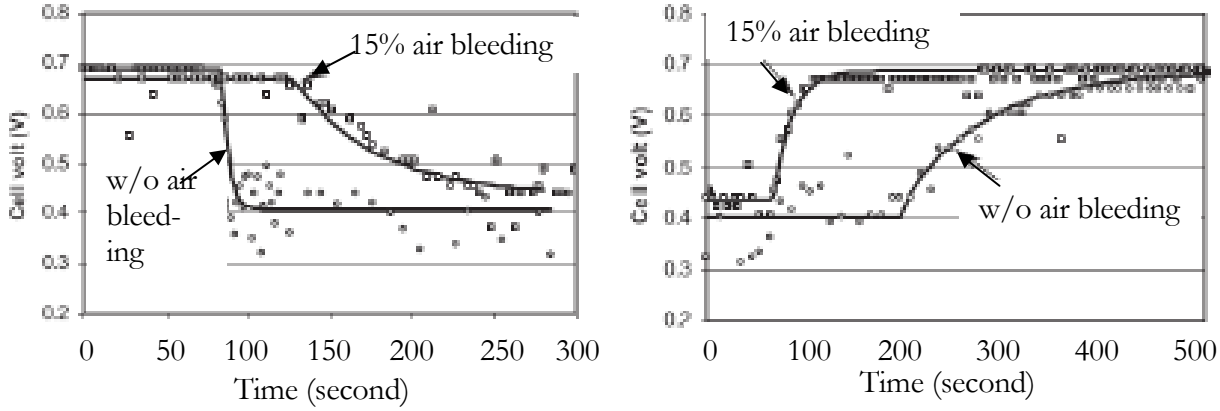

Figure 2.1: Air bleeding effect on PEMFC CO poisoning (left) & recovery (right) process [Lee, Zee, and Murthy, 2003], 3000 ppm CO at a 61.8 μmol dose

2.2 Numerical Analysis

2.2.1 Single Channel Analysis

It is well known that at high current density the losses are dominated by the limitation of

transport of fuel or oxidant to the reaction sites, the so-called concentration or mass transport over-potential. Mass transport in the porous electrodes depends on the structure of the porous electrodes, such as the porosity, tortuosity and mean pore size. Wasak, Guo, and Turan (2005), and Suwanwarangkul, Croiset, Fowler, Douglas, Entchev, and Douglas (2003), conducted comparative studies using the Fick's law and the Dusty Gas Model for a Solid Oxide Fuel Cell. They found that the current density, the reactant concentration and the pore size were the three key parameters for choosing a proper porous media simulation model. The Dusty Gas Model works better for the H_2–H_2O and CO–CO_2 systems, especially under high operating current densities, low reactant concentrations and small pore sizes. A transient isothermal simulation of a two dimensional PEMFC model using the finite volume method was developed by Um, Wang and Chen (2000), and compared to the experimental polarization curve of Ticianelli, Derouin, and Srinivasan (1988). Comparison is made between humidified H_2 and humidified H_2 diluted by N_2. Guo, and Hasan (2009), have conducted transient temperature distribution in membrane and catalyst layer using heating pulse. Um, and Wang, 2000, present a 3D single domain finite volume analysis of an interdigitated cathode flow field. A 3D numerical simulation of a 36 channel 50cm^2 PEMFC has been conducted by Wang, Wang, and Chen (2001). Ju, Meng, and Wang (2005), present a non-isothermal, 3-D model of a PEMFC and the effect of heat produced in different regions of the cell. Kulikovsky (2003) has showed various conservation equations for MEA. There is no information about gas and liquid transport considering all the parts in a cell. Hsing and Futerko (2000), present a finite element analysis of 2D water transport in the PEMFC without external humidification of gases (i.e. water is present only due to electrochemical reaction on cathode side). The catalyst layer is treated as an interface between the gas diffusion layer and membrane, which in some sense is not accurate as the catalyst layer will have a thickness. 3-D numerical simulation using commercial computational fluid

dynamics software has been conducted by Lee and Chu (2006) to locate the gas-liquid interface for PEMFC for various relative humidity in the cathode gas diffusion layer and gas flow channel. Hasan and Guo (2005) and Hasan (2005) have optimized different configurations of gas flow channel to mitigate water flooding after electrochemical reaction. Coppo (2005) has used mathematical equation for water droplet inside gas flow channel in relation with surface tension and drag force when it will be moved inside the channel by air flow.

2.2.2 Transient Temperature during Pulse Heating in Fuel Cell Poisoning Analysis

Operating PEMFCs at elevated temperatures (>100°C) reduces the effect of CO poisoning [Song, Fenton, Kunz, Bonville, and Williams (2005), and Song, Xu, Wei, Kunz, Bonville, and Fenton (2006)]. It has been reported that by increasing the PEMFC temperature to 110-120ºC, the CO tolerance improves to approximately 50 ppm at low anode catalyst loading (0.1-0.2 mg noble

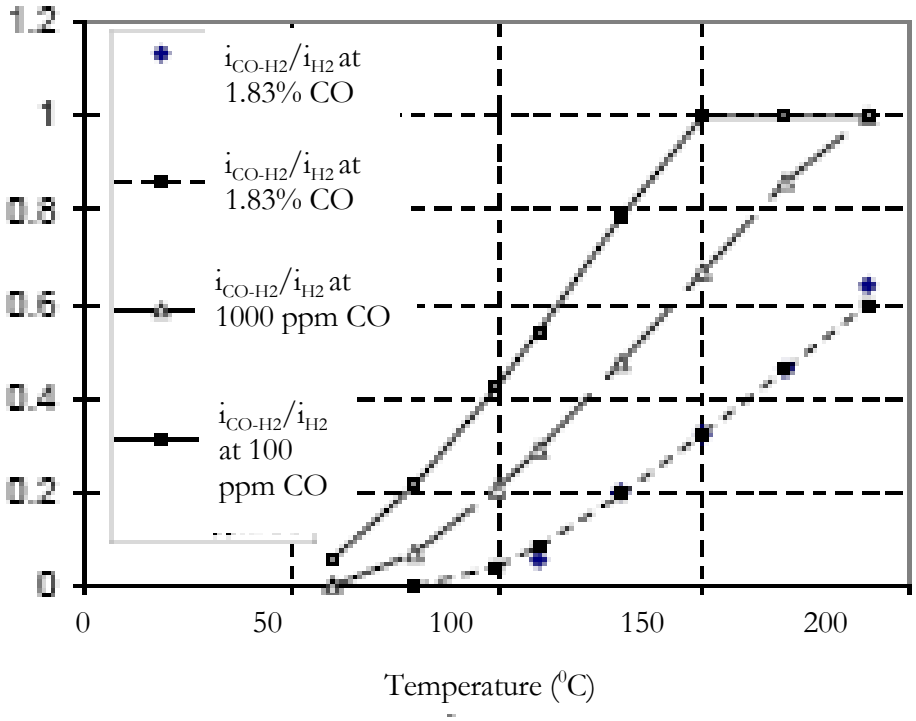

Figure 2.2: Normalized PEMFC (i_{CO-H2}/i_{H2}) performance at different temperatures, based on Dhar, Christner, and Kush, 1987

metal/cm^2). For a system operating at 140-160°C range, an increase of CO-tolerance level to 0.1-

0.5% is expected, which could simplify the fuel reformer design. Dhar, Christner, and Kush (1987), presented a detailed study on the CO adsorption during H_2 oxidation to understand the polarization loss due to the poisoning by CO of a porous Pt anode under various conditions. Based on [Dhar, Christner, and Kush (1987)] figure 2.2 shows that a fuel cell could maintain the cell performance at 190°C when a 1000 ppm CO fuel is used. In contrast, at a cell temperature of 60°C, the cell is completely dead. Although high temperature membranes theoretically may have many advantages, the physical properties of the current high temperature membranes cannot match the advanced commercially available membranes, whose operating temperature is usually less than 80ºC.

2.2.3 Thermal Stress in SOFC Fabrication

A precision bench-top High Temperature Vacuum Tube Furnace (model number GSL1600X, manufactured by MTI Corporation, USA) is a furnace using $MoSi_2$ as heating element and the vacuum tube can be heated up to 1600ºC (1872ºK, 2912ºF). The furnace is widely used for processing materials (such as ceramics), developing new materials and sintering various types of material under vacuum or gaseous condition. Using a vacuum technique Y123 metal films were obtained on CeO_2-buffered sapphire substrates by Yamaguchi, Sohma, Tsukada, Kondo, Kamiya, Mizuta, Kumagai, and Manabe (2006). The production of sodium carbonate via flash calcinations of Turkish trona ore in a drop tube furnace is described by Demirbas (2002). Method has been developed by Zhang, Wang, Wang, Chen, and Feng (1995), for the determination of antimony, arsenic, bismuth, selenium, tellurium and tin under subatmospheric pressure in an electrically heated quartz tube furnace. Several biomaterials have been pyrolyzed by DeLuca and Voorhees (1993), who used a resistively heated tube furnace. The paper by Strumpf, Stillwagon, Kotchick, and Coombs, (1988), summarizes the use of ceramic heat pipe recuperators for high-temperature heat recovery from industrial furnaces. Materials surface cleaning using a furnace for determinations of gases in

metals is described in detail by Lounama, Aass, Kühne, and Persson (1963). The metallurgical processing of zircaloy for reactor fuel pin cladding (each consisting of an array of tubes) in a high-vacuum furnace is described by Pissanetzky (1980).

Analysis of HTVTF has been conducted by different researchers. To develop the method for analyzing transient characteristics of the combined radiative and conductive heat transfer in the industrial furnaces, heat transfer in vacuum furnaces is numerically analyzed by Mochida, Kudo, Mizutani, Hattori, and Nakamura (1997). Their study developed a 3D computer program to solve radiative heat transfer within enclosure which includes the transient conductive transfer of heat through the surrounding system of the insulation wall. A post-mortem failure analysis of a silicon-carbide tube that failed after cyclic operation in a vacuum furnace is analyzed by Segall (2006). Results of the fractographic analysis and service history indicated - thermomechanically induced severe defects on the internal (heated) surface. A high vacuum cylindrical furnace having the load of cylindrical tubes and supported by a carriage is described by Pissanetzky, Cingolani, Volpi, and Almagro (1981). Their results allow designing a high vacuum industrial furnace and optimization of its loads. A mathematical model was presented by Pissanetzky (1980), and work is shown for the numerical simulation of heat transfer by radiation and conduction, however important phenomena involving natural convection have been neglected.

2.2.4 Liquid Droplet Dispersion at the Interface of GDL-GFC

Liquid droplet dispersion at the interface of GDL-GFC indicates possible saturation of that region. Um, Wang and Chen (2000), have developed a transient isothermal two-dimensional PEMFC model using the FVM (finite volume method) which considers seven regions that include GFC, GDL, and CL for both anode and cathode sides and a membrane. Transient response is considered for current density and velocity profiles and gas concentrations in anode and cathode flow channels.

Reformate gas as well as N_2 is considered on the anode side. Comparison is made between humidified H_2 and humidified H_2 diluted by N_2. The Butler-Volmer equation is simplified while using in this work. N_2 as well as reformat gas are considered in anode side where H_2 dilution by N_2 is considered in this work. Transient response of current density is shown. Their work have shown that H_2 dilution effects on lower cell performance. The author mostly deals with H_2 dilution effects, however liquid water effect at the interface of GDL-GFC is neglected.

Coppo, 2005, has used mathematical equation for water droplet inside gas flow channel in relation with surface tension and drag force when it will be moved inside the channel by air flow. Detailed equations involved in fuel cell were discussed in this works. Due to lack of experimental facility data was not able to take, although experimental rig was made to take experimental data and to visualize two-phase water droplet generation and blow out by air flow in gas flow channel with optical techniques. The work depicts saturation trends in cathode side catalyst layer, gas diffusion layer, gas flow channel from left to right. In higher voltage, which is related to lower current, will produce low water after electrochemical reaction so saturation is lower. In the same way, lower voltage that is related to higher current will produce higher water so, the saturation is higher. Also from this work, gas channel-GDL interface saturation values can be found. In the high current case 9% of the catalyst pores are filled with water. On the other hand, 2.5% of the catalyst pores are filled when the cell current is low. The increase of saturation value in the interface between GDL-GFC was found as saturation was corrected in the channel to yield the true liquid to gas volumetric ratio.

Um and Wang (2000), presented a three-dimensional single domain FV (finite volume) analysis of an interdigitated cathode flow field. From the study, in the model seven-regions or domains are considered. The data obtained from this work indicate that forced convection in the interdigitated flow field enhances mass transport of oxygen and water removal from the reaction

zone. Numerical simulation results explained the flow of gases, oxygen and water mole fraction distributions. Humidified air is considered in cathode side, however dry hydrogen is considered for anode side. Simulation of interdigitated flow field is done by this work. Numeical simulation results from interdigitated flow field of PEMFC indicate forced convection enhanced mass transport of oxygen which help water removal from reaction zone than conventional flow field. The same comparison works in higher current density in polarization curve. Anode side hydrogen is considered dry which needs to be humidified for proper functioning of membrane. The work did not address the water effect at the interface of GDL-gas flow channel.

A non-isothermal, 3-D model of a PEMFC that evaluates the effect of heat produced in different regions of the cell was presented by Ju, Meng, and Wang (2005). Three sources of heat were considered: irreversible heat (55%) due to electrochemical reaction, entropic heat (35%) due to the difference of total chemical energy of reactants and the maximum usable work, and Joule heating (10%) due to electrolyte ionic resistance. Rather than using the Butler-Volmer (B-V) equation for current density, their work used a simplified form of the B-V equation that assumes the hydrogen oxidation reaction (HOR) that is facile (i.e. surface overpotential will be small), but that the oxygen reduction reaction (ORR) is slow, (i.e. high overpotential). For this work Star-CD software which uses the finite element method was used. A single channel is considered for modeling purposes with conservation equations applied to mass, momentum, species, charge and energy. In addition to that, H_2 and H_2O are considered for anode side species, while O_2 and H_2O are considered for cathode side species. For this model seven regions (GFC, GDL, CL for anode and cathode side and membrane) are considered. The variation of temperature is shown in membrane for different conditions of membrane hydration, different values of the thermal GDL conductivity and different cell voltages. For simplicity purposes, brick types of elements are considered in every region. Their

work found that under low humidity conditions the membrane will dry and performance will be decreased but under fully humidified conditions severe flooding in cathode electrode region will decrease the cell performance. Heat produced from different regions of cells. Their work also found the reasonable phenomena related to fuel cell that under low humidity condition membrane will dry and performance will be decreased and under fully humidity conditions severe flooding in cathode electrode region will decrease the cell performance. This paper deals mostly on heat release from different parts of cell, the work did not exactly address the gas and liquid transport in cell.

Wang and Wang (2005), have conducted a 3D numerical simulation of a 36 channel and 50cm^2 PEMFC. Two immediate flow channels have been considered in counter flow arrangements in cathode side. For this study two cases are considered. For the first case, only molecular diffusion is considered in the GDL. However for the second case, both molecular diffusion and lateral convection is considered in the GDL. In this study a single-phase water model in which the liquid volume fraction is low or liquid droplets are small to form a mist flow. This assumption was predicted on a relatively low humidity operation. An important study by this paper is the determination of water vapor concentration distributions at mid-length cross-section for convection and without convection in the GDL and the GFC. To solve the conservation equations Star-CD software is used with the SIMPLE algorithm. The comparison indicates that making two neighboring channels in counter flow has bypass loss, flow from one channel will go to other channel through GDL, and so, this flow arrangement is ineffective. However, their work recommended that low permeability of GDL would be effective for this kind of counter flow of cathode flow channels arrangement. Thirty six (36) channels with 50cm^2 PEMFC. Making two neighboring channels in counter flow has bypass loss, flow from one channel will go to other channel through GDL. Counter flow arrangement is ineffective. Low permeability of GDL will be effective for counter cathode flow

channels arrangement. Single-phase approach used by this paper is the main limitation of this paper. This paper deals mostly with the comparison of performance between diffusion and convection in GDL, and does not consider liquid water transport in GDL and phenomena involved at the interface of GDL-GFC.

A series of analyses beginning with a 1-D simulation of a PEMFC self written Matlab code based on the finite volume (FV) approach was presented by Coppo (2005). The author has compared his result with experimental results from the literature and found reasonable agreement.

Kulikovsky (2003) has shown various conservation equations for MEA. This study deals mostly water transport through membrane. Figures are provided for membrane side water transport. This study provides detailed discussion of membrane water transport. Therefore, there is no information about gas and liquid transport considering function of all the parts in a cell. Nonlinear diffusion of water transport through membrane and closely located dry and wet regions in the membrane due to nonlinearity has been discussed. Details discussion about membrane water transport is provided by this paper, however water transport in gas flow channel in this paper is not discussed.

In later part, a two-dimensional (2-D) simulation has been performed by Coppo (2005). This study of the simulation was to identify implementation errors that could be spotted and solved more quickly by using 2-D simulation before undertaking a 3-D model. The 2-D model addresses phenomena occurring on a slice of cell cut halfway through channel height. This study tried to see the gradient of different parameters through the cell layers and along the channel. Reasonably, the 2-D model shows higher values than 3-D in polarization curve due to 2-D model has different values that should have to be tuned to get proper values. This study is dealing with working with stability in multiphysics during 1D simulation as well as domain meshing, equation discretisation and linear

system solution during 1D simulation. This work tried to find out implementation errors that could be spotted and solved more quickly by using 2-D simulation. This work tried to see the gradient of different parameters through the cell layers and along the channel. This work has used mathematical equation for water droplet inside gas flow channel in relation with surface tension and drag force when it will be moved inside the channel by air flow. A large part of numerical simulation deals with various transport and electrochemical properties relation with Temperature. In this study, mathematical equation has been derived for water droplet inside gas flow channel in relation with surface tension and drag force when it will be moved inside the channel by airflow. A polarization curve showing advection coefficient (ratio of liquid to gas velocity) effect on performance of cell is shown. The model is a sub case of the full model while considering one-dimensional simulation. Water phase change between liquid and vapor is not considered during one-dimensional (1D) simulation. Two-dimensional (2-D) simulation did not properly address all multiphysics problems.

A finite element analysis (FEA) of two-dimensional water transport in the PEMFC without external humidification of gases (i.e. water is present only due to electrochemical reaction on cathode side) has been presented by Hsing and Futerko (2000). The work addresses five layers: gas flow channels, gas diffusion layers, and membrane. The catalyst layer is treated as an interface between the gas diffusion layer and membrane, which in some reason is not accurate, as the catalyst layer will have a thickness. For that reason, the model does not consider multiphysics comprehensively in that catalyst region. This work has used exponentially spaced nodes and nine-noded biquadratic elements. In this work, hydrogen flow is counter flow with the air flow. In this work streamlines for reactant gases and water and contour plots of water mole fraction in the flow channel and electrodes are presented. Reasonable agreement was found between this simulation work with experimental results from other researchers. Concentrated solution theory is used to

model transport within the membrane. Simplified model has been presented without considering transport limitations within the active catalyst region as it has less impact on results or accuracy. In this study calculation of fraction of product water leaving the anode side of PEMFC with wide range of H_2 and O_2 stoichiometries, current densities and cell temperatures as well as Non-humidified external gases are used. Water formation is considered only by electrochemical reaction in cathode side.

Finite Volume method (FVM) has been used for three-dimensional (3D) domain two-phase, transient PEFC by Wang and Wang (2007). This work mostly deals with dewetting of flooded gas diffusion layer in relation with cell performance. In addition, through plane and in plane drying were considered. In addition to that, different water diffusivity in the anode and cathode are considered. Numerically predicated time constant has been compared with theoretical calculation for in-plane and through-plane drying region. In this work, derived two-phase equations for regions of fuel cell are implemented in the numerical solutions. Different liquid water saturation and water vapor concentration distributions in time instants for side view of midplane-PEMFC have been shown for different time instants and provided information from this work. In this paper dewetting of flooded gas diffusion layer was studied in relation with cell performance. In addition, through-plane and in-plane drying was also considered. Also differing water diffusivity in the anode and cathode are considered. Dewetting enhance performance of the cell up to a certain range, after that performance decreases. More discussion was done on membrane dewetting but, very less work was done on gas and liquid transport in cell as well as at the interface of GDL-GFC.

In another part of Coppo (2005), in his work the catalyst layer model is based on an agglomerate geometry which deals with gas, liquid and dissolved phases. For this work 3D fuel cell simulation were done by CFD code provided by CFDesign by Blue Ridge Numerics, Inc. to simulate

the cell. Numerical results for transported quantities (water content, conductivity, ionic potential, cell current density, hydrogen, water, oxygen, nitrogen mass fraction, saturation etc.) were presented for the various domains (GDL, CL and membrane). Polarization curves are shown the effect of the advection coefficient (ratio of liquid to gas velocity) on the performance of the cell is shown by this study about gas and liquid transport from the GDL-GFC interface to gas flow channel. The numerical simulation used to explore the effect of temperature on the various transport and electrochemical properties.

Interfacial saturation condition for PEMFC for GDL only has been described by Hasan (2007). Complete saturation condition while considering other layers are not considered in this study. Lee and Chu, 2007, has conducted three-dimensional (3-D) numerical simulation using commercial computational fluid dynamics (CFDRC) software to locate the gas-liquid interface for PEMFC for various relative humidity in the cathode gas diffusion layer and gas flow channel. In this study steady state, isothermal model is presented. Oxygen (O_2) fraction, water fraction and liquid water saturation field along the channel are presented. Their results from simulation indicate that, pore is hydrated more with liquid water so, air does not get access to react, as a result, cell performance decreases. Interface of vapor and liquid water are provided by this work. In this study location is made for the gas-liquid interface for PEMFC for various relative humidity in the cathode gas diffusion layer and gas flow channel. This study shows that with increasing relative humidity gas-liquid interface moves from catalyst layer to gas diffusion layer. It is also found that cell performance decreases as water blocks pore spaces to transport fuel gas. However, more equations involved in two-phase water in various porous regions are neglected.

The study done by Chen, Kikner and Noble (2005), provided information for equations derived for predicting the instability of liquid water droplet inside gas flow channel. Simplified model

of cylindrical and spherical shape droplets are derived based on macroscopic force balances and droplet-geometry approximations. This work also conducted some experiments to validate the instability results. Numerical modeling were counted for surface tension effect and drag force and correlation from some other research works were also taken. This work derived equations for cylindrical and spherical droplet. Two-dimensional (2D) Finite element simulations coupled with an arbitrary Lagrange-Eulerian formulation for liquid or gas interface were conducted and flow results over cylindrical droplet were compared with simplified cylindrical droplet model. This work is applicable for one droplet instead of multiple droplets emerging from GDL-GFC interface at any given time and not for real life situation. The onset of droplet instability leads to removal of water droplet at GFC-GDL interface. Droplet visualization experiments are done to observe formation, growth and removal of water droplet. Simplified equations for onset of droplet instability are derived.

Summary of review on literature survey has been conducted to find out reasonable saturation value on the interface of GDL-GFC. Based on literatures for a specified value of 0.6 V cell voltage, average value of saturation at the interface of GDL-GFC is 0.05.

2.3 Conclusion of Literature Survey

Based on literature review it is found that very few works have been attempted in providing complex information for APS application for SOFC manufacturing, adhesion at the interface of thin metal and substrate, Gas flow channel configurations, PEMFC poisoning and recovery, PEMFC single channel, transient temperature during pulse heating, thermal stress in SOFC fabrication and liquid droplet dispersion at the interface of GDL-GFC. Although some papers and works have important information but it becomes clear that all these lack research completeness and details. Research has been conducted with the view to look at complex phenomena of APS application for SOFC manufacturing, adhesion at the interface of thin metal and substrate, Gas flow channel

configurations, PEMFC poisoning and recovery, PEMFC single channel, transient temperature during pulse heating, thermal stress in SOFC fabrication and liquid droplet dispersion at the interface of GDL-GFC.

Application of APS to SOFC manufacturing of different components of fuel cell is widely used in the literature. Concepts that is learned from the literature are used to manufacture SOFC components.

Adhesion of anode and cathode with electrolyte membrane by tensile testing machine by small load cells was not discussed in the literature and gaps or lack of information exist in the literature.

In research literature, very little work has been done to demonstrate systematically, how gas flow channel configurations could affect the PEMFC performance. Therefore, available literature also lacks to find the best performance of a cell using a combination of three basic gas flow channel designs: straight, serpentine and interdigitated.

It has been found that, very little work has been done to demonstrate systematically, how pulse oxygen (O_2) feeding and heating can mitigate PEMFC poisoning and recovery. Also, very little work has been done to demonstrate systematically, how PEMFC single channel can simplify fuel cell simulation, computation time and meshing elements with considering mass, species, electronic, ionic, momentum conservation equations. Very little work has been done to demonstrate systematically, how to mitigate thermal stress in HTVTF during SOFC fabrication by considering air flow and inserting small pipe flow, and heat affected zone (HAZ). Also, there is lack of information to demonstrate systematically, how liquid droplet dispersion at the interface of GDL-GFC can be handled by saturation and capillary pressure slope.

C H A P T E R - 3

FUEL CELL OPERATION AND EXPERIMENTAL ANALYSIS

To address fuel cell performance optimization it is very important to manufacture fuel cell components from raw materials available in the market. Experimental analysis has been conducted with the view to look at complex phenomena of APS application for SOFC manufacturing, adhesion at the interface of thin metal and substrate, Gas flow channel configurations, and PEMFC poisoning and recovery.

3.1 Application of APS to SOFC Manufacturing

In general, components materials in SOFC are composed of different materials. Bipolar plate or Gas Flow channel (GFC) are made of Metallic or ceramic layer, Nickel- and steel-based alloys, doped lanthanum chromites, cermet. Electrolyte is made of Yttria Stabilized Zirconia (YSZ), gadolinium doped ceria (GDC). Anode is made of cermet (Ni mixed with the ceramic material). Cathode is made of lanthanum strontium manganite (LSM), LSM YSZ,perovskite LSCF.

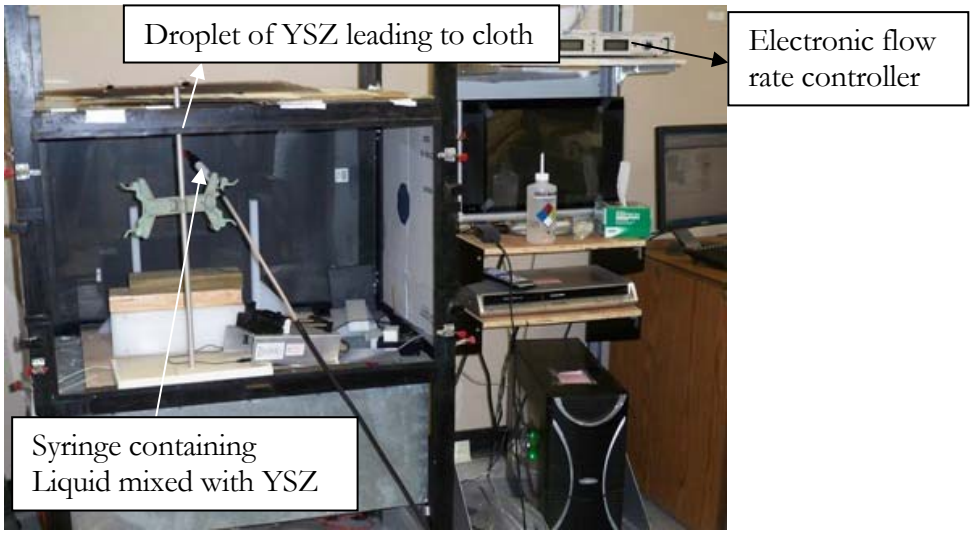

Figure 3.1: Electrospinning

There have been different techniques for SOFC Electrolyte Fabrications: (1) Spraying (2)

Extrusion (3) Electrospinng (4) Tapecasting. Among these methods, spraying using APS is the most convenient way to manufacture SOFC.

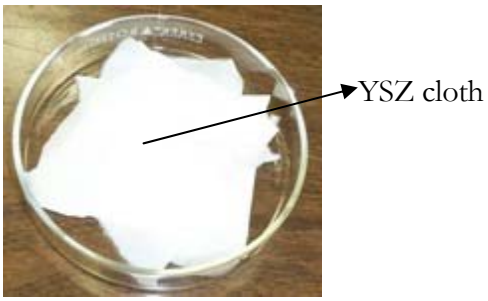

Figure 3.2: YSZ (yttrium-stabilized zirconia) cloth made by electrospinning

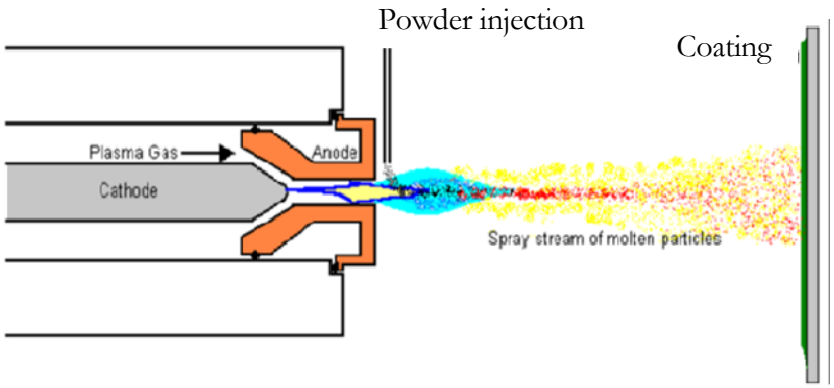

Figure 3.3: Atmospheric Plasma spray by Surface engineering forum

Figure 3.4: Manufactured Alumina using APS (Air Plasma Spray)

Air Plasma-Spray (APS) coating process, a form of thermal spray, uses ionized gas plasma to melt and propel the powdered coating material toward the substrate. It has been used to manufacture solid alumina. Figure-3.3 shows atmospheric plasma spray process. Figure 3.4 shows thin alumina

films that was manufactured by APS.

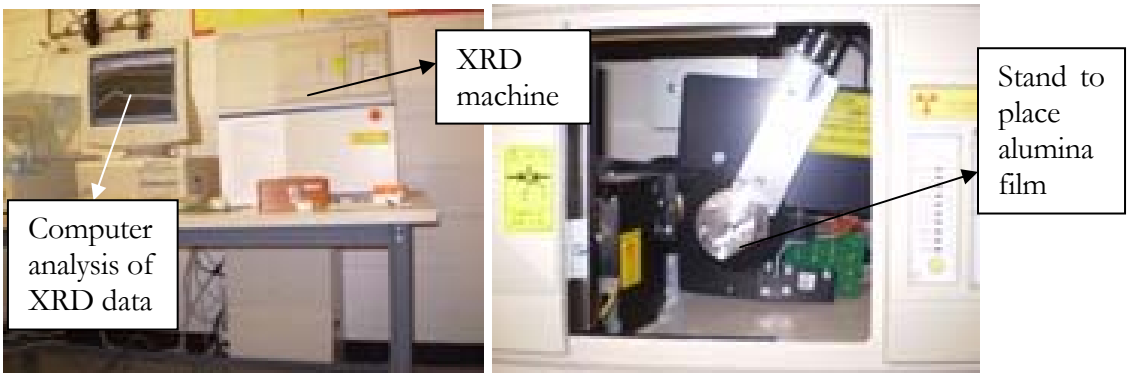

Figure 3.5: XRD machines to analyze crystalline structure

XRD analysis of alumina powder (α-Al_2O_3) was conducted. Rigaku XRD: Ni filtered Cu Kα (λ=1.54056A) machine was used for this study. After APS, α-Al_2O_3 turns to γ-Al_2O_3 and less percentage of α-Al_2O_3. Tests compared with Li, Li, Xing, Gao, and Yang (2006).

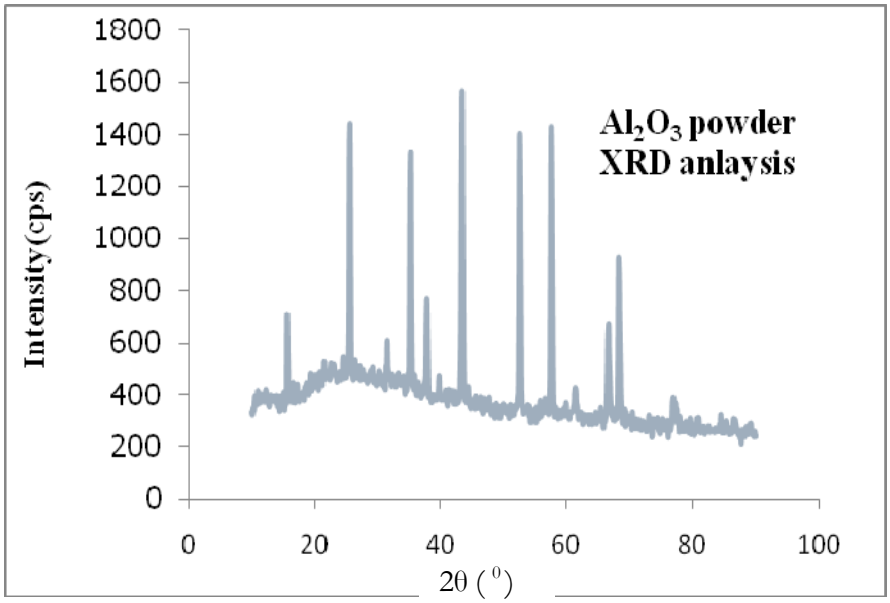

Figure 3.6: XRD of Al_2O_3 powder

This process of manufacturing of alumina is similar to the manufacturing of zirconia (ZrO_2) electrolyte membrane in SOFC. Figure 3.8 shows zirconia powder that can be used for manufacturing of zirconia electrolyte membrane as chemical properties of alumina and zirconia is

similar including their non-heat conduction behavior. However, due to lack of experimental facility, zirconia thin film was not made. However, the preliminary study on alumina is valuable to zirconia electrolyte manufacturing.

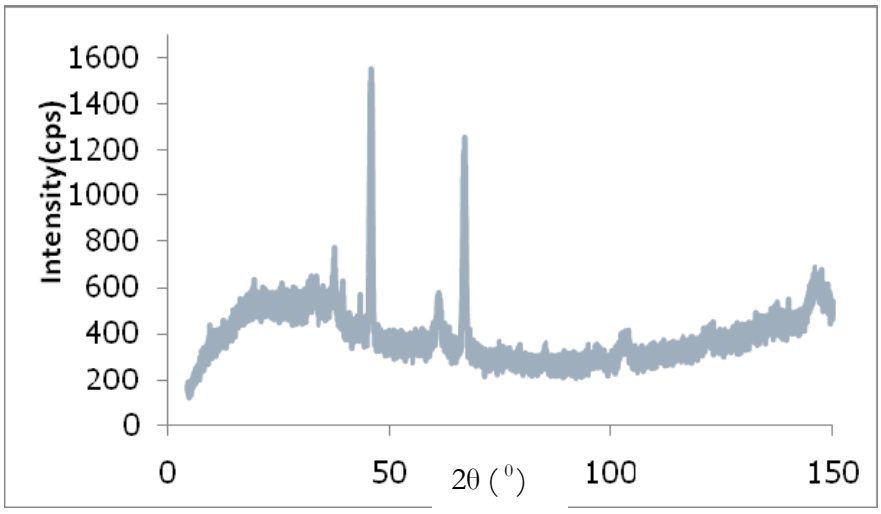

Figure 3.7: XRD of Al_2O_3 thin film after APS

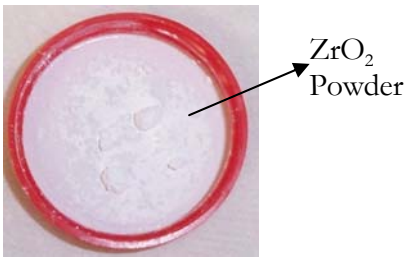

Figure 3.8: ZrO_2 powder

3.2 Anode and Cathode Adhesion with Electrolyte Membrane

It is very important to keep adhesion between anode or cathode and electrolyte. Delamination and debonding between anode and cathode with electrolyte leads to low performance of fuel cell.

Different ways have been used by researchers for testing adhesion. Current adhesion tests to quantify mechanical failure are of two types: (1) Strength tests (2) Fracture tests.

(1)Strength Tests are classified as:

– Lap Shear

– Butt Joint (pull test)

– Cleavage

(2)Fracture Tests are classified as:

– Beam

– Blister

– Peel

In lap shear test, end side of metal film is pulled and energy that is involved to separate the thin metal film from substrate is measured which is converted to adhesion energy. In butt joint (pull test) test end side perpendicular to the position of thin metal film is pulled and energy that is involved to separate the thin metal film from substrate is measured which is converted to adhesion energy. In blister test gas is used to make blister and energy that is involved to separate the thin metal film from substrate is measured which is converted to adhesion energy.

In addition to these tests, needle or wedge probe adhesion tests can be used. Probe test is a quantitative tool for measuring adhesion. Inclined needle-like conical tip probe is used to measure adhesion. Debond is initiated by inserting conical tip at the interface of thin metal film and substrate. Interfacial fracture energy (G_c) (critical strain energy release rate) are used as quantitative measure of adhesion. Wedge test specimens can also be used.

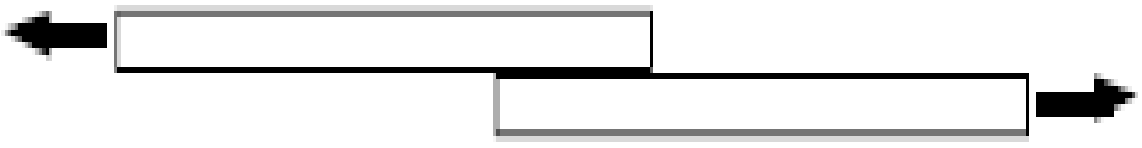

Figure 3.9: Lap shear [MII Lecture, 2007]

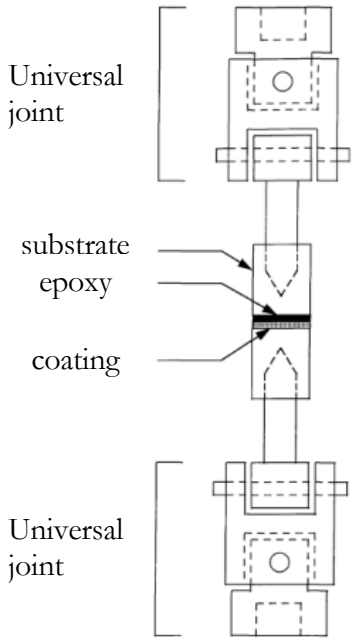

Figure 3.10: Butt joint [MII Lecture, 2007]

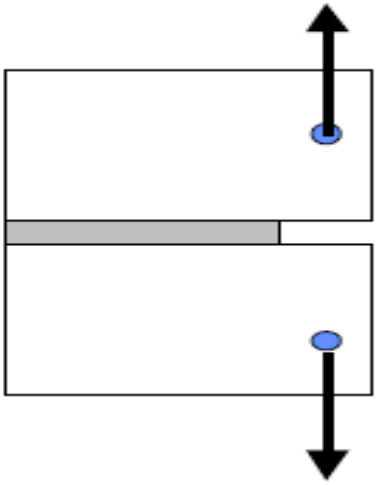

Figure 3.11: Clevage [MII Lecture, 2007]

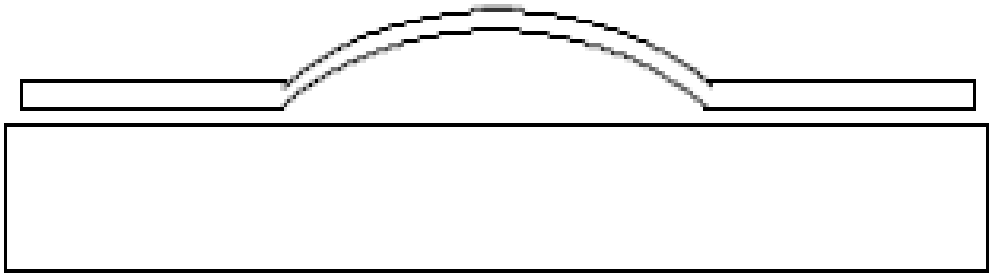

Figure 3.12: Blister [MII Lecture, 2007]

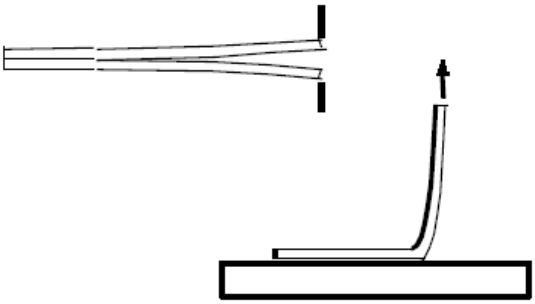

Figure 3.13: Peel [MII Lecture, 2007]

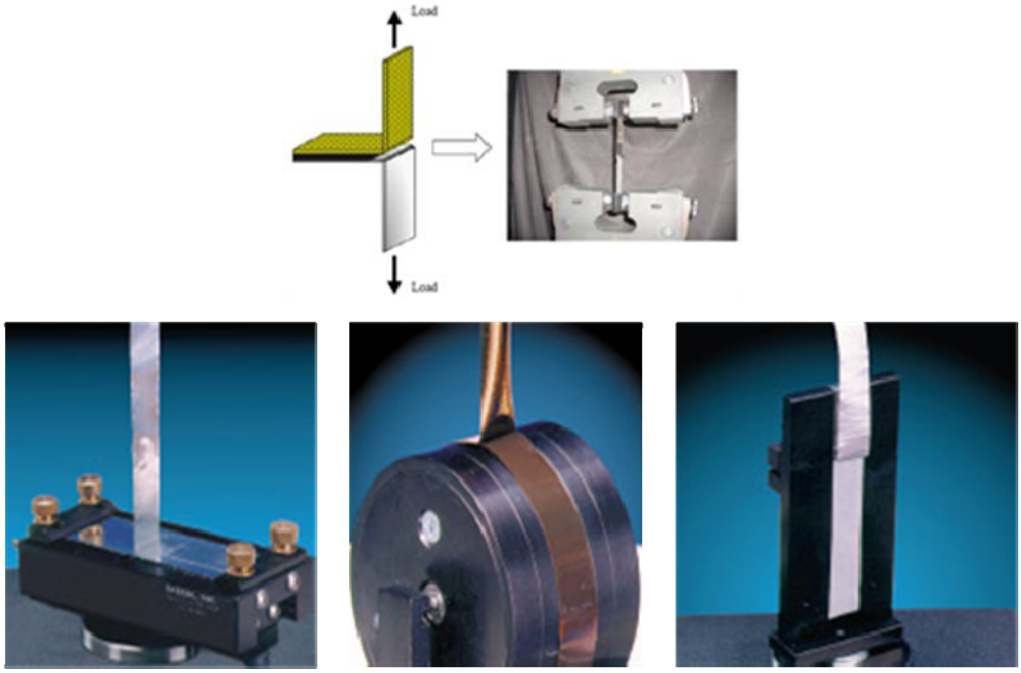

Figure 3.14: Peel test [MII Lecture (2007), Quad Group Inc.]

For T-peel test, Instron machine can be used. T-peel test is tested according to ASTM standard D 1876-01. Several of ways peel test can be conducted are 90^{0}-peel test (for rigid substrate), 90^{0}-peel test (for flexible substrate), 180^{0}-peel test, arbitrary angle (45^{0}) peel test, floating roller test, and climbing drum test.

Instead of traditional methods to find adhesion, for this study different approach has been made for adhesion measurement. Different microfeatures will show different adhesion or bonding capability with ceramic in mechanical testing (tensile, compressive, fatigue, 3-point bend test etc.).

Curves will be found from mechanical testing for different metals adhesion with ceramic. Best material bonding with ceramic will be ideal for the purpose.

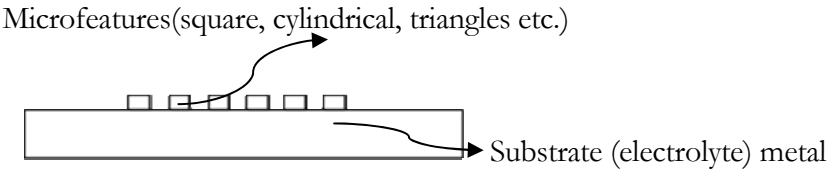

Figure 3.15: Before application of APS ceramic coating (microfeatures above substrate)

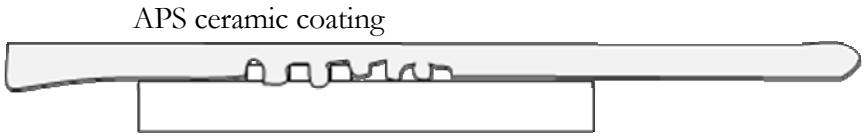

Figure 3.16: After application of ceramic coating (microfeatures above substrate)

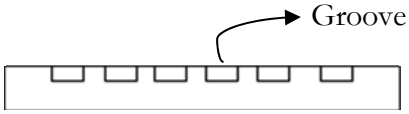

Figure 3.17: Before application of APS ceramic coating (microfeatures as groove)

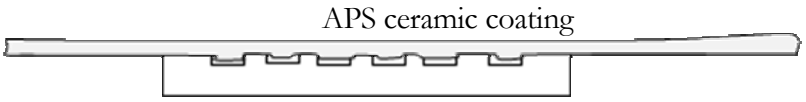

Figure 3.18: After application of ceramic coating (microfeatures as groove)

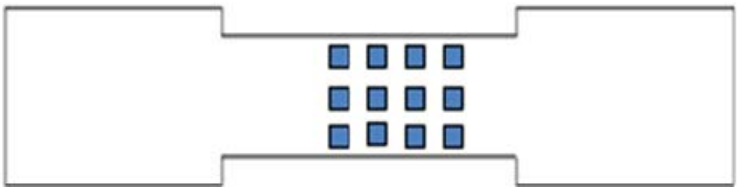

Figure 3.19: Dog bone sample with microfeatures over or grooved surface

For this test fixture for pull test was designed based on tests used for this purpose which are ASTM C 633–01 and ASTM C 633-79.

This works involve : (1) microfabrication (2) maskfabrication (3) metal substrate preparation

(4) resist application and removal. These all are preparation for pull test.

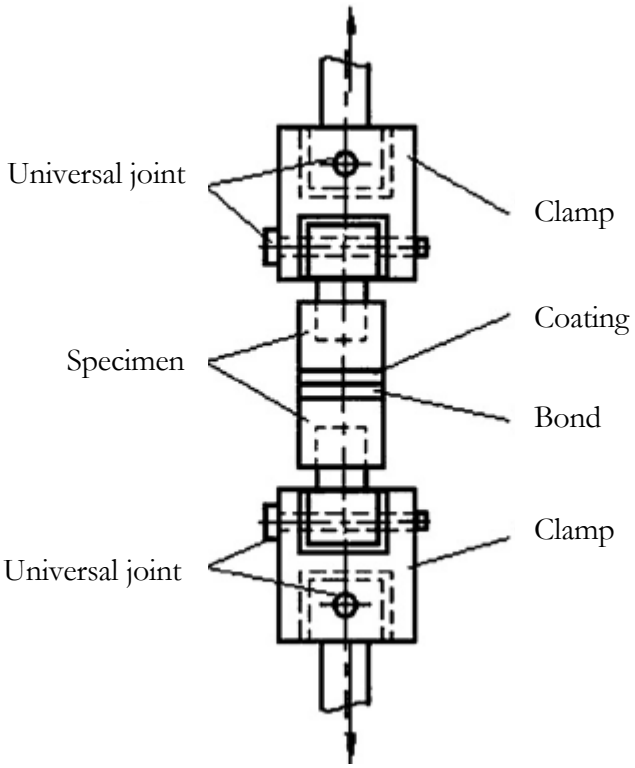

Figure 3.20: Fixture for pull test [by ASTM standard tests]

Photolithography (also known as optical lithography) is a process used in microfabrication to remove parts of a thin film (or the bulk of a substrate) selectively. It uses light to transfer a geometric pattern from a photomask to a light-sensitive chemical (photoresist, or simply "resist") on the substrate. A series of chemical treatments then engraves the exposure pattern into the material underneath the photoresist. In a complex integrated circuit (for example, modern CMOS), a wafer will go through the photolithographic cycle up to 50 times. Photolithography shares some fundamental principles with photography, in that the pattern is created by exposing it to light, using either a projected image or an optical mask. It requires extremely clean operating conditions.

The photolithography fabrication technique was utilized to generate the substrate patterns. The first step was to create a photomask of the pattern, for using in the photolithography process.

The desired pattern was drawn in AutoCAD and converted to Mann 3600 pattern generator format. The feature size for each of the patterns was two and half (2.5) mm, five (5) mm, and ten (10) mm and small sizes of five (5) μm and ten (10) μm. The pattern generator was run for one day and four hours to expose the blank photomask based on design. The mask was then developed, chrome etched and stripped to generate the finished photomask.

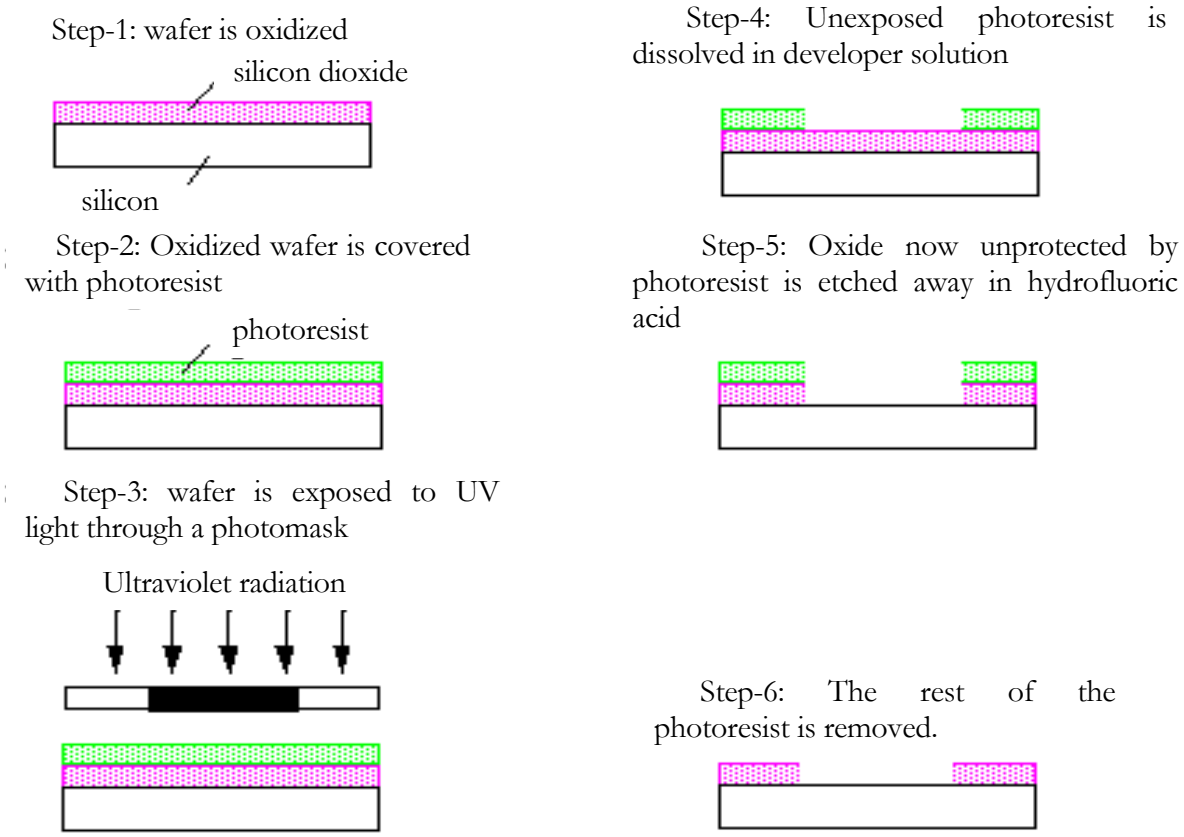

Figure 3.21: Photolithography techniques [by Microelectronics Manufacturing]

At the temperature of 25 °C the etch rate is 30 Å/sec and at the etch rate of 45 Å/sec for aluminum metal substrate. The etch rate is 105 Å/sec at temperature of 30°C for Stainless Steel (AISI 316 grade) metal substrate.

The complete process of making groove inside substrate surface from using positive photoresist up to groove making is shown in figure-3.23 from step (a) to (g). Metal rod is shown in

(a), positive photoresist is placed over metal rod is shown in (b), UV light shines the desired pattern over the surface of metal rod as shown in (c), two-dimensional (2D) drawing of this metal rod is shown in (d), groove inside pattern is made after application of developer solution is shown in (e), groove that was made inside substrate after application of etchant is shown in (f), and finally three dimensional (3D) drawing of the groove inside surface is shown in figure (g).

Figure 3.22: Cylindrical fixture for pull test

For metallic and metallic matrix coating (adhesion is approxiately 55MPa) adhesive bonding agents that can be used are CONAP-1222, CONAP Inc. and for Ceramic or metallic (ahesion is approxiately 28MPa) adhesive bonding agents that can be used are Bondmaster-M666 and Bondmaster-M777. Manufacturer of bonding agents are Epon 911F by Shell Chemical Co., Armstrong A-12 by Armstrong Products Co., and Hysol XA7-H368 Grey by Hysol Inc.

To compare bonding strength data that can be obtained from this application are tabulated in table 3.1. Primary AutoCAD drawings for making photomask by using pattern generator are shown in figure 3.24 and 3.25 with square shape objects.

A thousand (1000) μm (= 1 mm) size can occupy 49 squares over 1" cylinder surface. It is calculated that ten (10) μm size can occupy 4900 squares in the same diameter. In general, the pattern machine does 5000 flashes/hour on average for flash count. Which indicates that a single flashe duration of 225 msec occur for every opening of shutter.

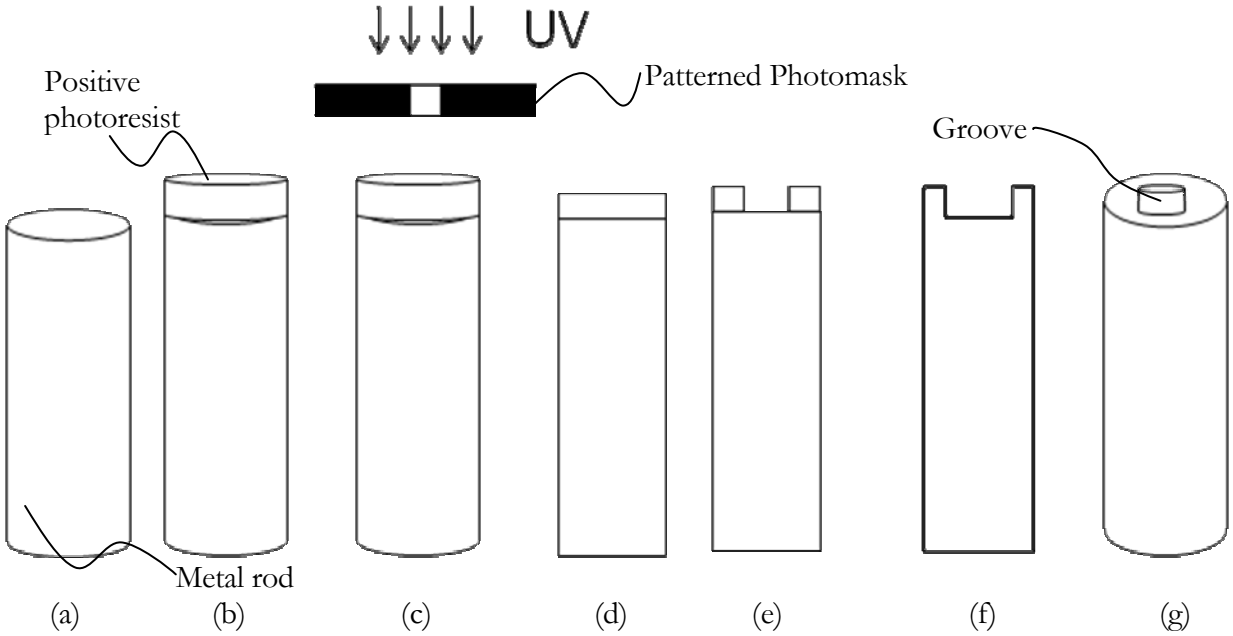

Figure 3.23: Process of photolithography positive photoresist for making groove: (a) polished rod, (b) rod with positive photoresist, (c) rod exposed by UV light, (d) 2D side view of the rod, (e) after application of developer solution (f) after application of etchant (g) rod with groove

Prior to the photolithography process the cylindrical, foil, plate and dog bone alloy of Al and low carbon steel rod and sheet were cut in proper shapes and dimensions. Al and low carbon steel were chosen because of Transene Al and Ni etch could be used to etch the substrate pattern. In the cleanroom at CAMD (Center for Advanced Microstructures & Devices, Baton Rouge, LA), the square plate, foil and cylindrical substrates were loaded into the heavy-duty resist spinner (figure-3.29) to coat the surface with Shipley 1827 photoresist(figure-3.30). These were baked softly on a hot plate (figure-3.31) or convection oven (figure-3.32) for 10 minutes to ensure the resist would not stick to the mask. At the Oriel UV exposure station or aligner (figure-3.33), the mask was placed on

top of the substrates and exposed for 25 seconds. The resist patterned Al and low carbon steel were revealed by submersion in Microposit 351 developer. The substrates were then taken to create the patterns. After that, the substrates were placed in the Al and Ni etch in acid station (figure-3.34) and agitated for approximately 15 min. Acetone was then used to strip the remaining resist from the substrates. This results in substrates with square or quadrilateral patterns with different depths of removed material as revealed by high resolution Nikon Optiphot-88 optical microscope or image capture (figure-3.35). The completed substrates, shown in the figures below, are ready for ceramic plasma spray coating.

Table 3.1: Bonding strength data

Coating	**Substrate**	**Bond strength (MPa)**	**Work information**	**Sublayer**
$Fe_{67.5}Ni_{23.5}B_9$ alloy	$_1Cr_{18}Ni_9Ti$ stainless steel	42.5MPa	Yang and Li (2008)	Ni–Al alloy (Ni/Al: 2:8 wt.%)
NiCrAl 25/9 FeCrAlMo 25/9/3 WC+10% Ni WC+15% Ni WC+25% Ni WC+15% Co	Al alloys PA6 (Cu: 3.5%, Mn: 0.4–1%, Mg: 0.4–1%, Si: 0.2–0.8%, Fe: 0.7%, Cr: 0.1%, Zn: 0.25%, Al balance) and AK12 (Si: 11.5–13%, Cu: 0.8–1.5%, Mg: 0.8–1.5%, Ni: 0.8–1.5%, Fe: 0.8%, Al balance)	20MPa 30MPa 280MPa 28MPa 32MPa 20MPa	Białucki and Kozerski (2006)	N.A.
aluminum bronze (900 C, 1 h)	Mild steel	28.4 MPa	Li, De-yuan, Shui-yong (2006)	N.A.

Figure 3.36 shows ten (10) microns square photomask after Cr etching. The yellow part shows groove in Cr part and the black one shows Cr part.

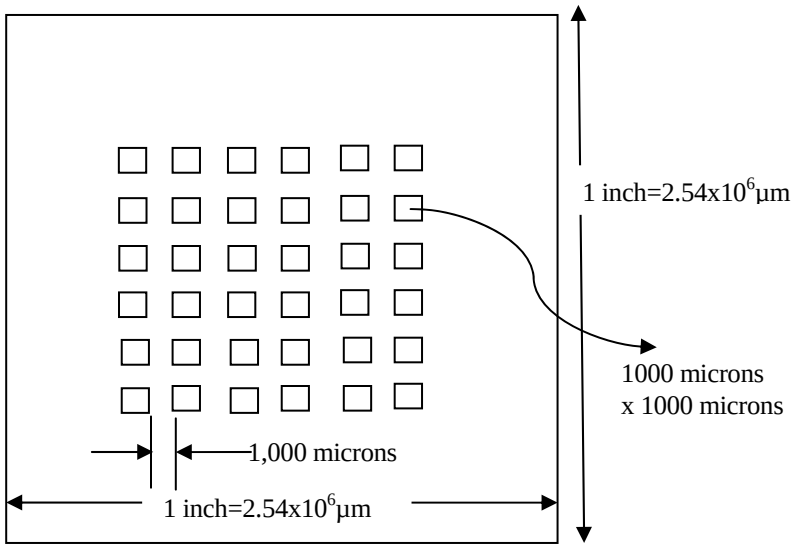

Figure 3.24: Photomask drawing by AutoCAD2008

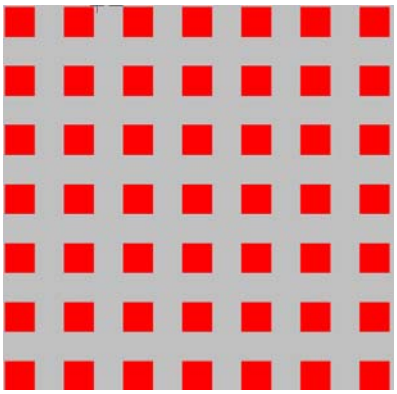

Figure 3.25: AutoCAD drawing after conversion for pattern generator

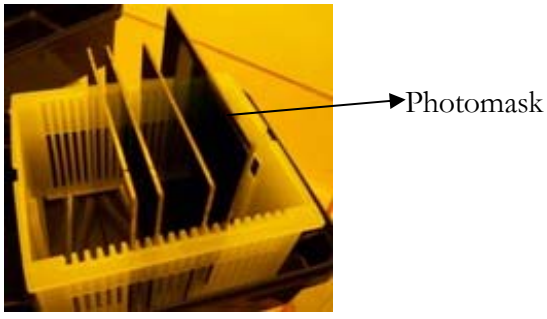

Figure 3.26: Photomask from Nanofilm

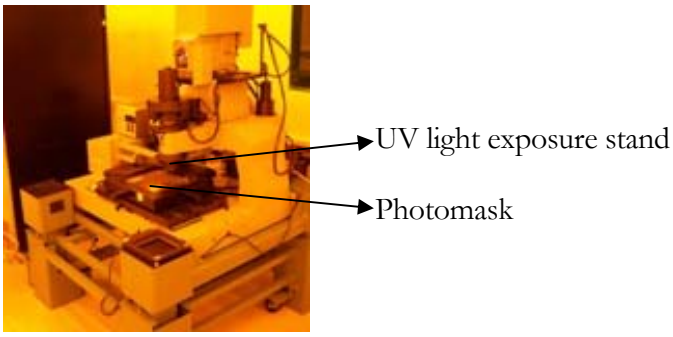

Figure 3.27: Pattern generator for pattern making

Figure 3.28: Hood for developing mask

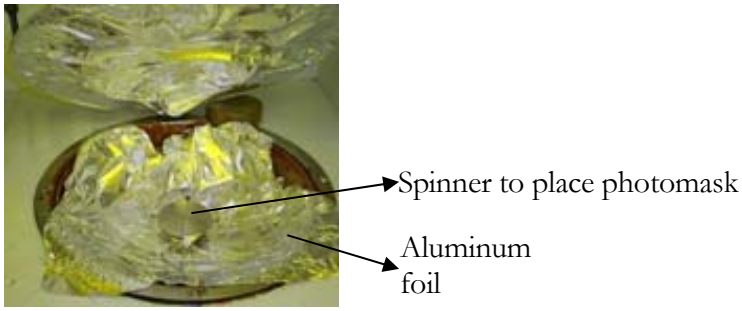

Figure 3.29: Spinner for uniform photoresist making

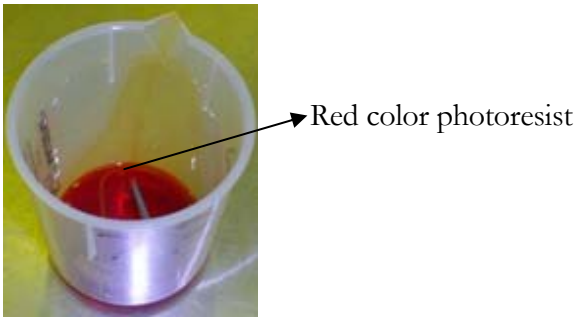

Figure 3.30: Photoresist

Figure 3.31: Hot plate station

Figure 3.32: Convection oven

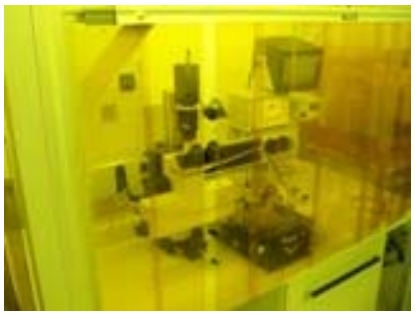

Figure 3.33: UV exposure station

Figure 3.34: Acid station for etching

Figure 3.35: Microscopic observation

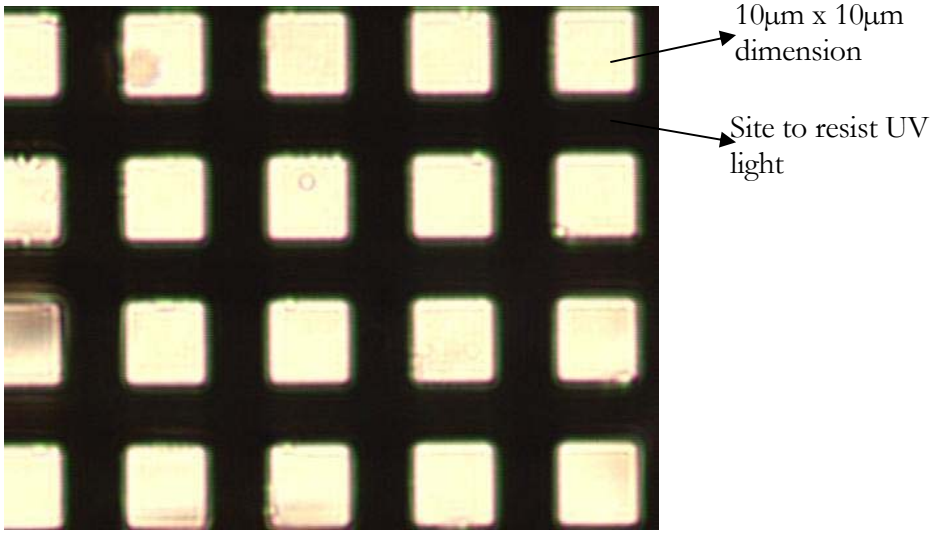

Figure 3.36: Microscopic view of 10 microns square photomask

In the figure 3.37 shows five (5) microns photomask under the microscope and the actual design. Before microfabrication manufacturing substrate (electrolyte) cleaning was conducted. Bench top grinding and cleaning machine are used for metal cleaning. Figures 3.38 and 3.39 shows bench top grinding machine.

Different grit size papers were considered for polishing. Table below shows grit size with average particle diameter. It shows that higher grit size will have smaller particle diameter to get a smooth finish and vice versa. At first, work is started with the lower grit size papers (higher particle diameter) to get high rate of polish and later, moved to the higher grit size paper for smooth mirror like finish. After that, microfeatures or groove over substrate was made.

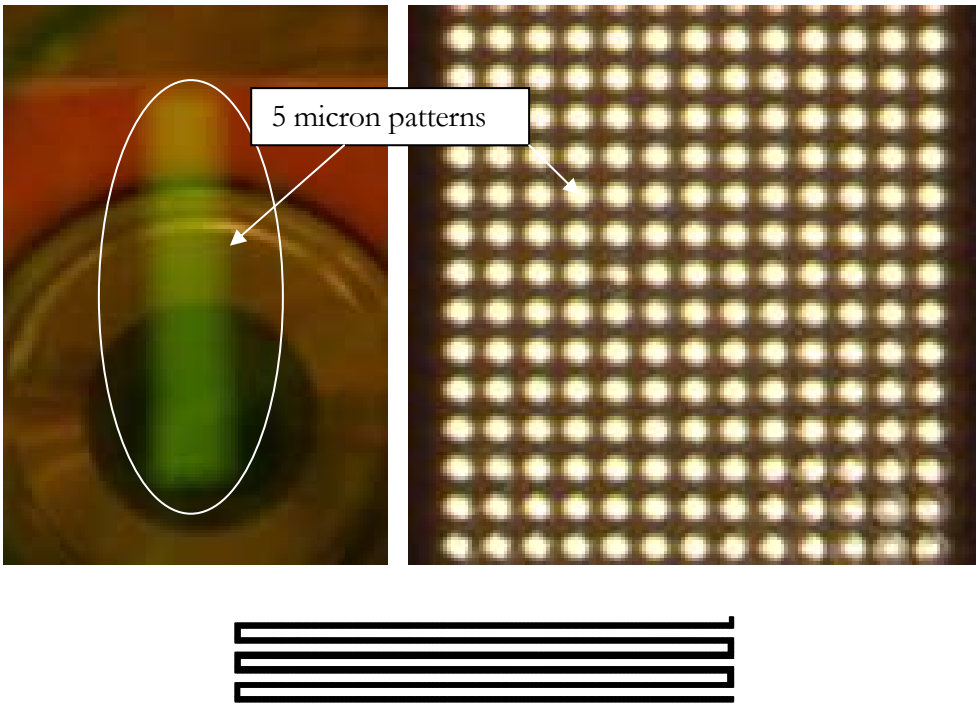

Figure 3.37: Actual design with 5 microns square patterns

Figure 3.38: Bench top hand grinding machine

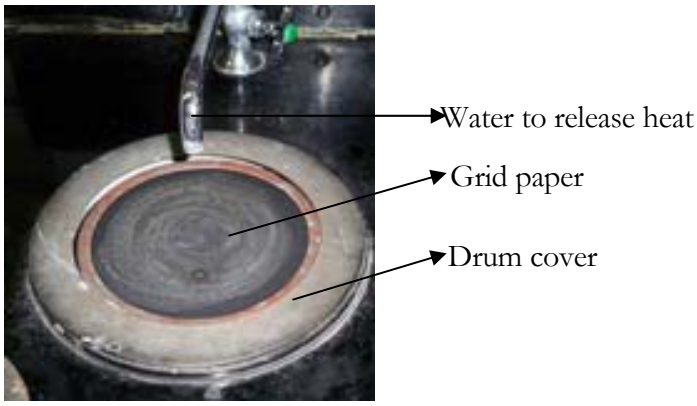

Figure 3.39: Drum type bench top grinding machine

Table 3.2: Grit size relation with average particle diameter

	CAMI Grit designation	**Average particle diameter (μm)**
MACROGRITS		
Extra Coarse	24	708
	30	632
	36	530
Coarse	40	425
	50	348
Medium	60	265
	80	190
Fine	100	140
	120	115
Very Fine	150	92
	180	82
	220	68
MICROGRITS		
Very Fine	240	53.0
Extra fine	320	36.0
	360	28.0
Super fine	400	23.0
	500	20.0
	600	16.0
Ultra fine	800	12.6
	1000	10.3

At first cylindrical Al and low carbon steel rod have been cut with 2" length and 1" diameter. After that, photolithography technique has been used for making groove inside the top surface of cylinder. Figure 3.40 shows Ni and Al etchants that were used for groove or microfeature making purposes.

Tables 3.3 and 3.4 lists Ni and Al etchants specification including etch rate. From these data, it indicates that very high amount of etching as well as groove inside substrate metal can be done within a reasonable amount of time. Tables 3.5 and 3.6 shows low carbon steel mechanical properties and as well as specifications and components.

Figure 3.40: Ni and Al etchants

Table 3.3: Ni etchant

Operating Temperature	30-60 °C
Tank	Glass
Rinse	Water
Etch Rate- Stainless Steel (AISI 316 grade)	45 Å/sec @ 25°C 105 Å/sec @ 30°C
Etch Rate- Stainless Steel (AISI 304 grade)	500 Å/sec @ 45°C
Agitation	Continuous, mild

Table 3.4: Al etchant

Appearance	clear colorless
pH	1.0
Boiling Point	> 100 °C
Freezing Point	< 0 °C
Sp. Gr. @ 25 °C	1.45
Flash Point	Non-flammable
Solubility	Miscible with H_20
Etch Rate at	
25 °C	30 Å/sec.
40 °C	80 Å/sec

Table 3.5: Low carbon steel mechanical characteristics

Alloy	1018
Material	General-Purpose Low-Carbon Steel
Low-Carbon Steel Type	1018 Carbon Steel
Finish/Coating	Unpolished (Mill)
Hardness	Brinell 126-167
Maximum Attainable Hardness	Rockwell C60-C62
Yield Strength	54,000 to 70,000 psi
Melting Point	2700°F
Specifications Met	American Society for Testing and Materials (ASTM)
ASTM Specification	ASTM A108

Table 3.6: Low carbon steel specifications

Carbon, C	0.14 - 0.20 %
Iron, Fe	98.81 - 99.26 %
Manganese, Mn	0.60 - 0.90 %
Phosphorous, P	<= 0.040 %
Sulfur, S	<= 0.050 %

In general, adhesion of an anode and cathode to electrolyte is strongly dependent on chemical nature, cleanliness, and microscopic topography of electrolyte surface. Adhesion of anode or cathode can be improved by using a fine-grained electrolyte or an electrolyte precoated with suitable materials. Adhesion is better for higher values of adsorption energy of the thin metal film. However, for this study precoated thin metal film is not used.

To test the thin film adhesion with substrate Al and low carbon steel have been placed for a long time inside etching fluids to perform high amount of etching. Figure 3.41 shows these cylinder with actual dimension of the cylinder. Using the photoresist spinner was a problem for this case. So thin film photoresist is poured over the surface of cylinders and heated up to make a solid surface.

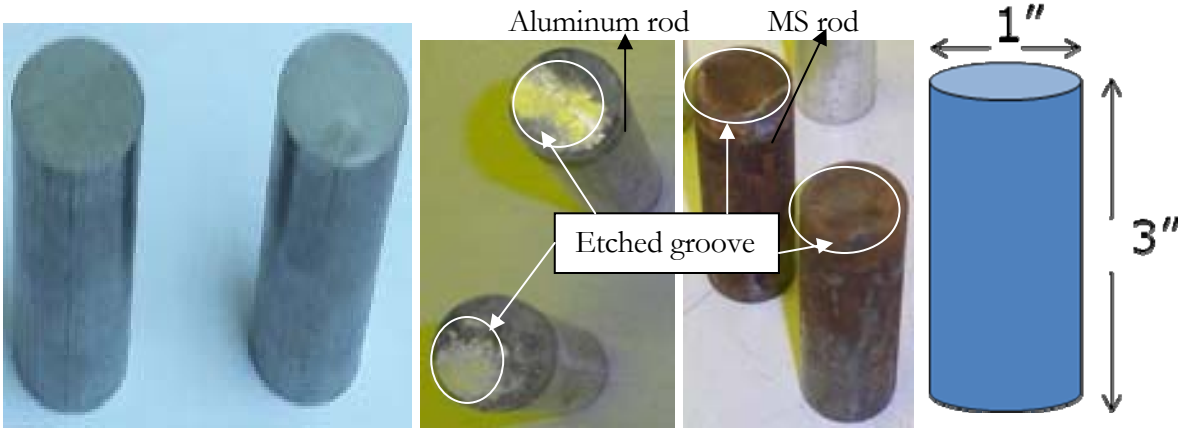

Figure 3.41: Al and MS rod before and after etching

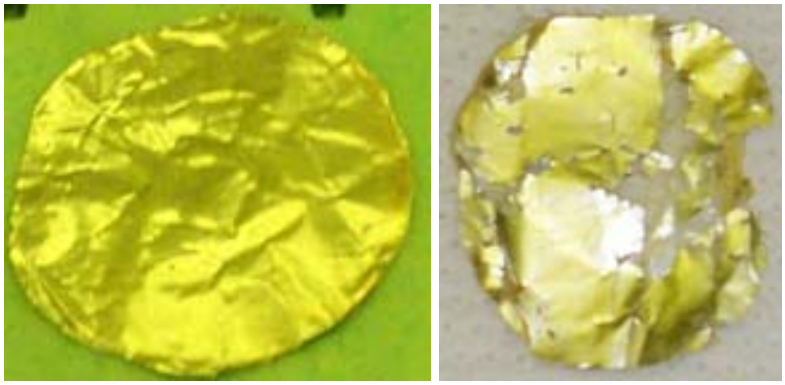

Figure 3.42: Al foil before and after etching

Due to the problem of bigger height of cylinders placing it in UV light exposure station and measuring groove surface by stylus probe, Al foil has been considered for etching. The results that have been found indicated that etching it for one day made very high amount of etching, which is shown in figure 3.42.

Due to proper handling, Al foil during photolithography process as it wraps up quickly, Al plate has been used dimension of $1inch^2$ and 1 cm thickness. This plate was suitable height for measuring grooved surface and UV exposed. In addition, spinner application to photoresist is turned to easier due to Al plate application. For patterns of 2.5, 5 and 10 mm squares etching has been conducted and shown in figure 3.43.

Later low carbon steel has been analyzed. Photolithography technique has been used in the same way that was discussed during aluminum etching. This time for low carbon steel plate five (5) mm quadrilateral groove has been made. For dog bone sample, three 2.5 mm quadrilateral grooves have been made over its surface.

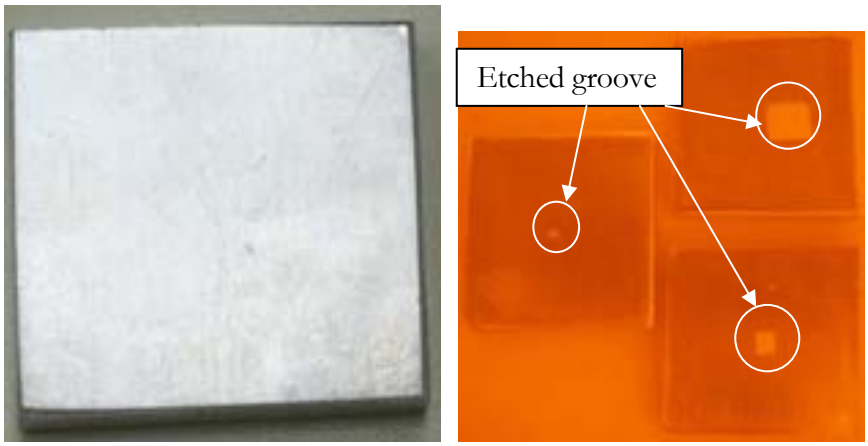

Figure 3.43: Al plate before and after etching

Surface groove is measured with stylus probe profiler and found 40 microns on average depth for these samples. Figure 3.45 shows surface roughness of the groove as obtained from stylus profiler.

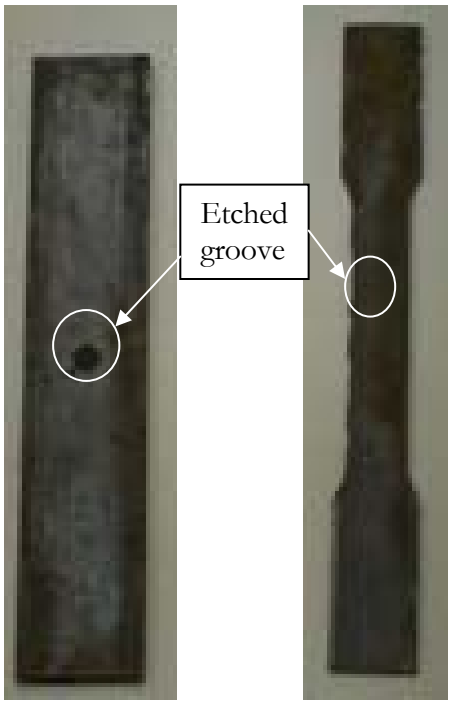

Figure 3.44: MS dog bone and plate etching

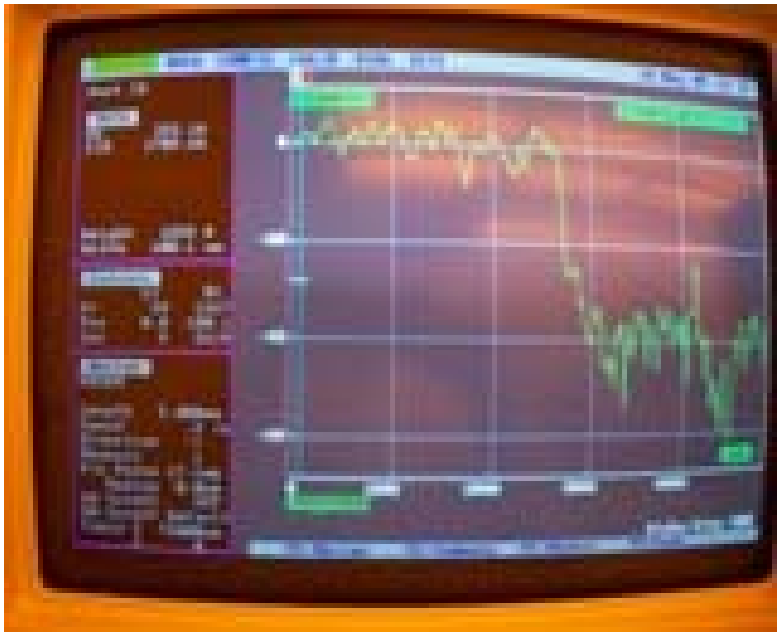

Figure 3.45: Roughness value

A ten (10) microns square groove for plate and cylinder under microscope is showing in figure-3.46 and figure-3.47.

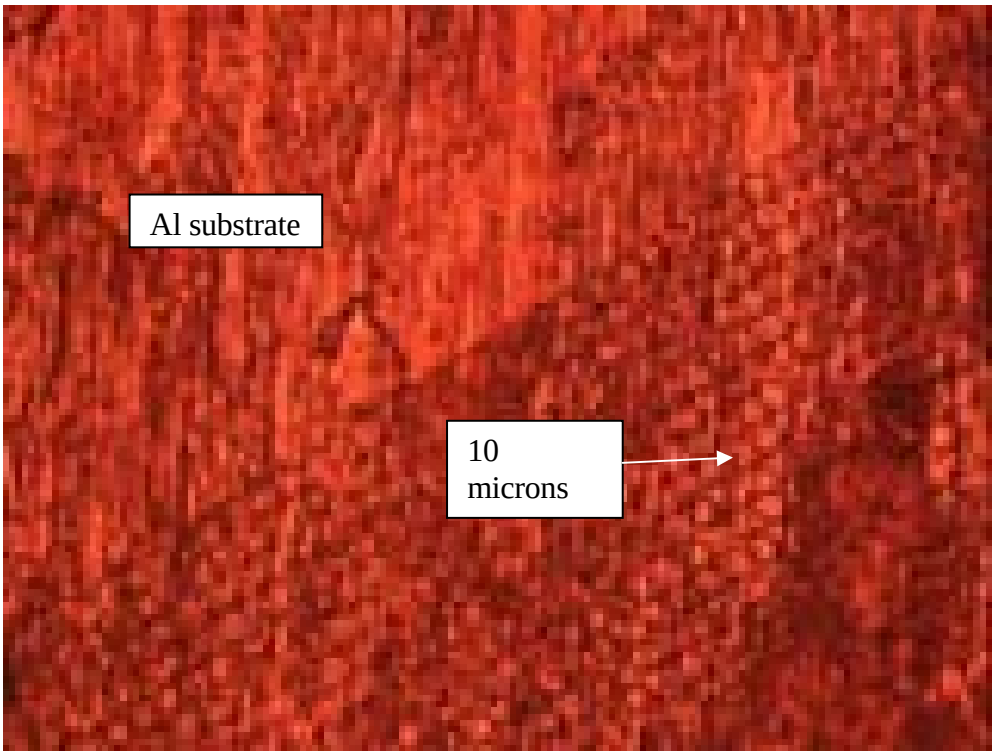

Figure 3.46: 10 microns groove over Al substrate plate (10X magnification)

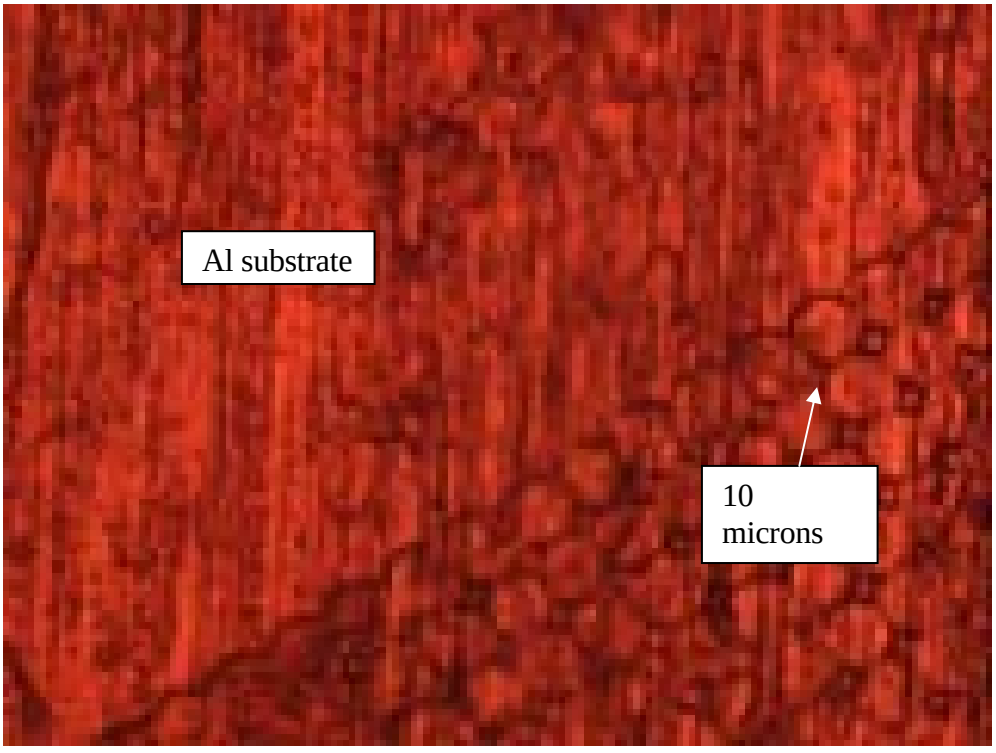

Figure 3.47: 10 microns groove over Al substrate plate (25X magnification)

After completion of making groove and placing it in stylus profiler, the substrate (electrolyte) roughness value is measured. Among different ways to measure surface roughness, stylus profiler is used for substrate roughness. Figure 3.48 and 3.49 shows Tencor Alpha-Step 500 surface profiler stylus probe while monitoring of surface roughness and groove surface.

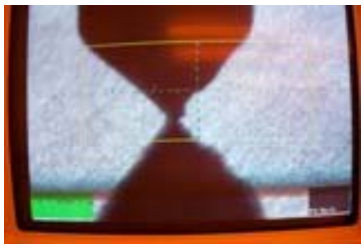

Figure 3.48: Stylus probe to measure roughness of substrate

Figure 3.49: Stylus profiler is used for surface roughness

Figure 3.50: MTS testing machine

Then ceramic layer can be deposited over these samples and suitable to perform mechanical testing. Small load cell to conduct various tests can be used for this purpose. Due to lack of experimental facilities, this work is not extended but the concept can be valuable for engineering communities to deal with complex adhesion problem.

3.2.1 Conclusion on Anode and Cathode Adhesion with Electrolyte Membrane

Different sizes of feature grooves have been made over substrate. The depth of groove for etching is satisfactory for APS experiment. Microfeatures over surface are made using negative photoresist. Information provided here can be useful to deal with complex adhesion problem.

3.3 Gas Flow Channel Configurations

In general, there are three designs of gas flow channels available in the market [Wilson, Springer, Davey, and Gottesfeld (1995), Gottesfield, Halpert, and Landgrebe, and Um, and Wang (2000), and Mench, Boslet, Thynell, Scott, and Wang (2001)]: serpentine (denoted as 'S'), straight (denoted as 'St') and interdigitated channel (denoted as 'I'), which are shown in figure 3.51. In this study, straight and interdigitated gas flow channels were conveniently produced by modifying the pre-existing market-available serpentine type gas flow channels. For all tests, a commercially available five-layer (gas diffusion layer in both sides of anode and cathode, in the middle electrolyte, and catalyst layer in both sides) Membrane-Electrode Assembly (MEA) was used. The MEA area is 5.05 cm by 4.95 cm. Hydrogen and oxygen flow through anode and cathode in a co-flow manner; i.e., both flows are parallel and in the same direction. Laboratory temperature was air-conditioned at 21°C. The pressure of oxygen and hydrogen in the cell was close to ambient pressure.

The gas flow channel block has an outer dimension of 7.65 cm by 7.65 cm, and has a thickness of 1.3 cm. The gas flow channels have a width of 1 mm and a depth of 1 mm. The fuel

cell was connected to variable load resistors to observe the variation of cell performance with loads. In total twelve (12) resistors: four 0.68 ohm, two 0.56 ohm, two 0.39 ohm, and four 0.27 ohm were used to form the load bank. By connecting some or all of these resistors in serial or parallel manner, different loadings conditions were achieved.

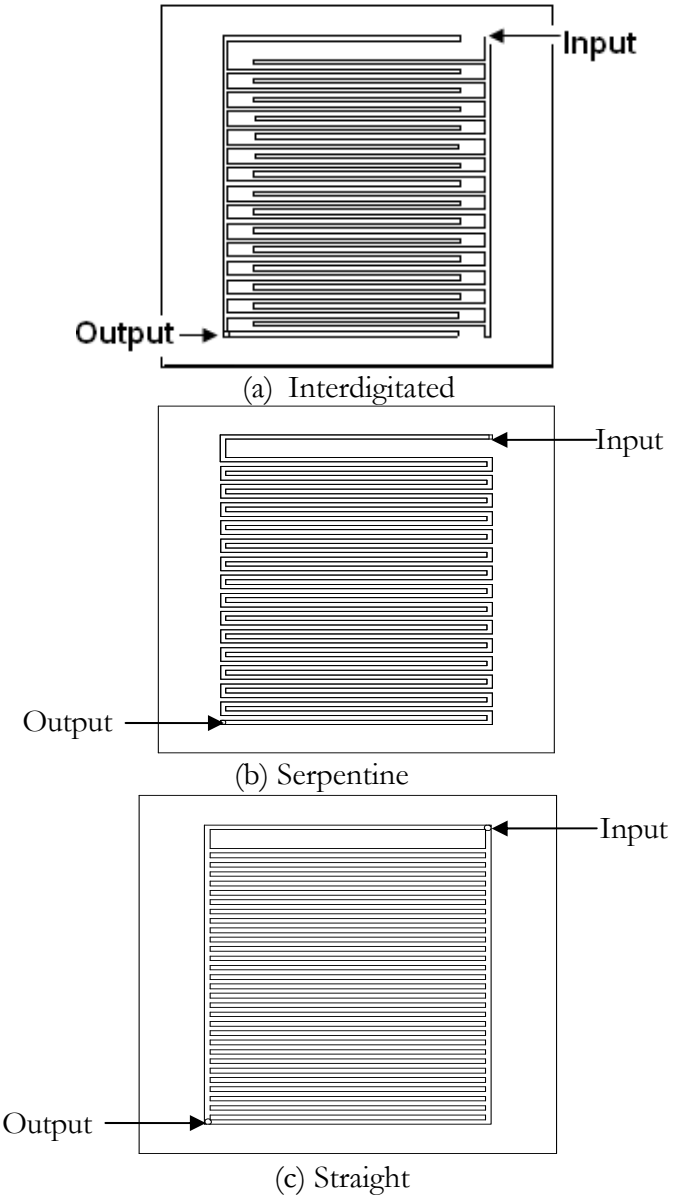

Figure 3.51: (a) Interdigitated (b) Serpentine (c) Straight bipolar plate

Overall schematic as well as block diagram of the experimental setup is shown in Figure 3.52. Unused oxygen was released at the cathode side outlet port. No suction device was used in

the oxygen outlet port and oxygen was free to release outside and mix with the outside ambient air. However, the hydrogen outlet port was connected via a long tube with a laboratory hood for rapid removal of unused hydrogen gas from the lab. As hydrogen is a potentially dangerous combustible gas, so this precaution was necessary.

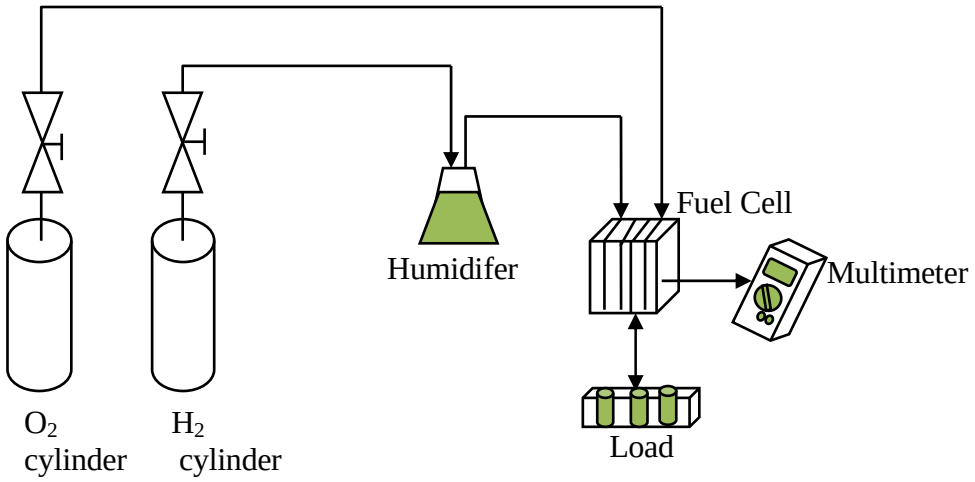

Figure 3.52: Test station

The gas flow rate of hydrogen was varied in the tests to observe cell performance dependence. However, the oxygen flow rate was maintained constant at 46 sccm (standard cubic centimeters per minute) for all the tests. The fuel cell output voltage was monitored using a multimeter. The cell current is obtained by calculating the measured voltage divided by the relevant resistance that was involved; and the cell power is obtained by multiplying the current density and the voltage data that were obtained. The testing cell is inserted with two cartridge heaters for maintaining an elevated operating temperature. To avoid the overheating of the cell and membrane-thermocouple, readings were taken from the testing cell when these heaters were used.

For the straight gas flow channel, once the gases enter the channel, they will try to find the shortest way to release from fuel cell. Therefore, the gas flow distribution in the straight gas flow channel is unlikely to be uniform. For serpentine gas flow channel, gases have to follow the direction

of the serpentine channel. Due to the relatively defined gas flow path and a long travel distance, high-pressure losses are expected for the serpentine design. Interdigitated gas flow channel forces the fluid to go inside the porous gas diffusion layer towards the membrane. Therefore, high fuel or oxidant partial pressure at the three-phase region is expected and the fuel might be used more efficiently.

Efficient hydrogen utilization of a cell is a prime criterion for fuel cell performance. Hydrogen utilization is defined as the ratio of the theoretical flow rate and experimental flow rate of hydrogen into the cell. The experimental flow rate of hydrogen is obtained from the flow meter reading and the theoretical flow rate of hydrogen is calculated from the measured cell power output. After analyzing experimental results, it is found that all gas flow channel configurations show a similar trend in hydrogen utilization. Moreover, data shows that under high load, the interdigitated gas flow channel in anode side and serpentine gas flow channel in cathode side show slight improvement of hydrogen utilization.

P-I (Power-Current) and V-I (Voltage-Current) relations at 21ºC operating temperature using serpentine gas flow channel at the anode and cathode sides are observed for various flow rates of hydrogen. As the local current density (I) is a function of hydrogen and oxygen partial pressure, increasing the fuel flow rate will increase the partial pressure at the later portion of fuel flow channels, thus improving the performance of the cell. Accordingly, from the data it is observed that at the fuel flow rate of 100 sccm, the maximum current density is three times that of 20-sccm.

Figure 3.55 shows voltage-current density relations for 60sccm flow rate of H_2 and 21ºC operating temperature for various arrangements of gas flow channels. Experiments were conducted for nine (9) combinations of gas flow channel arrangements. Also for lower gas flow rates, V-I relations at 20 sccm flow rate and 21ºC operating temperature for various arrangements of gas flow channels are shown in Figure 3.54. Based on these results, the interdigitated gas flow channel in the

anode side and the serpentine gas flow channel in the cathode side show the best performance out of all gas flow channel configurations that were studied. In the same way, V-I curves under hydrogen flow rates of 40, 80 (as shown in Figure 3.56) and 100 sccm and at 21ºC operating temperature for various arrangements of gas flow channels are observed. Again, the interdigitated gas flow channel in the anode side and the serpentine gas flow channel in the cathode side have the best performance.

The amount of water at a particular location may not block the gas flow channel completely, and the water pattern along the flow channel may not represent the water flooding in the gas diffusion layer. A uniform water pattern in the middle of the gas flow channel region may provide adequate water to saturate the membrane and thus make it function properly. For the case of an interdigitated channel in the cathode side, the water flooding in the channels occurs near the inlet port, and water in those places introduces hindrance to the flow. The oxygen flow rate is not large enough to blow them through the channels, resulting in an undesirable cell performance. For the case where the anode side is the straight channel, water pattern is observed almost everywhere in the exit portion of flow channel. Here, hydrogen will try to take the shortest distance to find the exit port situated at the lower channels. This result in greater water generation in the upper part, so water will flow from the upper part to the lower, causing water jamming in the lower part. In another case, when the Straight gas flow channel is used at the cathode side, and the Interdigitated gas flow channel at the anode side, it will lead to small patches of localized flooding patterns in the gas flow channels. Images and results of the cell performance have shown that this configuration is better under high loading. These results also indicate that the serpentine at the cathode side and the interdigitated at the anode side will show best water flooding pattern.

To operate the cell effectively, it is very important to humidify or wet the membrane. However, too much humidification of the membrane may cause water flooding, which can lead to

low performance of the cell. For that reason, the performance of the cell was also tested with and without the use of the humidifier. Under high load, more water generation and stronger transportation of water from the anode to the cathodes, due to the electro-osmotic drag, makes the use of a humidifier unnecessary in the cathode side.

After operating the fuel cell at high current density until it showed steady data in multimeter, the cell was opened, and the patterns of water flooding in the cathode side gas flow channels were photographed. Table 3.8 lists the percentage of area covered by water in the flow channel for different combinations of gas flow channel arrangements. All combinations appear to have wet areas along the gas flow channels. Water is generated due to the reaction of hydrogen and oxygen, and water particles are carried by electro-osmotic drag from the anode towards the cathode. After observing water flooding and percentage of water in the cell from Table 3.8, it is found that for all combinations of arrangements, the water flooding in the gas flow channel is nearly 25%. However, the real flooding problem, which seriously damages the cell performance, occurs in the porous gas diffusion layers close to the three-phase boundary. Thus, the water accumulations in the gas flow channels can only be used as an indicator for potential water flooding in the gas diffusion layers.

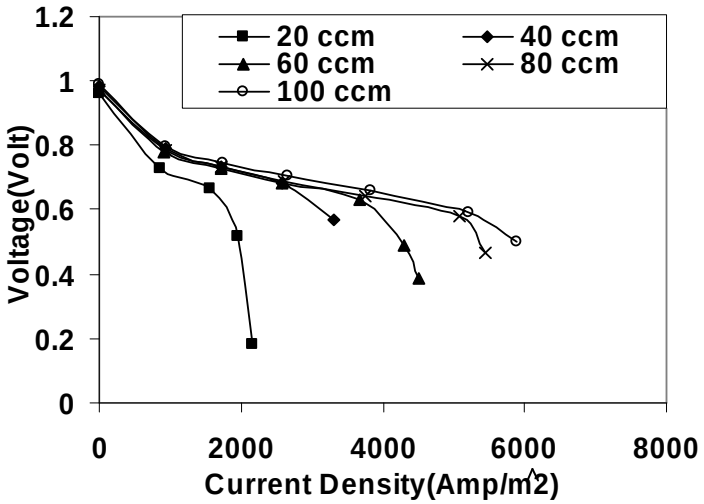

Figure 3.53: Voltage versus current density curve for Serpentine (Anode)-Serpentine (Cathode) gas flow channel configuration under different hydrogen flow rates at 21°C

This work uses cell voltage, current density, flooded area and fuel utilization to characterize the cell performance. However, another factor for the fuel cell design is the cell electric efficiency, which is not addressed here. In particular, energy is needed to blow the fuel and air through the channels, meaning more energy will be consumed. If the energy loss is considered this way, the optimal gas flow channel arrangements will have the same energy consumption and similar effects to those described above in both sides of the anode and the cathode channels.

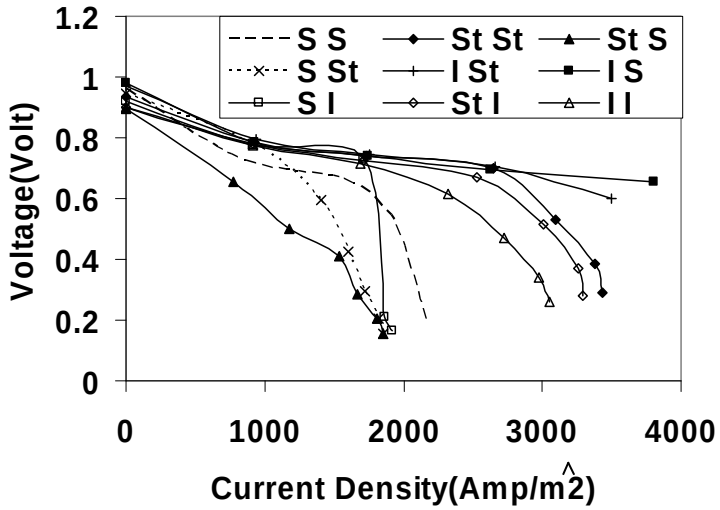

Figure 3.54: V-I curve at 20 sccm H_2 flow rate using different gas flow channel configurations. Here, S: Serpertine, St: Straight, I: Interdigitated.

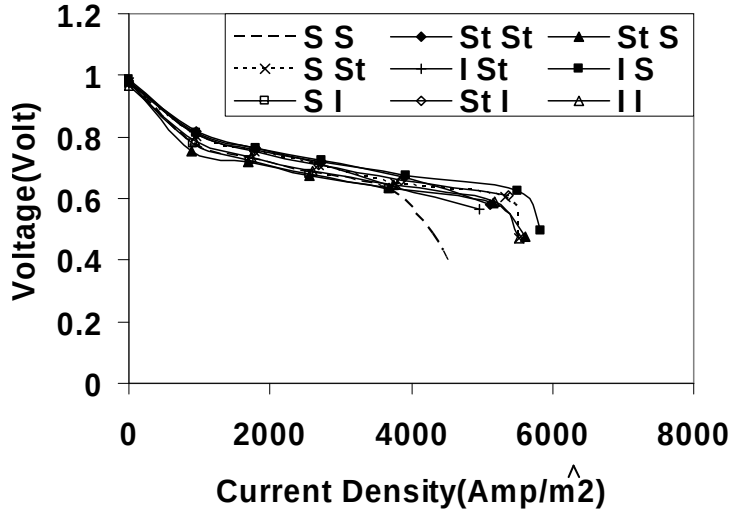

Figure 3.55: V-I curve under 60 sccm H_2 flow rate for different gas flow channel configurations. Here, S: Serpertine, St: Straight, I: Interdigitated.

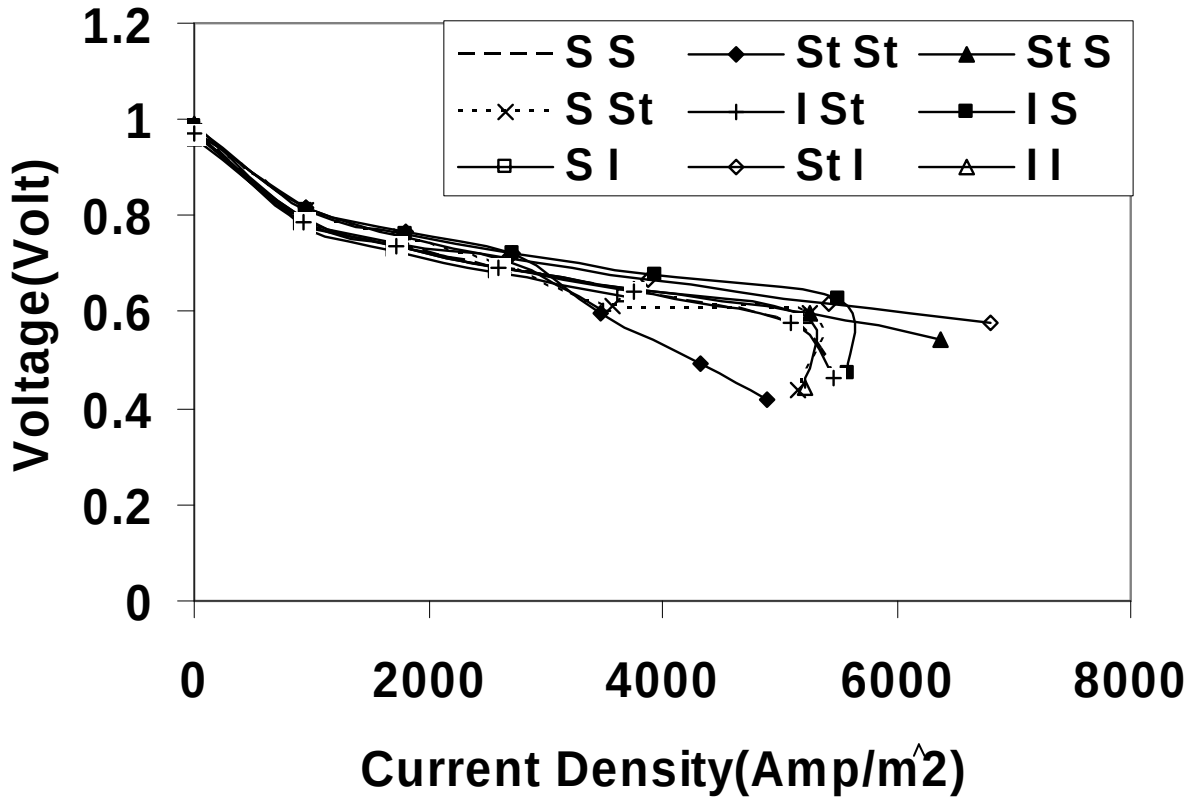

Figure 3.56: V-I curve under 80 sccm H_2 flow rate for different gas flow channel configurations. Here, S: Serpertine, St: Straight, I: Interdigitated.

Table 3.7: Velocity, Reynolds number, and total pressure loss data for various reactants and bipolar Plates

	Reactant fluid	Velocity (m/s)	Reynolds Number (Re)	Total pressure loss (kPa)
Serpentine	Oxygen	0.767	79.6	1.5567
Straight	Oxygen	0.02556	5.147	0.000202
Interdigitated	Oxygen	0.010223	2.0585	0.0019689
Serpentine	Hydrogen	0.333	20.2	0.32
Straight	Hydrogen	0.01111	1.3055	0.00004189
Interdigitated	Hydrogen	0.004444	0.522	0.00039823

Table 3.8: Water flooding in the cathode side gas flow channels for various gas flow channel configurations. Here, S: Serpertine, St: Straight, I: Interdigitated.

Gas flow channel arrangements	% Water in the channel
S I	26%
S St	22%
S S	23%
I I	37%
I St	27%
I S	25%
St I	17%
St St	25%
St S	34%

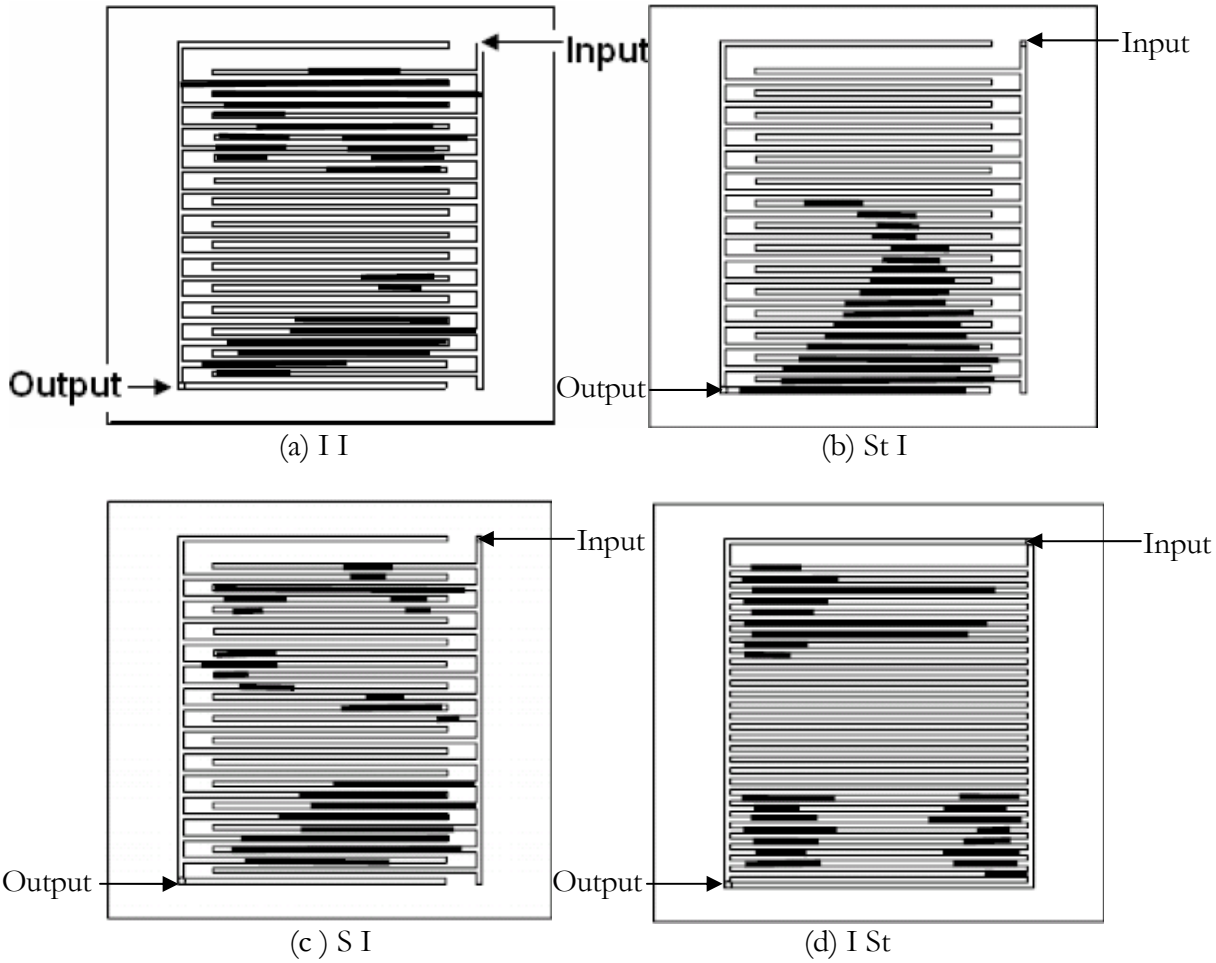

Figure 3.57: Water flooding patterns of cathode side bipolar plates. Here, S: Serpertine, St: Straight, I: Interdigitated.

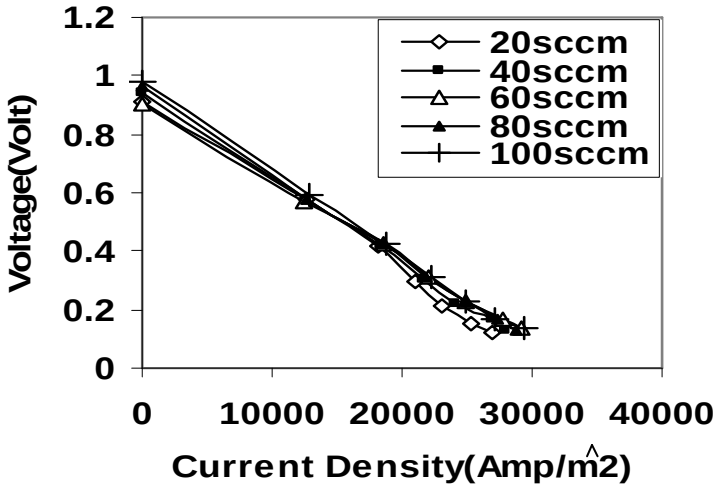

Figure 3.58: Experimental result for voltage vs. current density curve for various flow rates for the single channel test cell

3.3.1 Conclusion on Gas Flow Channel Configurations

An Interdigitated anode gas flow channel with a Serpentine cathode gas flow channel gave the best result. For this arrangement, the hydrogen is forced to flow inside the anode porous gas diffusion layer towards the reaction sites. The water flooding is partially eliminated by the using of serpentine bipolar plate in cathode side, due to the high flow speed and thus the capability of blowing the water droplets out of the cell. It is expected that, this arrangement of bipolar plates could significantly help the operation of PEMFC in practical applications.

3.4 PEMFC Poisoning and Recovery

Fuel cells are high efficiency electrochemical devices. Although considerable advances have been made in the past three decades, fuel cell systems are still considered to be emerging technology. Proton Exchange Membrane Fuel Cells (PEMFCs) are under aggressive research and development. PEMFCs are attractive power sources for use in many applications, including portable power sources, electric vehicles and on-site combined power or heat plants, due to the inherently high efficiency and low emission. Despite the advantages, significant obstacles to

commercialization remain in the areas of cost, durability, heat and water management and tolerance to poisons (especially carbon monoxide, CO) in the cell. CO poisons the PEMFC through preferentially adsorbing to the platinum surface and blocking the active sites on anode side of the catalyst layer.

At the heart of a PEMFC is the Membrane Electrode Assembly (MEA). A five layer MEA consists of a proton exchange membrane, two catalyst layers, and two gas diffusion layers. The catalyst layers are in direct contact with the membrane and the gas diffusion layers. Typical catalyst layer thickness is about 10 to 20 microns while the membrane thickness varies from 25 microns to 100 microns. To operate a PEMFC efficiently, it is crucial to keep the proton conducting membrane in the most hydrated state. Upon losing water, the conductivity of the membrane and the fuel cell performance will deteriorate. That is a reason why most of the commercially available membranes, such as Nafion^{TM}, have a maximum operating temperature of about 80ºC.

A thin-film type micro heating device is to be embedded in the electrolyte membrane of the PEMFC, close to the anode side surface. This micro heater is designed to heat up the PEMFC anode side catalyst layer locally in a pulsed manner, without causing overheating to the neighboring PEMFC membrane. Figure 3.59 shows the schematic design of such embedded micro heater which will be placed in the electrolyte layer, close to the anode side catalyst layer. This can be done by laying the thin film mesh heater onto one side of the electrolyte layer, then spin coating a thin layer of high temperature electrolyte solution. On top of the spin coated thin electrolyte layer, standard catalyst layer can be laid, such as Pt/Carbon catalyst inks. The electrolyte top layer should be thick enough to prevent electrical contact between the catalyst layer and the thin film heater. This design could significantly enhance the carbon monoxide tolerance level of PEMFC, due to the high temperature induced fast CO poisoning recovery process. Because in the major part of

the membrane temperature is kept low, high conductive low temperature membranes can be used. By applying a transient localized heating to the catalyst layer while maintaining the membrane at a near normal temperature (below 80ºC), the PEMFC is expected to be able to work continually using a high CO concentration fuel.

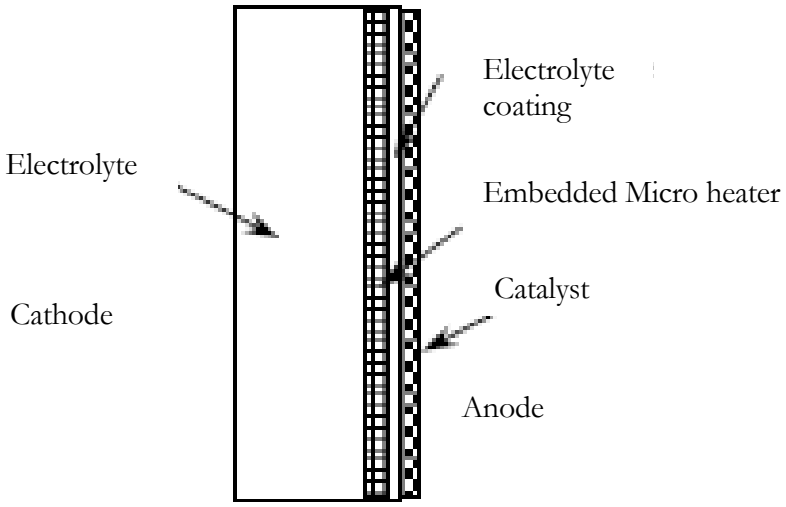

Figure 3.59: The design concept of the embedded heating device

In the study, a simplified approach was used. Instead of embedding a thin-film heater inside the thin electrolyte, fine mesh heater, 40 microns diameter stainless mesh, was constructed in direct contact with a five layer PEMFC Membrane Electrode Assembly (MEA) as shown in figure 3.60.

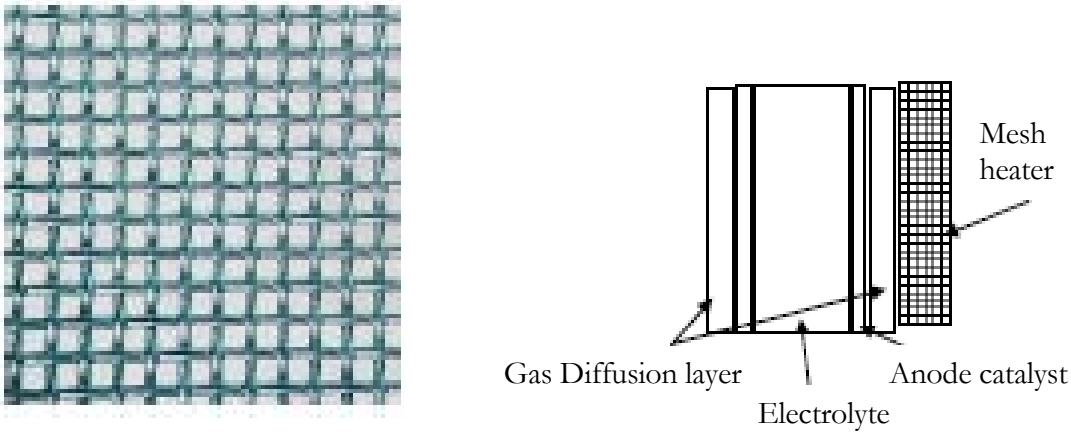

Figure 3.60: BOPP stainless Mesh and the schematic test setup

For the experimental tests, commercially available five layer Membrane-Electrode Assembly (MEA) was used. The MEA area is 5.05 cm by 4.95 cm. Hydrogen and oxygen flow over anode and cathode in a co-flow manner i.e. both flow are parallel and in the same direction. Laboratory temperature was air-conditioned at 21°C. The pressure of oxygen and hydrogen in the cell was close to ambient air pressure. Unused oxygen was released at the cathode side outlet port. No suction device was used for the oxygen outlet. However, outlet hydrogen port was connected via a long tube to a laboratory hood for rapid dispersion of unused hydrogen gas out of the lab.

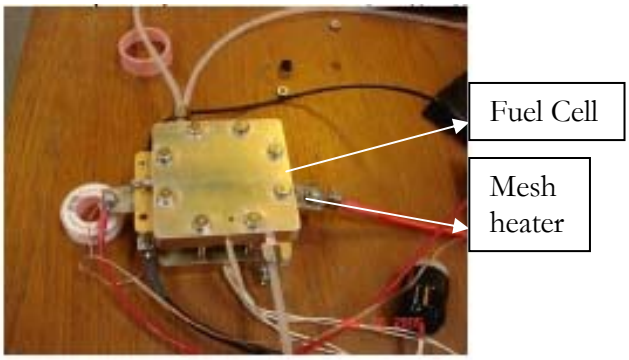

Figure 3.61: Fuel Cell with mesh heater in operating condition

The testing fuel cell has an outer dimension of 7.65 cm by 7.65 cm and a thickness of 1.3 cm, shown in figure 3.61. Serpentine and parallel bipolar plates were used. The gas flow channels have a width of 1 mm and a depth of 1 mm. The fuel cell was connected to variable load resistors to observe the variation of cell performance with loads. Twelve resistors: four 0.68 ohm, two 0.56 ohm, two 0.39 ohm and four 0.27 ohm, were used to form the loading bank. By connecting some or all of these resistors in serial or parallel, different loadings were achieved. Flow rate of hydrogen was varied in the tests to observe cell performance dependence. The fuel cell output voltage was monitored using a multi-meter. The cell current is obtained by taking the ratio of the measured voltage and the relevant resistance; the cell power is obtained by multiplying the current density and the voltage. The testing cell is instrumented with two cartridge heaters for maintaining an

elevated operating temperature. To avoid the overheating of the cell, thermocouple readings were taken from the testing cell when these heaters were used.

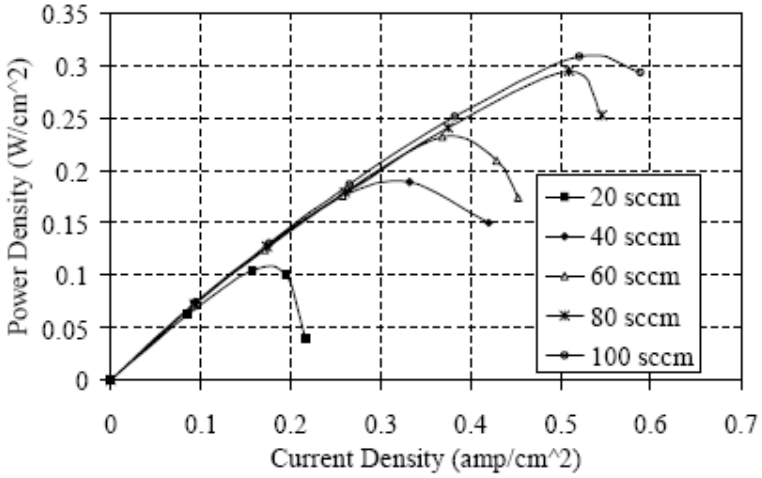

Figure 3.62: Power density versus current density curve using pure hydrogen

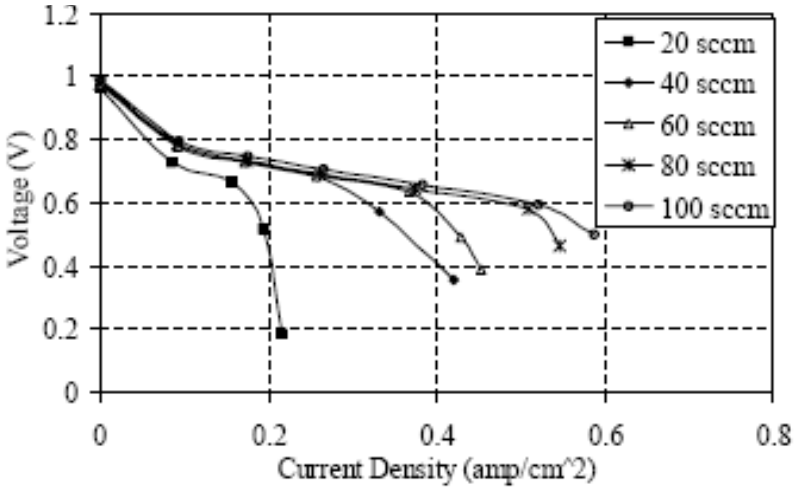

Figure 3.63: Voltage versus current density curve using pure hydrogen

Pure hydrogen was used to obtain the baseline results. Power density-Current density relations at an operating temperature of 21ºC using serpentine gas flow channel at anode side and serpentine gas flow channel at cathode side is shown in figure 3.62 for various flow rates of hydrogen. As the local current density is a function of hydrogen and oxygen partial pressure, increasing the fuel flow rate will increase the partial pressure at the downstream portion of fuel

gas flow channels and this ultimately could enhance the performance of the cell. The pure hydrogen case fuel cell voltage versus current test results can be found in figure 3.63.

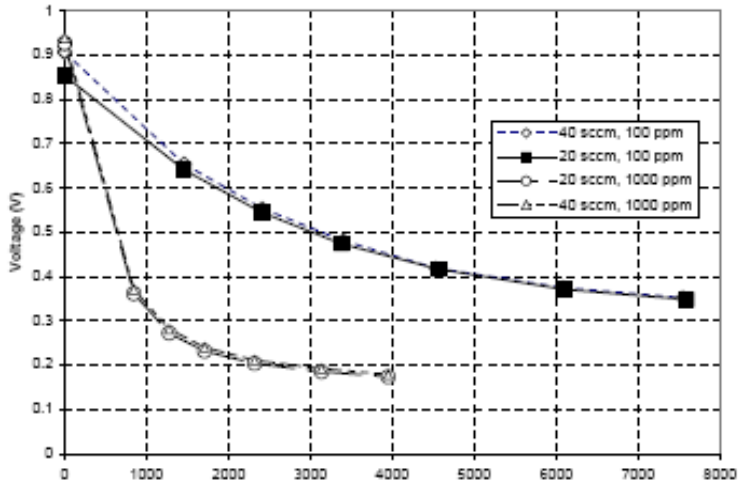

Figure 3.64: Performance of PEMFC using 100 ppm and 1000 ppm CO concentration H_2 under fuel flow rates of 20 sccm and 40 sccm

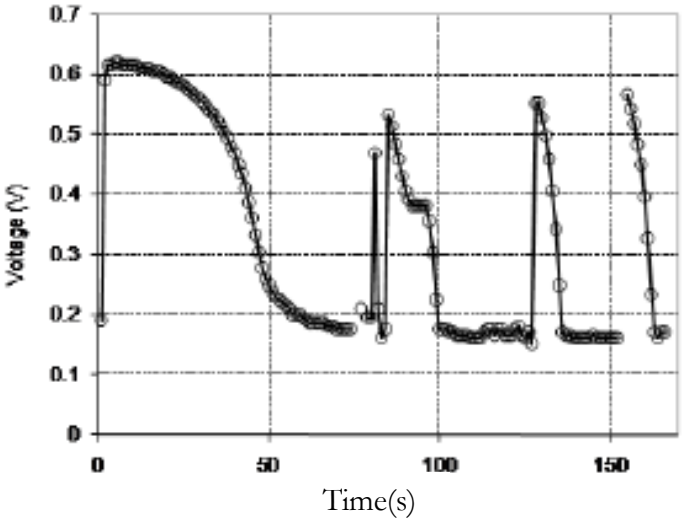

Figure 3.65: PEMFC poisoning and recovery due to pulsed heating (3 pulses at ~80s, 128s and 152s)

After the pure hydrogen tests, hydrogen fuels contaminated by CO were used. Carbon monoxide was premixed with hydrogen and the gas mixture was stored in a gas-sampling bag. Figure 3.64 shows the performance of the PEMFC using hydrogen fuel with a CO concentration of 100 ppm and 1000 ppm at different fuel flow rates.

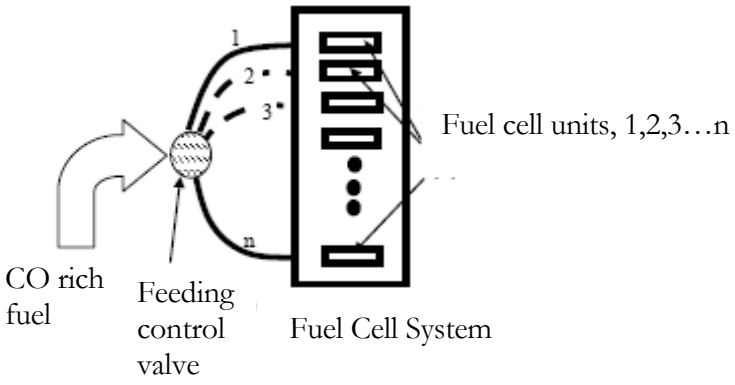

Figure 3.66: PEMFC poisoning and recovery due to pulsed feeding

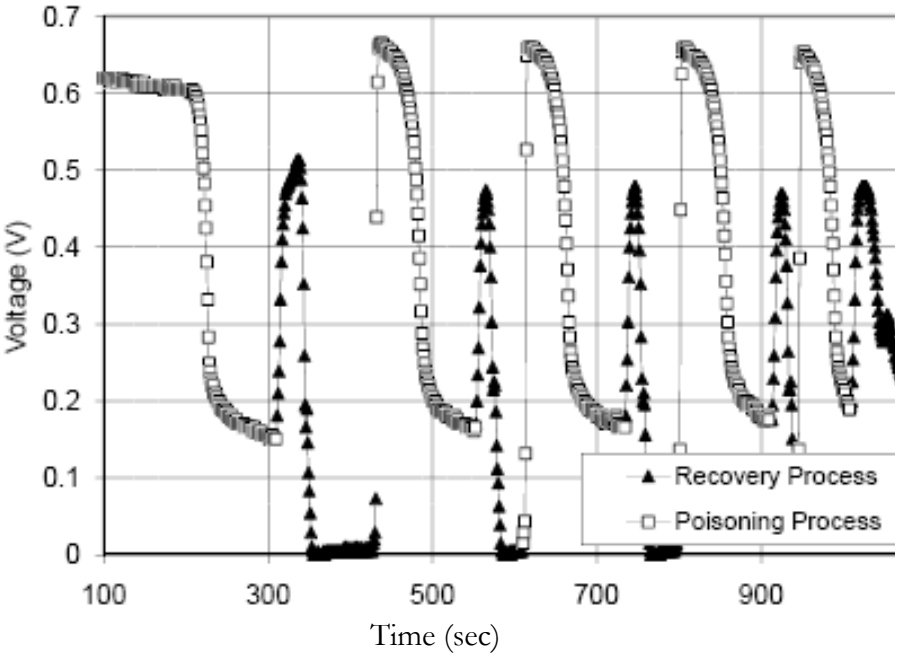

Figure 3.67: Poisoning and recovery of PEMFC due to pulsed feeding.

To quantify the change in performance of PEMFCs in the presence of relatively high concentrations of CO (1000 ppm) that exists in the hydrogen fuel stream, micro heating mesh, in direct contact with the MEA was heated up using a micro thermocouple spot welder at a power setting of 35J, in a pulsed manner as shown in figure 3.65. Before CO poisoning, the PEMFC could provide a constant voltage of 0.6V, under a loading of 1W. After introducing 1000 ppm CO concentration in hydrogen fuel and into the system, the cell voltage dropped to about 0.2V. The

cell can only produce 0.12W of power. With a heating pulse, the cell was quickly recovered to about 0.6V, and poisoned again in about 10 to 20 Seconds. Utilizing the transient recovery-poisoning process by using continuous pulsed heating, an average cell voltage of 0.4V is expected, which gives an average power output of 0.5W. This is four times better than the poisoned case.

The feeding line pressure swing method is also used to mitigate the CO poisoning. Using the fuel line pulsed feeding method, a PEMFC may operate between poisoning and fully recovery. This can be done by splitting a fuel cell system into a number of sub-units. A multi-channel valve can be used to shut the supply of fuel to certain portion of the system. At the outlet port of the fuel cell, air or oxygen is readily mixed with the waste fuel. Unlike the well know strategy of oxygen injection: supplying a small amount of oxygen at the fuel inlet, which causes the reduction of fuel cell efficiency, oxidant will be supplied from the outlet port to certain portions of the system. Without fuel supply while under load, the hydrogen in the PEMFC near the reaction sites will be consumed quickly and will produce a local "vacuum". Thus, the oxygen can be drawn into the fuel cell from the outlet port, which can recover the poisoned cell, as shown in figure 3.67. The pressure swing test results are shown in figure 3.67. It shows the feeding line pressure swing process could recover the CO poisoned PEMFC and improve the PEMFC performance by a factor of four when 1000 ppm CO concentration of H_2 was used.

3.4.1 Conclusion on PEMFC CO Poisoning and Recovery

This study studied the possibility of fuelling a PEMFC continuously by using a high CO concentration fuel , by applying a transient localized heating to the catalyst layer while maintaining the membrane at a normal temperature (below 80°C) and by using a pulsed feeding method (pressure swing) to promote the quick recovery of the fuel cell from the poisoned state. Because of the controlled membrane temperature, high conductive commercial membranes can be used. As most of

the cells operate at low temperature, quick start can be maintained. The study is specifically relevant to the fuel cell systems that may be operating with a reformer under dynamic load demands, thus resulting in transient high CO levels. The poisoning or recovery data presented in this study could be used to validate future theoretical model of poisoning and recovery behavior. It could also provide useful information to designers of fuel cell control schemes and reformate fuel-processing systems.

C H A P T E R - 4

FUEL CELL NUMERICAL ANALYSIS*

To compare experimental results as well as to predict fuel cell optimization it is necessary to simulate fuel cell. Numerical analysis has been conducted with the view to look at PEMFC single channel, transient temperature during pulse heating, thermal stress in SOFC fabrication, and liquid droplet dispersion at the interface of GDL-GFC.

4.1 PEMFC Single Channel

Multiphysics-based numerical simulation software using COMSOL was used to perform a parametrical optimization for the flow field design and to understand the experimental data. COMSOL offers detailed flow field, pressure field and concentration distribution along the gas flow channels. COMSOL is a commercial Partial Differential Equation (PDE) solver, which can solve coupled multi-physical problems which involve in electrochemistry as well as fluid simulation in Fuel cell.

The PDE (Partial differential equations) works as the governing equations for most physical phenomena and provide the foundation for modeling a wide range of scientific and engineering problems. There are three (3) ways of describing PDEs in COMSOL: the weak form, coefficient form, and general form. The coefficient form of PDE in COMSOL is suitable for the linear or nearly linear models and the rest two are suitable for the nonlinear models. The weak form was used in the simulation. The simulation software COMSOL runs finite element analysis (FEA) to solve the PDEs, together with adaptive meshing and error controls. To overcome the memory and speed limitation of simulation facing a three dimensional multiphysics calculation, source terms in the

*Portions of this chapter are used by Journal of Failure Analysis and Prevention and ASME Journal of Fuel Cell Science and Technology

simulation works were multiplied by a factor and this factor value was increased from 0.001 to 1.

For the simulated fuel cell model, problems with high reaction rates (high R_i), or more generally, large source terms in COMSOL, resulted in convergence problems and error message "NaN was repeatedly found in solution", or "Damping factor too small" were occurred. This problem was solved by using reduced source terms, and then gradually increasing it by using the previous solution during time of solving until the solution reached to the original problem. The reaction terms were handled by multiplication of the reaction (source) term (Ri) by a factor which is a variable,"k". The list of Parameter Values in the Solver Parameter were specified to be a range of increasing values, starting at a lower value and increasing to unity, for example "1e-3 1e-2 1e-1 1". The Solve button was started which helped to get the solution. COMSOL started to solve the problem using the first multiplication factor (0.001). Then, if that worked, the software COMSOL used the solution as initial guess for the next parameter value, and solved until it reached the last parameter value. As the specification of the last parameter value is to be unity, it leaded to the last solution corresponding to the original solution of the problem.

The simulated geometry was very thin in width and height directions comparing to its length. Since the simulation software COMSOL mesh generator creates tetrahedral that are isotropic in size, a large number of elements may be created in the thin layer. In addition, large differences in scale may cause the mesh generator to fail in creating the mesh. Therefore, the width and the height of the simulated cell are scaled during the meshing process to reduce the number of elements created before meshing. Then the mesh is scaled back, so that it fits the original geometry. The mesh is scaled by a factor of five without losing too much accuracy because a scale factor of 3 to 5 or 5 to 10 in one direction can sometimes be acceptable.

The region of interest of simulation domains were the three (3) dimensional as well as

Electrolyte and Electrodes on both sides of this electrolyte. The simulation includes the multi species transportation in the porous electrodes and the coupled electrical current and potential distributions. Stefan-Maxwell diffusion equations were applied to a mixture of O_2 and H_2O in the cathode side. As the anode side, the gas is not a two or more gas mixture (only hydrogen) so Stefan-Maxwell diffusion equations were not applied in the gas diffusion layer. Only Darcy's porous gas law was applied in anode side gas diffusion layer. At the same time for the flow goes through the porous electrodes, the Darcy's law was employed. In the electrolyte membrane, the ionic balance was calculated.

In porous region of the anode and the cathode, the global transport of momentum by shear stresses in the fluid is negligible as the pore walls impede momentum transporting the fluid outside the individual pores. Since a detailed description down to the resolution of every pore is not practical in the simulated model, homogenization of the porous and fluid media into one single medium was a common approach. Darcy's Law is used in that domain as it is based upon this approach and describes flow in porous media where pressure gradient is the only driving force.

Darcy's Law in the gas domain states that the pressure gradient, the fluid viscosity and the structure of the porous media determine that velocity vector.

$$\vec{u} = -\frac{\kappa}{\mu}\nabla p \qquad \text{Eq. (4.1)}$$

where, $\vec{u}$ =velocity vector

κ =permeability

μ =viscosity

∇p = pressure gradient

The Darcy's law application mode in the Chemical Engineering module of COMSOL combines Darcy's Law with the continuity equation. As a result, the equation becomes:

$$\frac{\partial \rho}{\partial t} + \nabla \bullet \rho\left(-\frac{\kappa}{\mu}\nabla p\right) = 0 \qquad \text{Eq. (4.2)}$$

where, ρ is the density of fluid

Gas density in the simulated model depended on the pressure which, for an ideal gas, was described by the ideal gas law:

$$\rho = \frac{PM}{RT} \qquad \text{Eq. (4.3)}$$

where, M=molar weight of the gas, R is Universal gas constant and T is temperature.

For the simulated model, impervious or symmetric boundary condition is defined as:

$$-\frac{\kappa}{\mu}\nabla p \bullet \vec{n} = 0 \qquad \text{Eq. (4.4)}$$

Impervious or symmetric boundary condition actually resides in the surface between the electrolyte and electrode surface. For the mixture of oxygen (O_2) and water (H_2O) in the cathode electrode Maxwell-Stefan diffusion and convection module was used. The reason to use Maxwell-Stefan diffusion in that Fick's law of diffusion is based upon the assumption that species dissolved in a solution interact with the solvent only independent of concentration. In the concentrated solutions, the solvent is affected by the solute species, and during the time of mixing, they interact with each other. Their diffusion coefficients are concentration dependent. The Maxwell-Stefan Diffusion and convection application mode makes it possible to treat convection and diffusion problems where there is full interaction between the species dissolved in a solution. In these solutions, the diffusion coefficients corresponding to the Fickian diffusion coefficients are highly dependent on the chemical composition of the solution [Curtiss and Bird (1999)].

$$\frac{\partial \rho\omega_i}{\partial t} + \nabla \bullet \left[-\rho\omega_i \Sigma_{j=1}^{N} D_{ij}\left\{\frac{M}{M_j}\left(\nabla\omega_j + \omega_j\frac{\nabla M}{M}\right) + \left(x_j - \omega_j\right)\frac{\nabla p}{p}\right\} + \omega_i\rho\vec{u} + D_i^T\frac{\nabla T}{T}\right] = R_i \qquad \text{Eq. (4.5)}$$

where, M denotes Molar mass of the mixture, M_j is the molar mass of species j, x_j is the mole fraction of component j, ω_j is the mass fraction of component j, R_i is the reaction rate of species i, D^T is the thermal diffusivity, D_{ij} is the binary diffusivities.

Mass fractions are related to:

$$\sum_i \omega_i = 1 \qquad \text{Eq. (4.6)}$$

In addition, molar mass fraction is related to:

$$x_i = \frac{\omega_i}{M_i \sum_k \frac{\omega_k}{M_k}} \qquad \text{Eq. (4.7)}$$

In the simulated model this module is used for the electrodes and electrolyte because its relation with these conductive media. In general, electrolysis involves a medium with conductivity and a steady current. When handling the conductive media, the equation of continuity works well. In a stationary coordinate system, the point form of Ohm's law states that:

$$\vec{J} = \sigma\vec{E} + \vec{J}^e \qquad \text{Eq. (4.8)}$$

Where, $\vec{J}$ is current density, σ is conductivity, $\vec{E}$ is electric field intensity and $\vec{J}^e$ is externally generated current density. The static form of the equation of continuity then gives:

$$\nabla \bullet \vec{J} = -\nabla \bullet \left(\sigma \nabla V - \vec{J}^e\right) = 0 \qquad \text{Eq. (4.9)}$$

To handle current sources, the equation is generalized to:

$$-\nabla \bullet \left(\sigma \nabla V - \vec{J}^e\right) = \vec{Q}_j \qquad \text{Eq. (4.10)}$$

where, $\vec{Q}_j$ is the current source.

This generalized equation was used in the electrodes and electrolyte. In this simulated model, multiphysics modeling of a proton exchange membrane fuel cell (PEMFC) was applied. This model

uses current balances, mass balance (Maxwell-Stefan diffusion for reactant and water) and momentum balances (gas flow) to simulate the PEMFC behavior.

The model of the fuel cell consists of three (3) domains: an anode, a proton exchange membrane, and a cathode. Each of the porous electrodes has an inlet channel, a current collector, and an outlet. In this simulation, an agglomerate model will describe the electrode reactions in the active catalyst layers. The agglomerate model consists of catalyst and carbon particles embedded in polymer electrolyte. The equations for the agglomerate models originate from the analytical solution of a diffusion-reaction problem in a spherical porous particle [Fogler (1999), and Bird, Stewart, and Lightfoot (1960)]. At the anodic active catalyst layer, hydrogen is the diffusing and reacting species in the agglomerates, while oxygen is the diffusion and reacting species in the agglomerates at the cathode. An agglomerate model of the cathodic active catalyst layer of a PEMFC has been presented by Broka (1995).

The potential distribution is modeled by using the application mode conductive media DC in the three subdomains, and it is given by the following equations:

$$\nabla \bullet \left(-\kappa^{s,eff} \nabla \phi_s\right) = 0 \quad \text{in anode subdomain} \qquad \text{Eq. (4.11)}$$

$$\nabla \bullet \left(-\kappa^{m,eff} \nabla \phi_m\right) = 0 \quad \text{in membrane subdomain} \qquad \text{Eq. (4.12)}$$

$$\nabla \bullet \left(-\kappa^{s,eff} \nabla \phi_s\right) = 0 \quad \text{in cathode subdomain} \qquad \text{Eq. (4.13)}$$

where, κ^{eff} is the effective conductivity. The potentials in the electrode are denoted by ϕ_s while in the membrane it is denoted as ϕ_m.

The gas flows in the gas backings are modeled by using the Darcy's law application mode. The velocity of the gas is given by the continuity equation, according to:

$$\nabla \bullet \left(c^g \vec{u}\right) = 0 \quad \text{in anode and cathode subdomain} \qquad \text{Eq. (4.14)}$$

Here, c^g is total molar concentration of the gas phase and $\vec{u}$ denotes velocity of the gas.

Darcy's law for porous media states that the gradient of pressure, the viscosity of the fluid, and the structure of the porous media determines the velocity vector:

$$\vec{u} = -\frac{\kappa_p}{\mu}\nabla p \qquad \text{Eq. (4.15)}$$

Here, κ_p denotes the permeability of the electrode, μ viscosity of the gas and p is pressure.

The ideal gas law gives the total molar concentration of the gas phase:

$$c^g = \frac{p}{RT} \qquad \text{Eq. (4.16)}$$

where, R denotes gas constant and T is the temperature.

The model takes into account two species at the cathode (oxygen O_2 and water H_2O). Maxwell-Stefan diffusion and convection application mode is used for cathode side electrode in the model.

At the electrode-membrane interface, the gas velocity boundary condition in the Darcy's law application mode is calculated from the total mass flux. It is done according to:

$$\vec{u} = \frac{n_{total}}{\rho} \qquad \text{Eq. (4.17)}$$

where, n_{total} is given by the local current density and molar masses of the reacting species.

The boundary condition for the current density at the interface between the anode and the membrane, normal to the anode domain, can be written as:

$$\left(-\kappa^{s,eff}\nabla\phi_s\right)\bullet\vec{n} = i_a \qquad \text{Eq. (4.18)}$$

This term act as a source term for that region where,

$$i_a = -K_1(c_H^{agg} - c_H^{ref}\exp(-K_2(\phi_s - \phi_m - \Delta\phi_{eq,a})))(1 - K_3\coth K_3) \qquad \text{Eq. (4.19)}$$

In addition:

$$K_1 = \frac{6\delta_l (1-\varepsilon) F D_H^{agg}}{(R^{agg})^2} \quad \text{Eq. (4.20)}$$

$$K_2 = \frac{2F}{RT} \quad \text{Eq. (4.21)}$$

$$K_3 = \sqrt{\frac{i_{o,a} S}{2F c_H^{ref} D_H^{agg}}} R^{agg} \quad \text{Eq. (4.22)}$$

In these expressions, c^{agg} denotes dissolved gas concentration at the surface of the agglomerates, c^{ref} denotes dissolved gas concentration at a reference state, and $\Delta\phi_{eq}$ is the potential difference between the electrode and the membrane at equilibrium conditions. Active layer thickness of the electrode is denoted by δ_l, while dry porosity of the electrode is denoted by ε. F denotes as Farady's constant, D^{agg} diffusion coefficient of the dissolved gas inside the agglomerate, R^{agg} the agglomerate radius, i_o the exchange current density and S the specific surface area of the electrode.

For the interface between the membrane and the cathode, the corresponding boundary condition normal to the cathode domain, becomes:

$$(-\kappa^{s,eff} \nabla \phi_s) \bullet \vec{n} = i_c \quad \text{Eq. (4.23)}$$

This term also act as source term for this region.

Where,

$$i_c = K_4 c_o^{agg} (1 - \sqrt{K_5 \exp(-K_6(\phi_s - \phi_m - \phi_{eq}^c))}) \coth \sqrt{K_5 \exp(-K_6(\phi_s - \phi_m - \phi_{eq}^c))} \quad \text{Eq. (4.24)}$$

And,
$$K_4 = \frac{12\delta_l (1-\varepsilon) F D_o^{agg}}{(R^{agg})^2} \quad \text{Eq. (4.25)}$$

$$K_5 = \frac{i_{o,c} S (R^{agg})^2}{4F c_o^{ref} D_o^{agg}} \quad \text{Eq. (4.26)}$$

$$K_6 = \frac{0.5F}{RT}$$ Eq. (4.27)

The dissolved hydrogen and oxygen concentrations at the surface of the agglomerates are related to the molar fraction of the respective species in the gas phase through Henry's law:

$$c_H^{agg} = \frac{p_H y_H}{H_H}$$ Eq. (4.28)

$$c_o^{agg} = \frac{p_o y_o}{H_o}$$ Eq. (4.29)

Here, H is the Henry's constant

It was chosen that the anode and cathode reference states to be equal to the molar fraction at the inlet channels of the anode and cathode respectively, at 1 atm. The dissolved gas concentration at the reference state is related to the molar fraction by the above-described Henry's law.

The current densities at the interfaces between the electrodes and the membrane and normal to the membrane domain, are given by:

$(-\kappa^{m,eff}\nabla\phi_m)\bullet\vec{n} = -i_a$ at the interface of anode and membrane subdomain Eq. (4.30)

$(-\kappa^{m,eff}\nabla\phi_m)\bullet\vec{n} = -i_c$ at the interface of cathode and membrane subdomain Eq. (4.31)

These two terms also act as source terms for those specified regions.

Clearly, what goes out from the anode goes into the membrane while the opposite is valid for the cathode.

The potential difference (volt) between the cathode and the anode current collectors corresponds to the total cell voltage. The potential (volt) at the anode current collector is arbitrarily chosen to be zero, while the total cell voltage (volt) is used as boundary condition at the cathode current collector. For the rest of the boundaries either insulation or symmetrical conditions have been considered:

$\phi_s = 0$ at the outer boundary of anode Eq. (4.32)

$\phi_s = V_{cell}$ at the outer boundary of cathode Eq. (4.33)

The pressure at the gas inlets and outlets are set to:

$p = p_{a,in}$ at anode side inlet Eq. (4.34)

$p = p_{ref}$ at anode side outlet Eq. (4.35)

$p = p_{c,in}$ at cathode side inlet Eq. (4.36)

$p = p_{ref}$ at cathode side outlet Eq. (4.37)

Hydrogen is consumed in the active catalyst layer at the anode while oxygen is consumed at the cathodic active layer. The mass transfer of species across the anodic and cathodic active layers is related to the local current density according to:

$$-\vec{n} \bullet \vec{n}_{H2} = -\frac{i_a}{2F}$$ at anode subdomain Eq. (4.38)

$$-\vec{n} \bullet \vec{n}_{O2} = \frac{i_c}{4F}$$ at cathode subdomain Eq. (4.39)

These two terms also act as source terms in that region. At the remaining boundaries, either insulation or symmetry conditions were used.

A computational method the finite element method (FEM) subdivides an object into very small finite-size elements. COMSOL generally uses the finite elements in the mathematical sense. In mathematical sense the finite element is a mesh element together with a set of shape functions and corresponding degrees of freedom. The linear combinations of the shape functions form a space of functions called the finite element space. In the traditional FEA sense, the concept of a finite element also includes the discretized form of the PDEs that govern the physics. A computer-based analysis method for field problems using the finite element method is known as finite element analysis

(FEA).

The degrees of freedom (DOFs) in FEA is the physics of one element which can be approximately described by a finite number. Each element is assigned as a set of characteristic equations (describing physical properties, boundary conditions, and imposed forces), which are then solved as a set of simultaneous equations to predict the object's behavior.

In this, numerical simulated work Non-linear solver was used which follows Newton step in the solution of a nonlinear PDE problem. Each nonlinear iteration involves the solution of a linear system of equations. The nonlinear solver uses an affine invariant form of the damped Newton method as described in Deuflhard (1974).

In general, COMSOL internally needs an accurate Jacobian matrix to establish convergence of a solution for nonlinear models. The model that described with weak form modes produces an exact Jacobian whereas the other modes generally do not. By considering the solution form as a weak for a model, COMSOL automatically generates the weak form of the equation, but the original application mode is still available. A partial differential equation (PDE) in the weak form is a more general formulation than the strong form. It is produced by multiplying the strong form PDE with an arbitrary function called the test function and integrating over the computational domain.

The basic calculation model has an electrolyte in the middle and two gas diffusion layers on the both side of the electrolyte. The most important part for a fuel cell is catalyst layer for this fuel cell that is residing on the surface of the electrolyte. Therefore, more meshing was used around the electrolyte and electrode interfaces. Extremely fine elements were used for meshing the model. Figure 4.1 shows the meshing of the model.

The Parametric nonlinear solver was used in COMSOL software to solve all the PDE equations. Parameter Nonlinear solver is similar to Nonlinear Solver in this software; the only extra

feature is iteration and it is done with varying one variable. The source terms in every boundary were increased systematically from a very smaller value to the value of one. The convergence of this model is hindered by source terms. Therefore, this systematically increase of source terms could accelerate the convergence of the calculation.

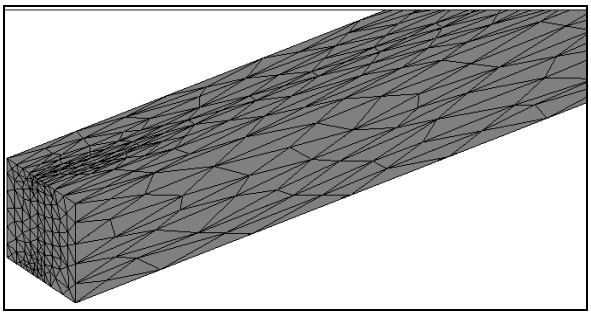

Figure 4.1: Meshing of the single channel model

Similar to the experimental work, flow rates of hydrogen was varied 20, 40, 60, 80, 100 sccm in the simulation works. However, the oxygen flow rate was maintained constant at 46 sccm for all of these simulation models. In these figures it is found that mass fraction of water patterns and partial pressure of hydrogen vary with variation of hydrogen flow rates. However, for oxygen flow rate is fixed in these works. Numerical simulation results of water patterns are shown in the following figures.

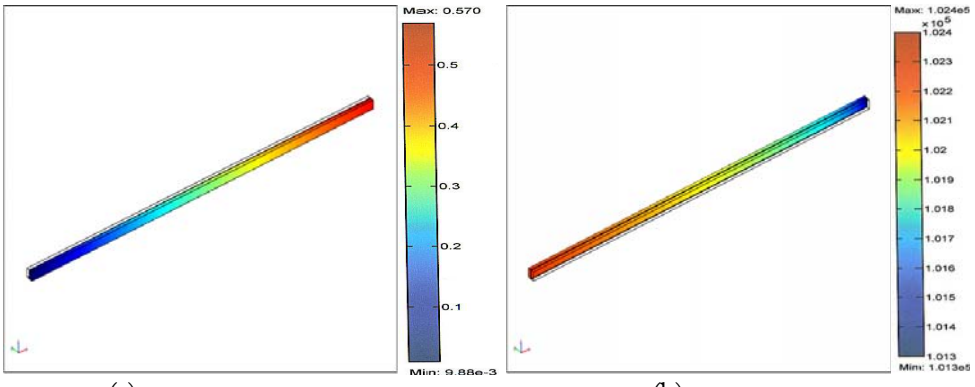

(a) (b)

Figure 4.2: 3D simulation, (a) water pattern indicated by water mass fraction, (b) hydrogen partial pressure, P_{H2}(bar) at 0.5V

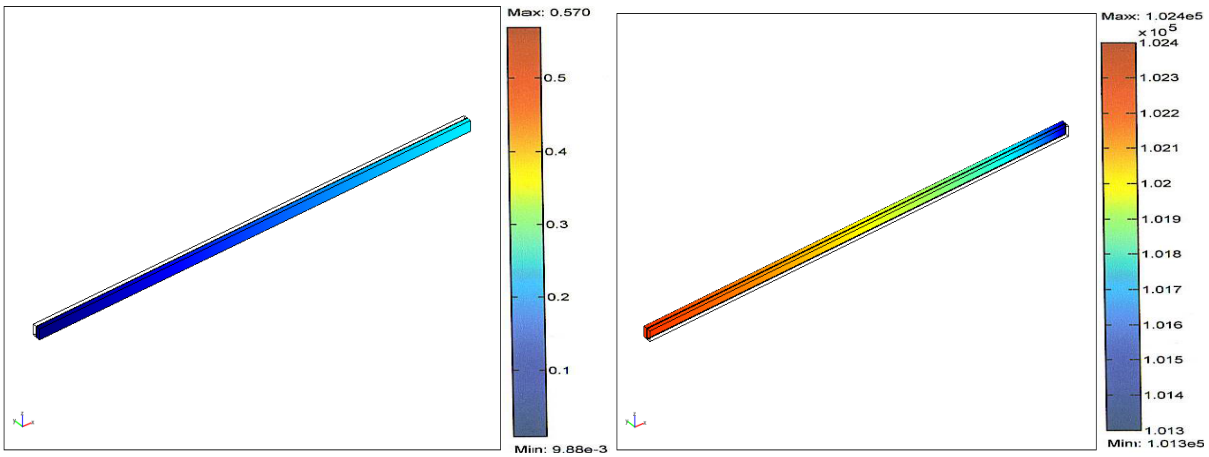

(a) (b)

Figure 4.3: 3D simulation, (a) water pattern indicated by water mass fraction, (b) hydrogen Partial pressure, P_{H2}(bar), at 0.7V

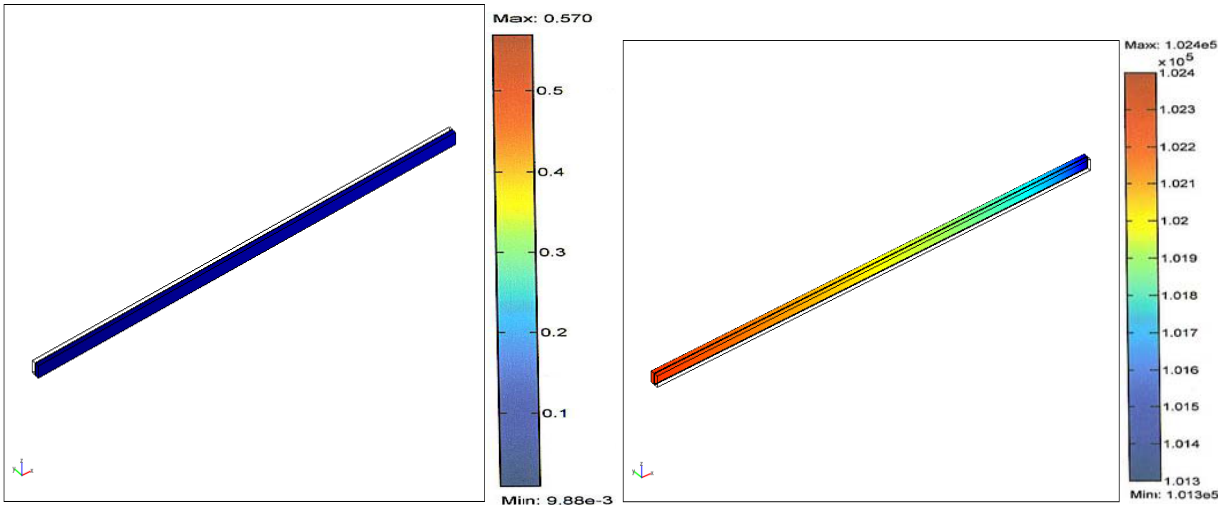

(a) (b)

Figure 4.4: Simulation of (a) water pattern indicated by water mass fraction (b) hydrogen partial pressure, P_{H2}(bar) at 0.9V

Numerical simulations are shown for various flow rates and loads. In the scale red color indicates higher and blue color indicates lower value. Each of the flow rate simulations shows reasonable results. For low load, less water is formed and for high load, more water is formed. Moreover, as the flow direction of hydrogen and oxygen are from left to right so, simulation results are also showing formation of more water in the outlet side of oxygen flow than the entrance. The

partial pressure of hydrogen is also varying reasonably from high to low from the entrance to the exit of the channel. In addition, for lower loads, less fuel is utilized and for higher loads, fuel utilization is high.

In Figure 4.5 shows water mass fraction variation along the single channel for 40 sccm hydrogen flow rate for various voltage readings. This figure shows reasonable indications of formation of liquid water particles from the entrance to the exit of the channel. Water content is less in the entrance and more in the exit for the same reason discussed earlier.

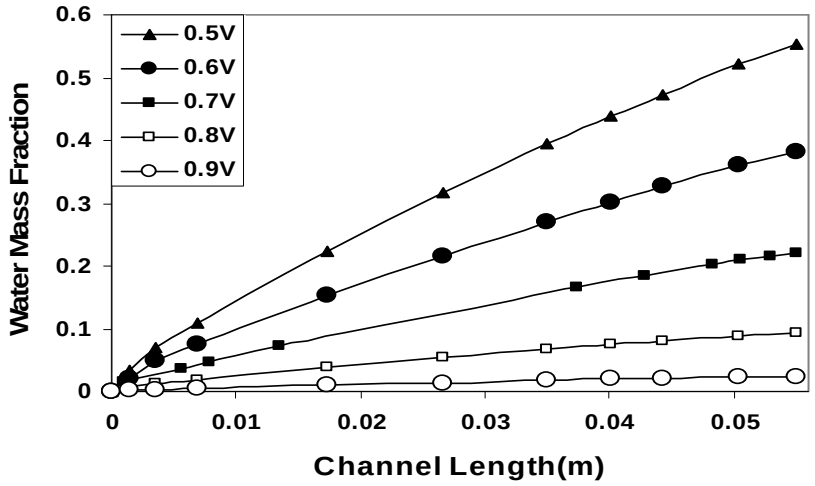

Figure 4.5: Water mass fraction along the channel

At nearly 20^0C, saturated vapor pressure is 2.338 kPa. After a certain distance from the inlet or entrance of the gas flow channel, water vapor will form or turn to liquid droplet because, the partial pressure of water will be greater than the saturation pressure of water vapor. The locations of that region from the entrance of the gas flow channel for various loads shows reasonable data such as, with the increase of loads, the unsaturated region will get smaller due to rapid electrochemical reaction from the entrance. After that distance, the partial pressure of water is greater than the saturated pressure of water vapor. Therefore, some of the water vapor start turning into liquid. From the entrance of cathode side to that particular region, the water vapor pressure is lower than

saturation vapor pressure. Therefore, in that region, water will be in vapor form.

In addition to that, two-dimensional (2D) numerical simulation has also been conducted. In this two-dimensional (2D) model is done without considering thickness of the channel as it is considered in three-dimensional (3D) model. In the 3D model, length, width, and thickness of the single channel are considered but for 2D simulation length and width of the channel are considered. In Figure 4.6 shows a 2D model with meshing. Three (3) layers are made for this 2D model. The middle layer is considered as the electrolyte and gas diffusion layers surrounding the both sides of this electrolyte. The catalyst is residing at the junction of gas diffusion layer and electrolyte. More meshing is used in both the sides of electrolyte, because of its importance in current generation.

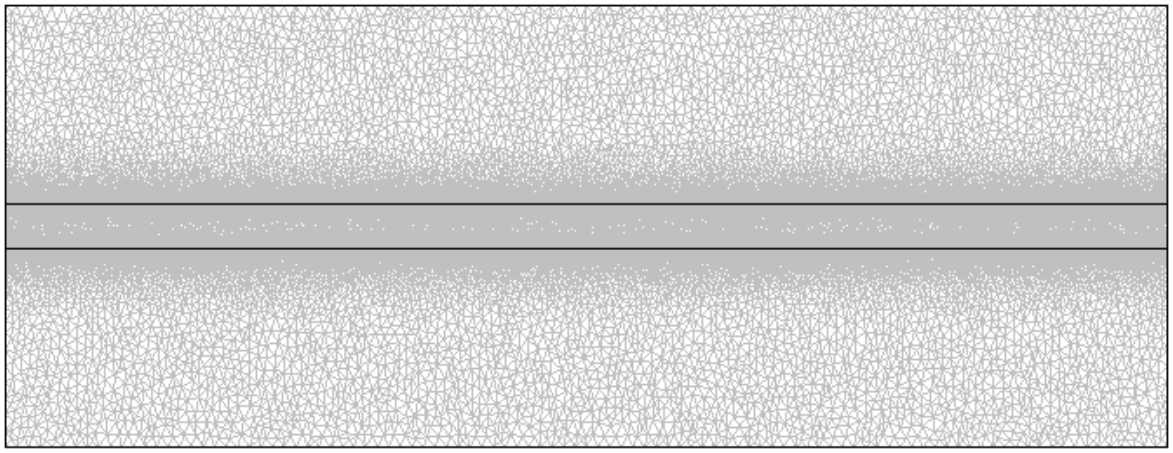

Figure 4.6: Grid of 2D model

It is found that, the simulations for two-dimensional (2D) models show the same shape of water patterns like 3D model. In the simulation results, it is found that with increasing loads, generation of water increases and with decreasing load water decreases. Figure 4.7 shows 2D numerical simulation of water pattern for 20 sccm hydrogen flow rate at a cell voltage of 0.7 volt with contour lines showing variation of water generation region. In addition to that, in the two dimensional (2D) simulation results the partial pressure of hydrogen decreases along the anode gas

diffusion layer.

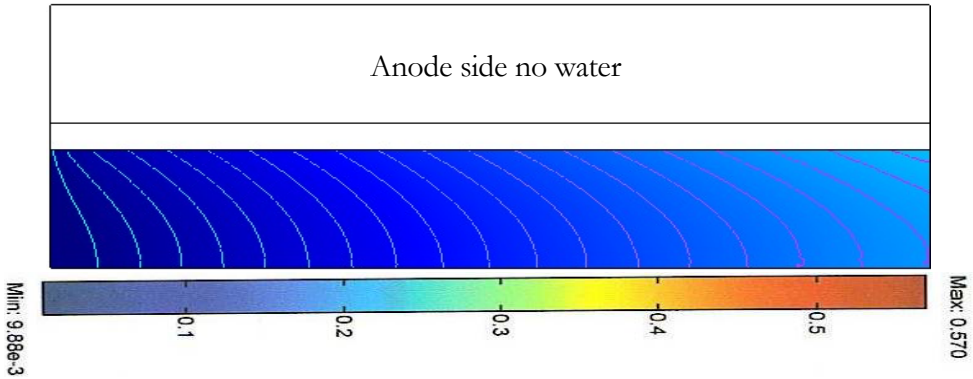

Figure 4.7: 2D numerical simulation of water pattern for 20sccm hydrogen flow rate at 0.7V with contour lines

After conducting two-dimensional (2D) numerical simulations, results are compared with three-dimensional (3D) numerical simulations. Two-dimensional (2D) and three-dimensional (3D) simulation results are compared and shown in figure 4.8. It is found that difference is very little between these two sets of data. For 2D simulation, reactants passing along the channel are considered but as thickness is not considered, so electrochemical reaction across the channel is not considered in those 2D simulation. In 3D numerical simulations as reactants are getting more space to react with the surface due to the thickness which resulted in more efficiency of the cell.

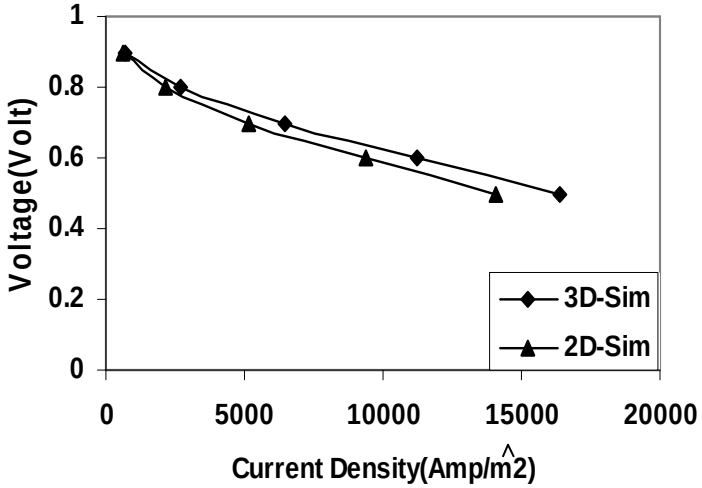

Figure 4.8: Voltage vs. current density curve for 2D and 3D simulation result for a 20sccm hydrogen flow rates.

Simulation of single channel fuel cell for various flow rates of hydrogen is shown in figure 4.9. The simulation result shows that in 20 and 40 sccm hydrogen flow rates are similar trend in the curve and match well. The reason for this trend is that those flow rates are more than enough for a single channel fuel cell. Simulation results are also shown for 1 sccm. For this less gas flow rate, a lower performance curve was found.

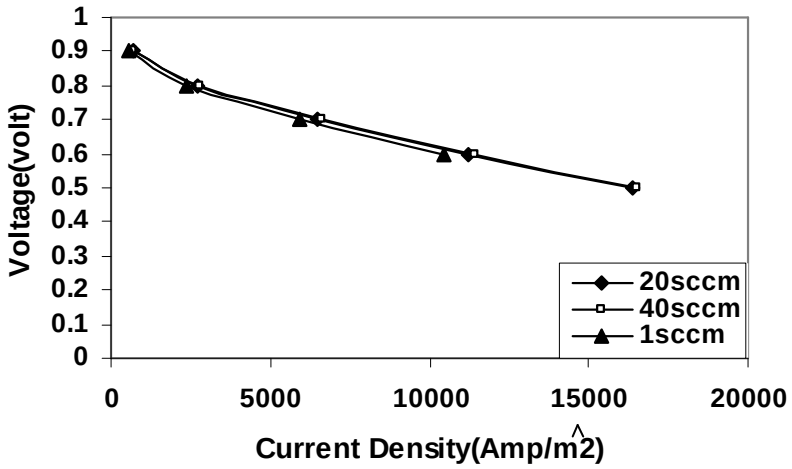

Figure 4.9: Simulation of voltage vs. current density curve for various hydrogen flow rates

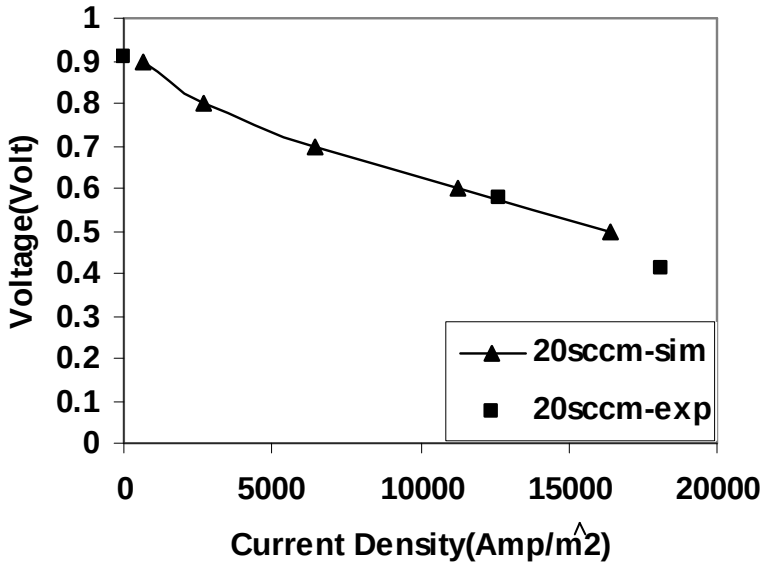

Figure 4.10: Comparison of experimental and simulation result of voltage vs. current density data for 20 sccm Hydrogen flow rate for one channel

In the Figure 4.10 the comparison of experimental and simulation results for single channel

fuel cell have been found. These results show agreement between the experimental and simulation results. There is very little variation between these two types of data. The very little deviation of the experimental data is due to the uncertainty of the factors involved in getting the data. Factors that might be involved are gas leakage from parts of fuel cells as well as tube to supply gases. Also experimental data might involve with some unsteady data as steady data were considered all along.

4.1.1 Conclusion on PEMFC Single Channel

The operation and performance of PEMFC is studied in a simplified way by a single channel fuel cell using numerical simulation software COMSOL. The fuel cell performance is analyzed in terms of polarization curve, power density curve, water pattern by mass fraction, water partial pressure in the gas flow channel, fuel utilization rate under different reacting fluid flow rates. Two-dimensional (2D) and three-dimensional (3D) simulations were performed in this study. During the 2D simulation, it is considered that this simulation is mainly used to obtain the detailed flow feature in the regions close to the electrolyte layer. The difference between 2D and 3D for the single channel design is found to be small. The simulation results were compared with the experimental measurements of a single channel PEMFC. The simulations results made agreement with the experimental data. It is expected that the methodology of single channel PEMFC simulation provides a useful design tool for the future development of PEMFCs.

4.2 Transient Temperature during Pulse Heating in Fuel Cell Poisoning Analysis

To demonstrate the design concept of fuel cell relating to transient temperature during pulse heating, a numerical simulation was performed using COMSOL software. COMSOL is a commercial Partial Differential Equation (PDE) solver, which can solve coupled multi-physical problems. The partial differential equations are the governing equations for most of the physical

phenomena and provide the foundation for modeling a wide range of scientific and engineering problems. There are three ways of describing PDEs in COMSOL: coefficient form, general form and the weak form. The coefficient form is suitable for linear or nearly linear models and it is used here. COMSOL runs finite element analysis to solve the PDEs, together with adaptive meshing and error controls. The 3D transient heat conduction was solved for the pulsed heating. In the simulation, a forty (40) microns diameter mesh heater was applied in direct contact with the catalyst layer (25 microns) of the PEMFC. The total thickness of the electrolyte layer is 100 microns. The general equation for an energy balance, which considers heat transfer through convection and conduction, used in the simulation is:

$$\rho \times C_p \times \frac{\partial T}{\partial t} + \nabla \cdot (-\kappa \times \nabla T + \rho \times C_p \times T \times u) = Q \quad \text{Eq. (4.40)}$$

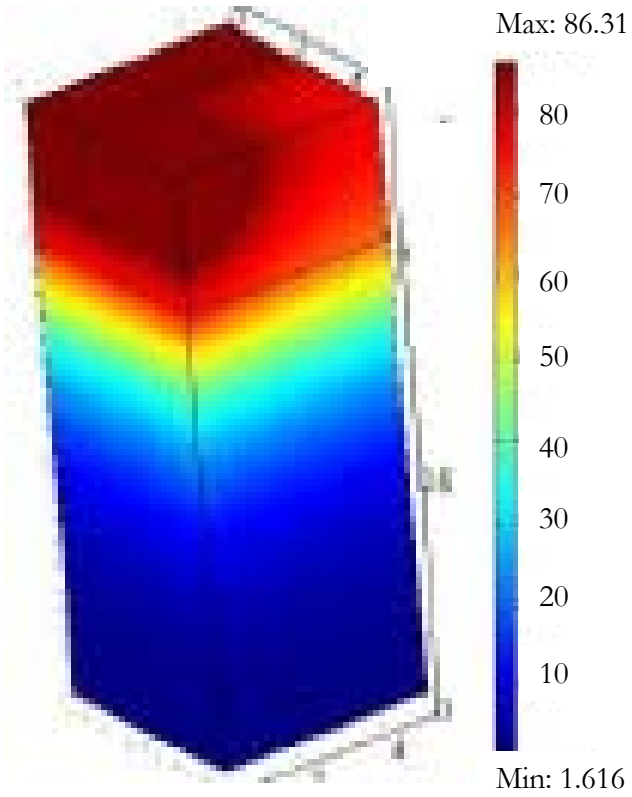

Figure 4.11: Membrane and catalyst temperature (T) rise at 10 ms under $2x10^6$ W/m^2 heating pulse.

where C_p denotes the specific heat capacity, T is the temperature, k is the thermal conductivity, ρ is the density, u is the velocity vector and Q is a sink or source term.

The physical properties for the mesh heater, the catalyst, and the electrolyte layer were set using the sub-domain setting panel. The boundary conditions were set as thermal insulators, except for the mesh heater boundaries, which were simulated by specifying a heat flux value. Lagrange quadratic elements were used with the degrees of freedom close to 40,000. The total number of elements used was about 25,000 and the total number of boundary elements used was close to 4,000. A time step of 0.002 second was used in the solver, and the GMRES linear system solver was used with an assembly block size of 5,000. Based on the calculation, a pulsed heating could raise the catalyst temperature by 80°K after 10 milliseconds of applying the pulsed heating, while keeping most of the neighboring membrane at a temperature increase of less than 10°K as shown in figure 4.11.

4.3 Thermal Stress in SOFC Fabrication

The thermal stress is developed during SOFC fabrication in High Temperature Vacuum Tube Furnace (HTVTF). Numerical modeling is conducted for thermal stress in HTVTF.

High Temperature Vacuum Tube Furnace (model number GSL1600X, manufactured by MTI Corporation, USA) is a precision bench-top furnace using $MoSi_2$ as heating element This vacuum tube can be heated up to 1600°C (1872°K, 2912°F).

At first, the ceramic vacuum tube is inserted into the furnace from back side and then the screw is tightened to fix the tube's position with the holder of the furnace. The material that requires heating is placed at the middle of the tube. Inside the tube, the porous cylindrical alumina 'Blocks' are placed at both the ends. However, the ends of the tube are closed with vacuum cover and the heater is turned on. The air within the furnace and the tube, eventually heats up due to convection by

the electric heater. The major portion of the heat will dissipate by natural convection to the air within the heater and the tube, while the minor portion of heat will be conducted through the furnace to the lab temperature. Then, the heat conducts through the cylindrical inner wall of the tube and will dissipate to the air inside the tube. Figure 4.12 shows a HTVTF with the necessary accessories attached with it.

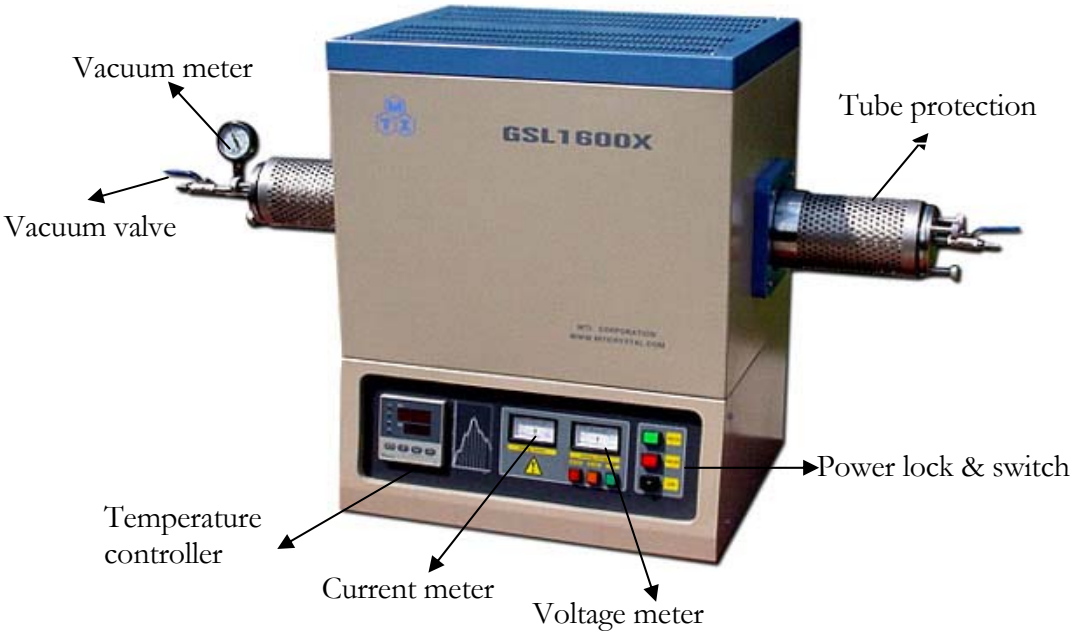

Figure 4.12: HTVTF showing different parts (from MTI corporation, Inc.)

Figure 4.13: Various components of HTVTF

The various dimensions for the HTVTF are shown in table 4.1 as mentioned by MTI Corporation. In order to heat up and sintering the thin film it is necessary that the HTVTF works properly. During this study, it is found that almost all the alumina pipes fractured during the operation of the furnace. A fractured and an actual alumina tube in front of HTVTF are shown in

figure 4.14. The left side of the fractured tube clearly shows the fracture inside the tube that may be attributed to high thermal stress generated by temperature difference in the inner and outer tube wall.

Table 4.1: HTVTF design parameters by MTI corporation manual

Property	**Value (mm)**
Furnace length	550
Furnace width	270
Block length	130
Block radius	35
Air region length	270
Air region (inside furnace) width	35
Tube thickness	5
Tube inside radius	35

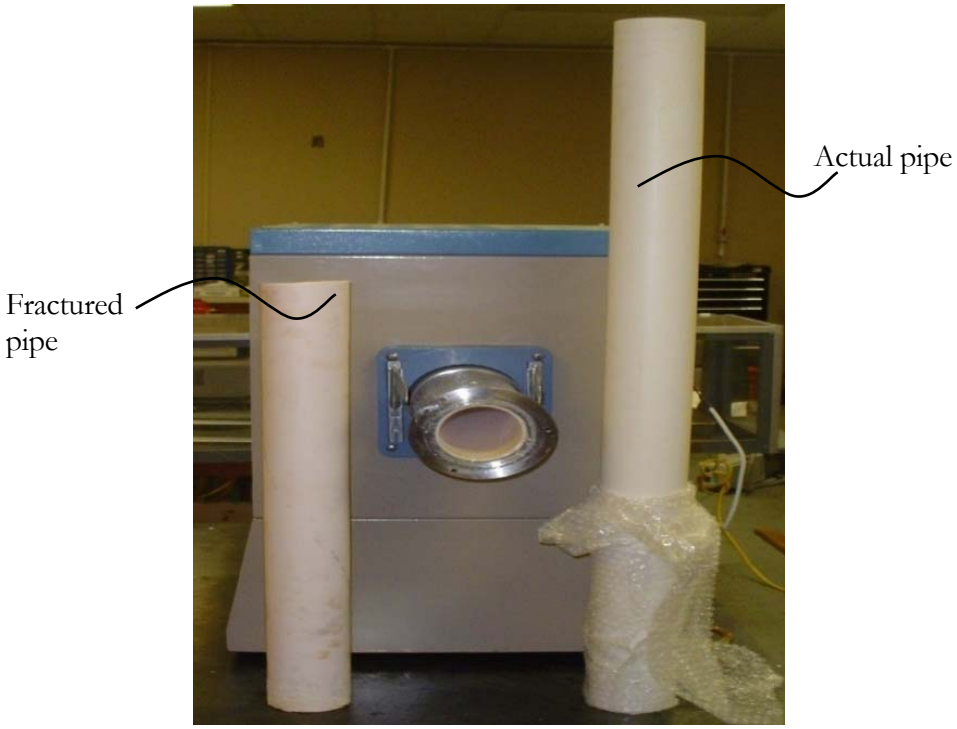

Figure 4.14: Fractured tube with actual tube in front of the HTVTF

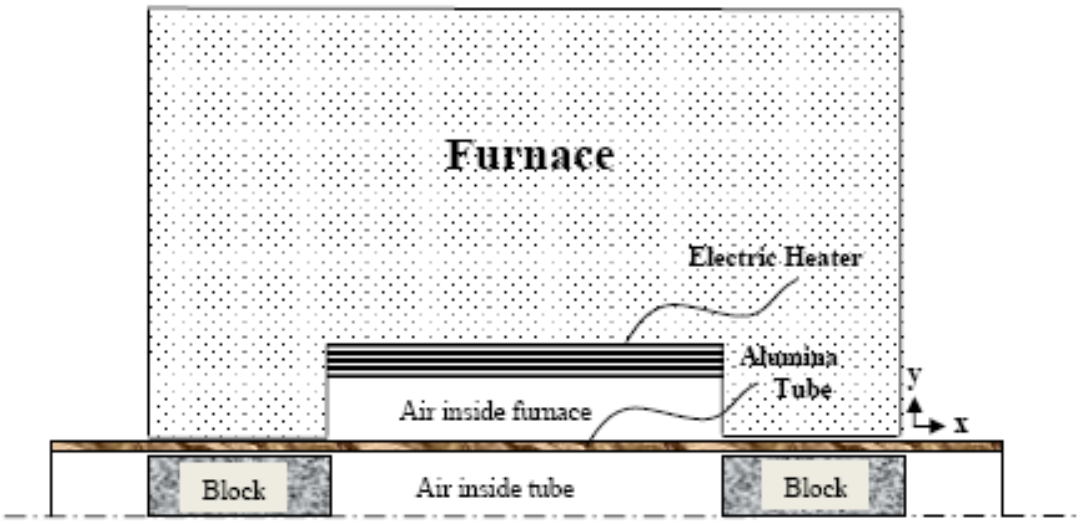

Figure 4.15: Vacuum tube furnace with porous blocks inside tube geometry at both entrances

A symmetric 2D numerical model of HTVTF with alumina tube at the interface of block and furnace lower wall, cylindrical porous alumina blocks at both ends inside tube and electric heater at the top are shown in figure 4.15. For this 2D symmetric model is chosen to save computation time and to assume that the bottom as well as the top part of the furnace will act similarly; with symmetry existing for geometry, loads, and boundary conditions. Cylindrical blocks help keeping heated air inside the tube and heat cannot dissipate or escape through the vacuum sealing cover of the tube or lower the furnace temperature.

The FE (Finite Element) meshing of the numerical model is shown in figure 4.16. Condensed meshing is used at the interface region of the blocks and the surrounding area of the tube as these regions are affected by fracture due to excessive thermal stress generation by temperature difference.

This model involves air flow, heat transfer and thermal stress analysis using linear coefficient of thermal expansion (CET) assumption. For simulation, the values for various constants and parameters are shown in table 4.2 at assuming average temperature inside furnace is at 1700 ^{0}K.

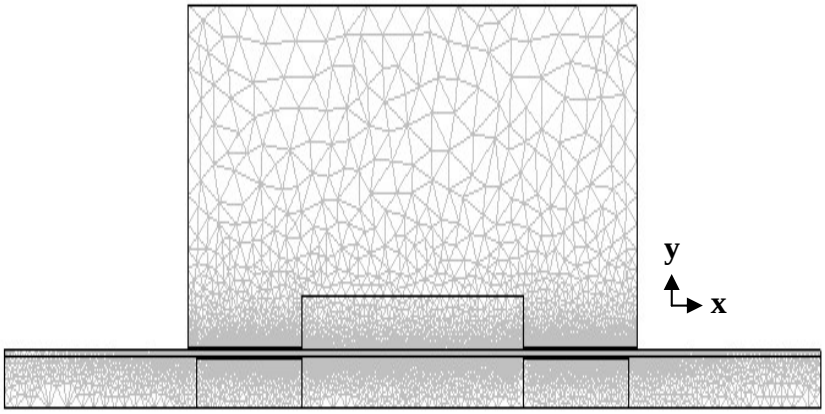

Figure 4.16: Meshing of the different furnace domains

Table 4.2: Constants and parameters used in simulation by Materials properties

Variable	**Definition**	**Value**
$E_{Alumina}$	Modulus of Elasticity of alumina	$3.5x10^{11}$ Pa
$\rho_{alu\ \min}$	Density of alumina	3900 kg/m^3
$c_{p,alu\ \min}$	Heat capacity of alumina	1050 J/kg-°K
$\kappa_{alu\ \min,\ furnace}$	Thermal conductivity of alumina in furnace	39 W/m-^{0}K
α	Thermal expansion coefficient of alumina tube	$9.6x10^{-6}$/^{0}K
ε	Poisson's ratio of alumina	0.33
μ	Dynamic Viscosity of air	$4.96x10^{-5}$ Pa-s
ρ_∞	Density of air at ambient temperature	0.2679 kg/m^3
$c_{p,air}$	Heat capacity of air	1189 J/kg-°K
κ	Thermal conductivity of air	0.082 W/m-^{0}K
T_{heater}	Temperature of heater	1872 ^{0}K
g	Gravitational acceleration	9.8 m/s^2

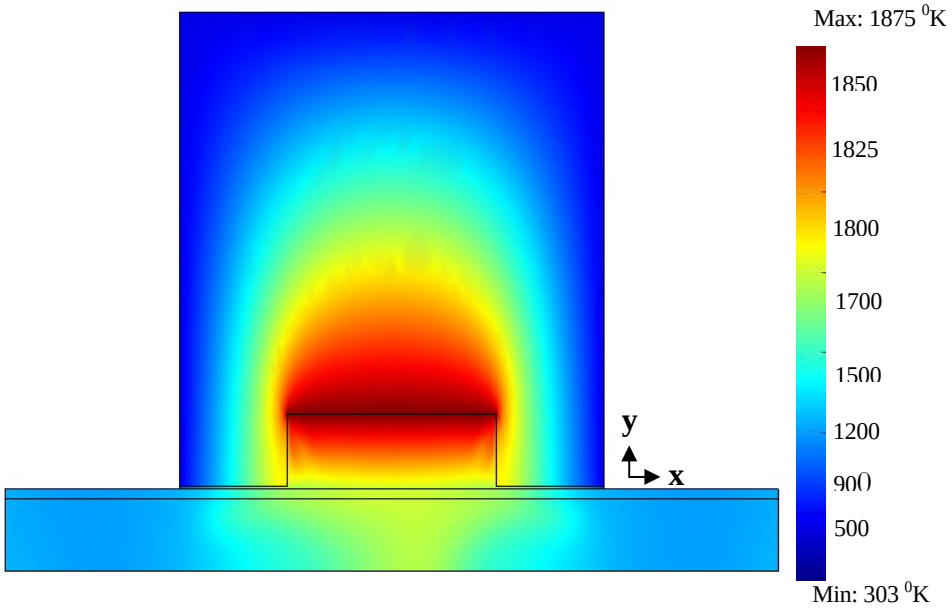

Figure 4.17: Temperature profile due to natural convection inside the furnace without porous cylindrical alumina blocks

Non-isothermal flow assumption is used inside the furnace and the tube as the furnace temperature will vary in different locations. For flow condition, mass conservation equation is used. It is assumed that heat transfer will occur from higher to lower temperature region of air inside the furnace and the tube by natural convection and these are shown below:

$$u\frac{\partial u}{\partial x}+v\frac{\partial u}{\partial y}=g\beta(T-T_\infty)+\nu\frac{\partial^2 u}{\partial y^2}$$ Natural convection equation Eq. (4.41)

$$\vec{\nabla}\bullet(\rho\vec{u})=0$$ Mass conservation equation Eq. (4.42)

Here, $\beta\ (=\frac{1}{T})$ is volumetric thermal expansion coefficient (/^{0}K) and $\nu\ (=\frac{\mu}{\rho})$ is kinetic viscosity of air (m^2/s). Values of various parameters are shown in tables 4.1 & 4.2. General heat transfer equation is used in every domain. Mostly heat conduction equation is used in the tube and furnace which are solid substance and the convection equation is used in the domain which contains air.

$$\vec{\nabla} \bullet (-\kappa \vec{\nabla} T) + \rho c_p \vec{u} \bullet \vec{\nabla} T = 0$$ General heat transfer equation Eq. (4.43)

Coupling of thermal stress and temperature data is necessary to use thermal expansion of tube due to temperature variation within the tube. The following simplified equation for linear thermal expansion is used to couple between the two data:

$$\sigma = E \alpha \Delta T$$ Thermal stress due to thermal expansion equation Eq. (4.44)

where, σ is total thermal stress (Pa), E is modulus of elasticity (Pa), α is Coefficient of thermal expansion (/^{0}K), and ΔT is temperature difference (^{0}K).

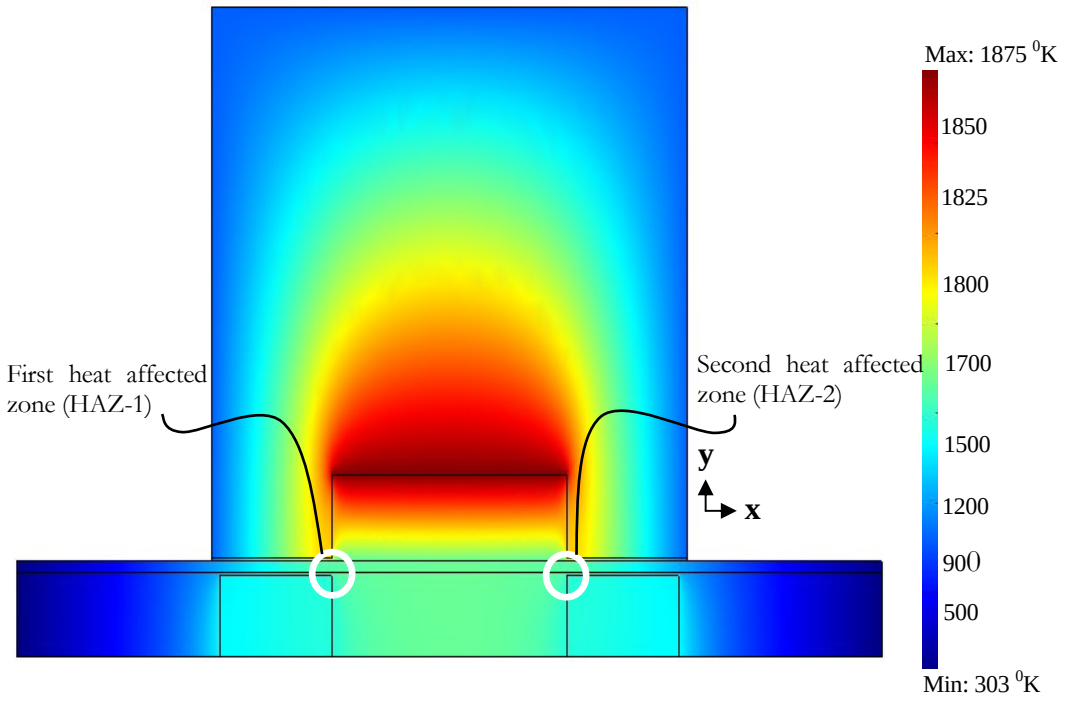

Figure 4.18: Temperature profile with cylindrical blocks and no inlet gas flow condition

Boundary conditions have been defined as upper wall of air inside furnace at heater temperature condition which is 1872^{0}K. For the bottom part symmetric boundary condition for momentum equation and zero heat flux condition for heat equation have been considered. Most of the boundary conditions have been considered as continuity boundary conditions to get value from the surrounding domains. No-slip flow boundary conditions have been considered for wall surfaces.

To complete best heating and sintering thin films temperature profile from FE analysis without blocks inside tube considering natural convection only inside furnace and tube are shown in the following figure 4.17. High temperature from the middle of the furnace convect and distribute at the tube two ends.

To avoid heat loss at the both ends of tube, blocks are necessary to place inside tube. It will also help user from accidental thermal shock if touched during the operation of the furnace. Temperature profile considering natural convection with blocks inside tube is shown in figure 4.18. The heater is placed near the top part of the furnace and for that reason high temperature (1875^0K) exists at the middle of the furnace wall compare to ends of tube. Two HAZs for higher temperature difference between inner and outer wall of tube have been detected and are shown in figure 4.18. This study also found the lab alumina tubes fractured in these zones.

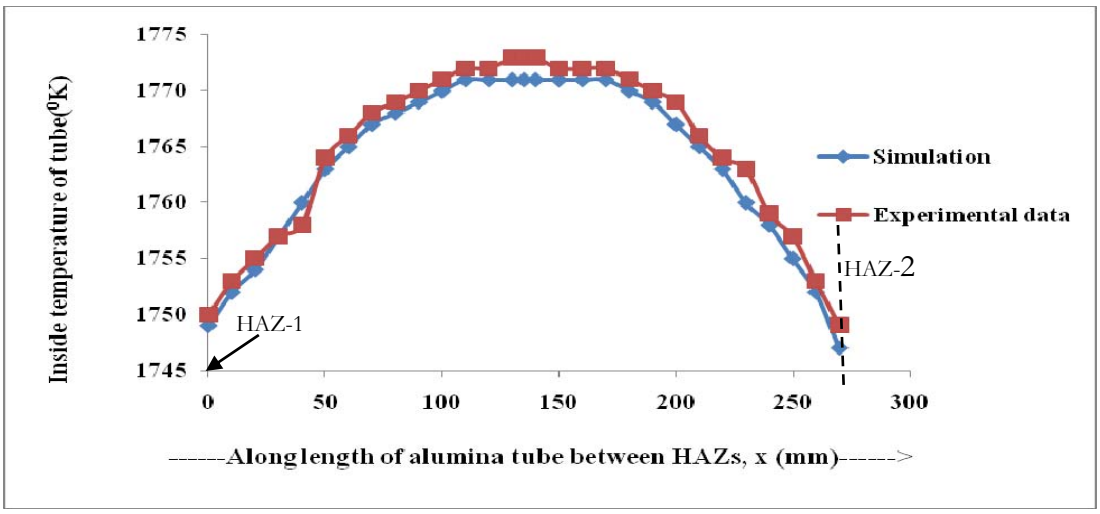

Figure 4.19: Experimental and simulation result of inside temperature of the tube between HAZs.

Temperature data for the inner wall between HAZs along the tube have been calculated from the simulation and is shown in figure 4.19. Data indicates very high temperature at the middle of the tube which decreases gradually at the two HAZs of tube due to heat convection from electric heater to HAZs. Comparison between simulation results and experimental data provided by MTI

Corporation are also shown. A correlation is found between these two sets of data.

It is found that, blowing air at the inner side of the tube has some effect on blowing out the heated air from inside of the furnace. However, this process will decrease inner tube wall temperature which can cause sudden fracture of the alumina tube. To blow out the heated air so that it cannot accumulate inside the alumina, a small pipe with a diameter of 1 mm is inserted inside the block. It blows heated air to the HAZ-2. This pipe is inserted from the inlet side to the end of first block inside the alumina tube. The air inside this small pipe will take heat from the heated tube and will blow hot air mostly on HAZ-2. Due to higher temperature from hot air flow on HAZ-2, the temperature difference can be reduced for inner side of tube wall as for air flow rate of 5 ml/min shown in figure 4.19.

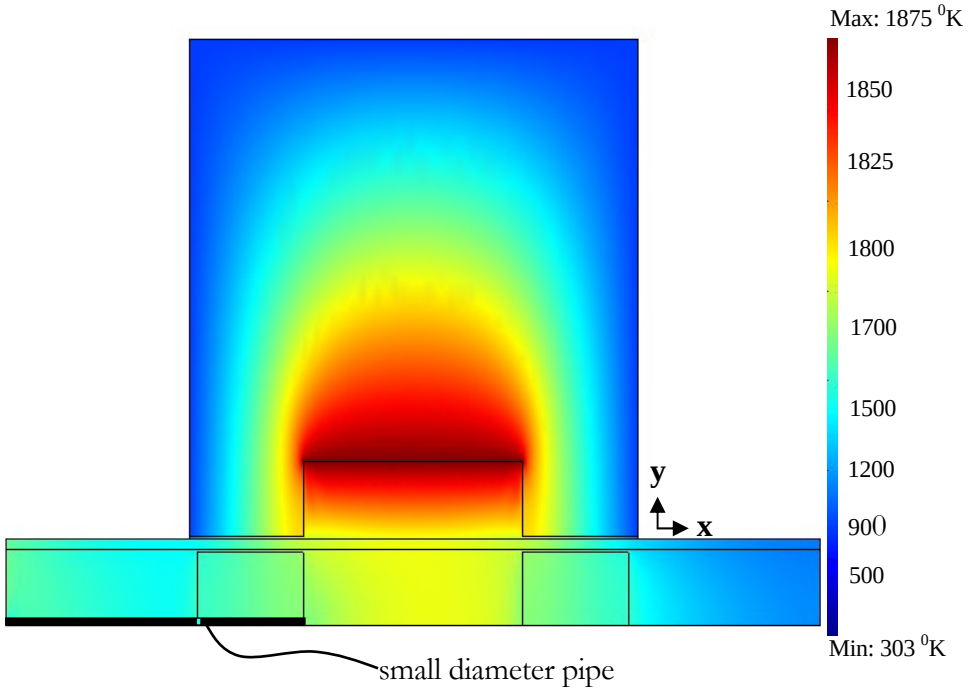

Figure 4.20: Temperature profile for the furnace while a small pipe is inserted inside the block

A relation between air flow rate and thermal stress generation is important to find out critical air flow rate to operate the furnace. From analysis the relation between air flow rates with thermal stress (MPa) have been found and it indicates 20 ml/min flow rate leads to fracture of the tube. This

is because in that flow rate thermal stress becomes 55 MPa maximum flexural strength of alumina tube at 1700 ^{0}K as specified by MTI Corporation assuming average furnace temperature at that temperature. A flow rate lower than this, is desirable for operating purpose of furnace. However, higher flow rate than this will fracture the tube. Once the small pipe with the diameter of 1 mm is inserted inside the block, thermal stress will be reduced. At higher air flow rates than 35 ml/min higher temperature difference will be generated in HAZ-2 and the alumina tube will fracture even when the small pipe is used.

Combined effect of low air flow rate (below 35 ml/min) and insertion of a small diameter pipe inside the first block to blow hot gas on HAZ-2 can increase furnace life expectancy. Therefore, these two factors have to be considered judiciously while operating this HTVTF to heat up or sintering thin film.

4.3.1 Conclusion on Thermal Stress in SOFC Fabrication

In this study, independent mathematical models are developed using multiphysics software Comsol® to understand stress concentration of tube wall and HAZs of a HTVTF. Simulation results have been shown for temperature profile. Combination of thermal stress with temperature difference determine fracture region. Different air flow rates have been considered to find out the critical thermal stress region inside the vacuum tube and found 20 ml/min critical air flow rate without inserting small diameter pipe inside blocks. It is recommended that 1 mm small diameter pipe may be inserted inside the first cylindrical block from the left hand end of vacuum tube inlet to blow hot air of maximum 35 ml/min on HAZ-2 may protect from thermal stress inside the vacuum tube and can save from eventual fracture of vacuum tube.

4.4 Liquid Droplet Dispersion at the Interface of GDL-GFC

In this study, a steady two dimensional, isothermal model of gas transport in a PEMFC is

developed and solved. The numerical simulation results were compared to those published by Um, Wang, and Chen, 2000. The model considers conservation of mass, momentum, species and charge. The cathode gas is assumed humidified air (Oxygen, water and nitrogen) and the anode gas is humidified hydrogen (hydrogen and water).

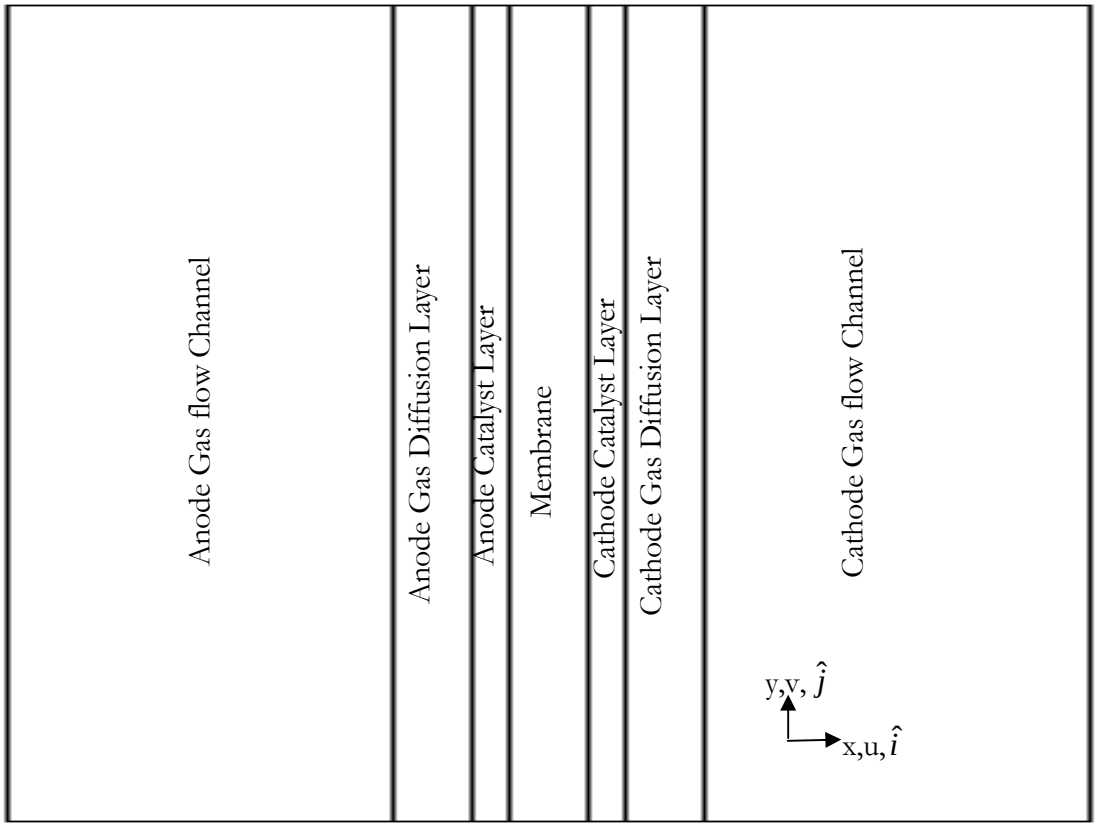

Figure 4.21: Fuel cell geometry.

This numerical analysis describes fuel cell saturation phenomena in seven (7) regions: cathode gas flow channel, diffusion layer and catalyst layer; the membrane; and the anode catalyst layer diffusion layer, and gas flow channel. For this study and assembly, the following assumptions are applied: the domain of interest is two-dimensional (2D), the membrane is non-porous, gases are assumed to follow the ideal gas model, flow is assumed to be incompressible and laminar, cathode and anode gases flow parallel and in the same direction, water exists in the vapor, on the cathode side water is supplied by electrochemical reaction, electro-osmotic drag from the anode and humidified

airflow, and the cell is isothermal.

Figure 4.21 shows fuel cell geometry with different components. This geometry contains membrane in the middle, catalyst layers on the both sides of membrane, gas diffusion layers (GDL) on both sides of catalyst layer, gas flow channel on the both sides of GDL.

The governing equations that are used include conservation of mass, conservation of chemical species, conservation of momentum, and conservation of charge (ionic and electronic). Constitutive relationships including the Darcy equation for pressure drop in porous media and the Butler-Volmer equation for electrochemical kinetics complete the description of fuel cell phenomena.

Mass conservation requires that the difference between the mass flowing in and out of a volume must be stored within the volume. For the steady case considered here, there is no mass storage and equation for mass conservation mass is given by:

$$\nabla \bullet (\rho u) = 0 \qquad \text{Eq. (4.45)}$$

For multi-component species flow, the transport of a particular species is given by the flow of the mixture plus the flow of the species of interest relative to the other species. For the case of steady flow, there is no accumulation of any species and species conservation indicates that the net flux of each species is zero.

For diffusion process in porous region one species will diffuse to other species so Maxwell-Stephan diffusion is needed to handle this kind of binary diffusion process. Numerical simulation software Comsol has capability to use this kind of binary diffusion as well as convection.

$$\nabla \bullet \left[-\rho w_i \sum_{k=1}^{2} D_{ik} \left(\nabla x_k + (x_k - w_k) \frac{\nabla p}{p} \right) + w_i \rho u \right] = 0 \qquad \text{Eq. (4.46)}$$

here, ρ =density of the mixture, w_k = mass fraction of each species, D_{ik} = diffusivity for the pair of gases

where,

$$\sum w_k = 1 \qquad \text{Eq. (4.47)}$$

$$x_k = \frac{w_k MW_{mix}}{M_k} \qquad \text{Eq. (4.48)}$$

Conservation of momentum in the gas flow channels is described by the Navier-Stokes equation.

$$\rho(u \bullet \nabla)u = -\nabla p + \nabla \bullet \mu(\nabla u) \qquad \text{Eq. (4.49)}$$

During electrochemical reaction, two kinds of charged particles are transported: one is protons and another is electrons. The protons move through the polymer phase and electrons move through the carbon phase of the electrodes.

In the steady case, ionic charge conservation equation requires that the net efflux of charge will be equal to the production of charged ionic species. In the anode, catalyst layer ionic charge is transported through the membrane due to a gradient in potential, and charge is generated in proportion to the current. Therefore, conservation of ionic charge at the anode is given by:

$$\nabla \bullet \left(\kappa_{ia}^{eff} \nabla \phi_i\right) - S_{aa} i_{act} = 0 \quad \text{anode side} \qquad \text{Eq. (4.50)}$$

where, S_{aa} denotes specific surface area of the electrode, i_{act} denotes current density and κ_{ia}^{eff} denotes the effective ionic conductivity in the catalyst layer at anode side.

In the cathode catalyst layer, ionic charge is transported through the polymer phase due to a gradient in potential and charge is consumed in proportion to the current. Therefore, charge conservation equation becomes:

$$\nabla \bullet \left(\kappa_{ic}^{eff} \nabla \phi_i\right) + S_{ac} i_{cct} = 0 \quad \text{cathode side} \qquad \text{Eq.(4.51)}$$

where, κ_{ic}^{eff} denotes the effective ionic conductivity in the catalyst layer at cathode side

As, the membrane contains no ionic source or sink,

$$\nabla \bullet \left(\kappa_i \nabla \phi_i \right) = 0 \quad \text{membrane} \qquad \text{Eq. (4.52)}$$

where, κ_i denotes the ionic conductivity in the membrane.

In the steady case, conservation of electronic charge requires that the net efflux of charge be equal to the production of charged electronic species. In the anode, catalyst layer electronic charge is transported through carbon phase and outside circuit due to a gradient in potential, and charge is generated as a result of hydrogen oxidation in proportion to the current. Therefore, electronic charge conservation at the anode is given by:

$$\nabla \bullet \left(\kappa_{ea}^{eff} \nabla \phi_e \right) + S_{aa} i_{act} = 0 \quad \text{anode side catalyst layer} \qquad \text{Eq. (4.53)}$$

where κ_{ea}^{eff} denotes electronic conductivity at anode side.

In the cathode catalyst layer, electronic charge is transported through the carbon phase due to a gradient in potential and charge is consumed in proportion to the current. Therefore, electronic charge conservation becomes:

$$\nabla \bullet \left(\kappa_{ec}^{eff} \nabla \phi_e \right) - S_{ac} i_{cct} = 0 \quad \text{cathode side catalyst layer} \qquad \text{Eq. (4.54)}$$

where κ_{ec}^{eff} denotes electronic conductivity at cathode side.

As, gas diffusion layer contains no electronic source or sink,

$$\nabla \bullet \left(\kappa_{ea}^{eff} \nabla \phi_e \right) = 0 \quad \text{anode side gas diffusion layer} \qquad \text{Eq. (4.55)}$$

$$\nabla \bullet \left(\kappa_{ec}^{eff} \nabla \phi_e \right) = 0 \quad \text{cathode side gas diffusion layer} \qquad \text{Eq. (4.56)}$$

Within porous media, the flow can often be described by a balance of viscous effects and pressure effects. In addition to using other equations this relationship is modeled by the Darcy equation.

$$u = -\frac{\kappa}{\mu}\nabla p \qquad \text{Eq. (4.57)}$$

After the electrochemical reaction current field that produced in the MEA part leads to the well known Butler-Volmer equation. As products and reactants gases, concentrations are almost similar so we get a simplified form of Butler-Volmer equation which is used in catalyst layer regions.

$$i = i_o\left(\frac{C_R^*}{C_R^{o*}}e^{\frac{\alpha nF\eta}{RT}} - \frac{C_P^*}{C_P^{o*}}e^{-\frac{(1-\alpha)nF\eta}{RT}}\right) \qquad \text{Eq. (4.58)}$$

$$= i_o\frac{C_R^*}{C_R^{o*}}\left(e^{\frac{\alpha nF\eta}{RT}} - e^{-\frac{(1-\alpha)nF\eta}{RT}}\right) \qquad \text{Eq. (4.59)}$$

where, F = Faradday constant, i_o = Exchange current density, α =Charge transfer coefficient and η =Overpotential

In electro-osmotic drag, electron that produces in anode side will eventually be dragged by water particle in anode side to cathode side of cell. It played a major role to find out value of electro-osmotic drag coefficient in simulating PEMFC.

Electro-osmotic drag coefficient, [Springer, Zawodiski, and Gottesfield (1991)]

$$n_{drag} = n_{drag}^{SAT}\frac{\lambda}{22}$$

$$= 0.114\lambda \qquad \text{Eq. (4.60)}$$

Water with polymer electrolyte played also a role in finding water drag coefficient. Water content in the membrane, [Springer, Zawodiski, and Gottesfield, 1991]

$$\lambda = 0.043 + 17.81a - 39.85a^2 + 36a^3 \quad \text{for} \quad 0 < a \le 1 \qquad \text{Eq. (4.61)}$$

$$= 14 + 1.4(a-1) \quad \text{for} \quad 1 \le a \le 3 \qquad \text{Eq.(4.62)}$$

From thermodynamics, we know water activity, $a = \frac{x_{H2O}p}{p^{sat}}$ Eq. (4.63)

Mass flux involved with this electro-osmotic drag [O'Hayre, Cha, Colella, and Prinz (2005)],

$$J_{H_2O,drag} = 2n_{drag}\frac{j}{2F} \qquad \text{Eq. (4.64)}$$

However, some water particle that generates in cathode side will eventually tend to diffuse in anode side due to concentration difference. Mass flux involved in back diffusion of water particle [O'Hayre, Cha, Colella, and Prinz, 2005]:

$$J_{H_2O,backdiffusion} = -\frac{\rho_{dry}}{M_m} D_\lambda \frac{d\lambda}{dx} \qquad \text{Eq. (4.65)}$$

A balance with mass flux of electro-osmotic drag water particle and back diffusion water particle is needed so that the membrane will not dry and will eventually hydrate on both of its sides.

In addition to that water that resides inside membrane is needed to complete calculation of drag coefficient. Water diffusivity in Nafion, [Motupally, Becker, and Weidner (2000)]

$$D_\lambda = 10^{-6} \exp\left[2416\left(\frac{1}{303} - \frac{1}{T}\right)\right]\left(2.563 - 0.33\lambda + 0.0264\lambda^2 - 0.000671\lambda^3\right) \qquad \text{Eq. (4.66)}$$

During application of ionic conservation equation it is needed to find out Nafion^{TM} Conductivity, [Meredith and Tobias, 1962]

$$\kappa(T,\lambda) = \kappa_{303K} \exp\left[1268\left(\frac{1}{303} - \frac{1}{T}\right)\right] \qquad \text{Eq. (4.67)}$$

where, $\kappa_{303K}(\lambda) = 0.005193\lambda - 0.00326$

The diffusion coefficient of species and ionic conductivity of the membrane phase are effective values modified by Bruggman correlation [Meredith and Tobias (1962)] to account for the effects of porosity and tortuosity in porous electrodes and catalyst layers.

$$D_k^{eff} = \varepsilon_m^{1.5} D_k \qquad \text{Eq. (4.68)}$$

$$\kappa_k^{eff} = \varepsilon_m^{1.5} \kappa_k \qquad \text{Eq. (4.69)}$$

For ionic and electronic current balances insulating boundary conditions are considered in different regions except for the interface between the gas flow channels and gas diffusion layer, where potential for anode side considers zero and for cathode side considers the cell voltage.

The components mass balance for the boundary conditions are all insulating conditions

except for the inlet and outlet boundary of the channel. At the channel inlet boundary, the mass fractions are given values. The condition at the outlet is a so-called convective condition, where it is assumed that convection dominates the flux in the main direction of the flow.

The **s**even (7)-layers of PEMFC is meshed at first in Comsol by using the GUI (Graphic User Interface). Brick type of mesh elements was chosen for this work. More meshing is used in the MEA (membrane electrode assembly) part as it has dominating role due to electrochemical reaction in that region.

Table 4.3: Electrochemical data

Variable	**Definition**	**Value used in simulation**	**Source**
F	Faraday constant	96487 coulomb/mol	Um, Wang and Chen (2000)
i_{oa}	Exchange current density at anode side	500000000 amp/m^2	Um, Wang and Chen (2000)
i_{oc}	Exchange current density at cathode side	100 amp/m^2	Um, Wang and Chen (2000)
R	Universal gas constant	8.314 J/(mol-K)	Um, Wang and Chen (2000)
$\Delta\phi_a$	Phase potential at anode side	0 volt	Comsol (2005)
$\Delta\phi_c$	Phase potential at cathode side	1 volt	Comsol (2005)
κ_{ea}^{eff}	Electronic conductivity of anode side catalyst layer	1000 S/m	Comsol (2005)
κ_{ec}^{eff}	Electronic conductivity of cathode side catalyst layer	1000 S/m	Comsol (2005)
κ_i	Ionic conductivity of membrane	3.273 S/m	Eq.[4.52]
κ_{ia}^{eff}	Ionic conductivity of catalyst layer in anode side	0.8279 S/m	Eq.[4.50]
κ_{ic}^{eff}	Ionic conductivity of catalyst layer in cathode side	0.8279 S/m	Eq.[4.51]
n	Number of electron transferred	2	Assumed
n_{drag}	Electro-osmotic drag coefficient	1.758	Eq.[4.60]

Table 4.4: Physical property data

Variable	Definition	Value used in simulation	Source
ρ	Density of gas	Dependent variable	NA
T	Temperature	353 K	Um, Wang and Chen (2000)
p_{ref}	Reference pressure	101350 Pa	Assumed
T_{ref}	Reference temperature	273 K	Assumed
M_{O_2}	Molecular weight of oxygen	0.032 kg/mol	Assumed
M_{N_2}	Molecular weight of nitrogen	0.028 kg/mol	Assumed
M_{H_2O}	Molecular weight of water	0.018 kg/mol	Assumed
M_{H_2}	Molecular weight of hydrogen	0.002 kg/mol	Assumed
κ_p	Permeability of gas diffusion layer	0.0000000000176 m^2	Um, Wang and Chen (2000)
μ_c	Viscosity of cathode side air	0.00001 Pa-s	Um, Wang and Chen (2000)
μ_a	Viscosity of anode side gas	0.0001948 Pa-s	Um, Wang and Chen (2000)
M_{mixc}	Molecular weight of mixture at cathode side	0.0288	O'Hayre, Cha, Colella, Prinz (2005)
M_{mixa}	Molecular weight of mixture at anode side	0.0088	O'Hayre, Cha, Colella, Prinz (2005)
ε	Porosity of GDL	0.4	Um, Wang and Chen (2000)
$D_{O_2H_2O}$	Diffusivity of O_2 in H_2O vapor	0.00002944 m^2/s	O'Hayre, Cha, Colella, Prinz (2005)
$D_{N_2H_2O}$	Diffusivity of N_2 in H_2O vapor	0.00007127 m^2/s	O'Hayre, Cha, Colella, Prinz (2005)
$D_{O_2N_2}$	Diffusivity of O_2 in N_2	0.00002734 m^2/s	O'Hayre, Cha (2005)
$D_{H_2H_2O}$	Diffusivity of H_2 in H_2O vapor	0.0001050 m^2/s	O'Hayre, Cha (2005)

Table 4.5: Inlet conditions

Variable	Definition	Value used in simulation	Source
V_{ina}	Anode side inlet velocity	0.2265 m/s	Um, Wang and Chen (2000)
V_{inc}	Cathode side inlet velocity	0.2009 m/s	Um, Wang and Chen (2000)
ζ_a	Anode side stoichiometry	2.8	Um, Wang and Chen (2000)
ζ_c	Cathode side stoichiometry	3	Um, Wang and Chen (2000)
x_{O_2}	Mole fraction of oxygen at cathode side	0.209	Um, Wang and Chen (2000)
x_{N_2}	Mole fraction of nitrogen at cathode side	0.7867	Um, Wang and Chen (2000)
x_{H_2Oc}	Mole fraction of water at cathode side	0.0043	Um, Wang and Chen (2000)
x_{H_2}	Hydrogen mole fraction at anode side	0.5769	Um, Wang and Chen (2000)
x_{H_2Oa}	Mole fraction of water at anode side	0.4231	Um, Wang and Chen (2000)
p_{in}	Inlet pressure at anode side	304050 Pa	Um, Wang and Chen (2000)

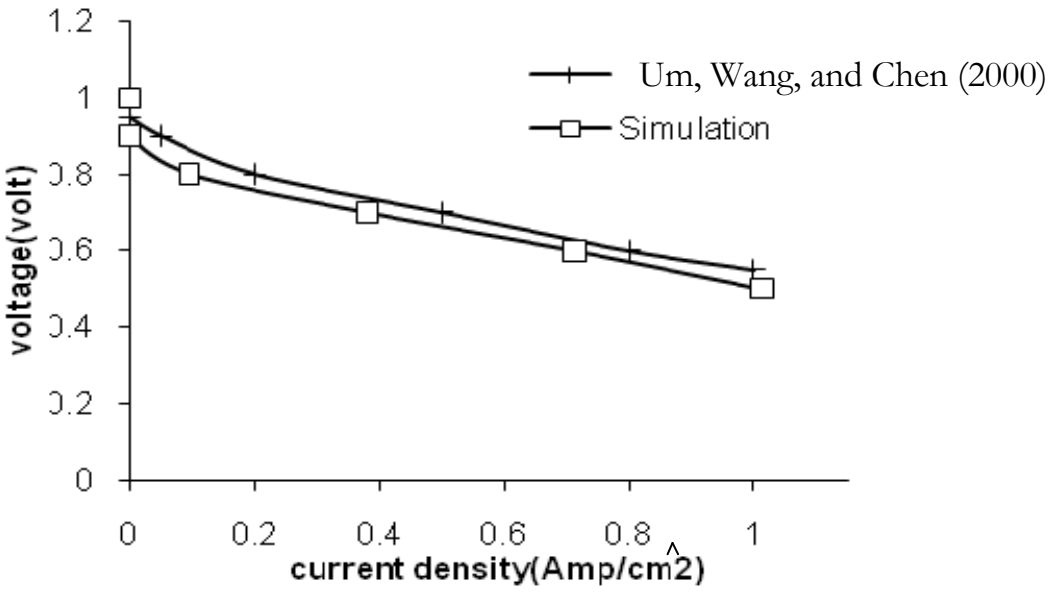

Figure 4.22: Polarization curve of PEMFC

Meshed two-dimensional (2D) PEMFC has been set up for different equations involved in fuel cell electro-chemistry. Various equations involved in 2D fuel cell in different subdomains have been used. A domain has been used for different times for various equations.

Figure 4.22 indicates polarization curve of the simulated cell. Numerical results were compared with data obtained from Um, Wang, and Chen (2000). Curves indicates comparable match between published paper and simulated results by this study.

The presence of liquid water decreases the porosity of the gas diffusion layer. Saturation is defined as the fraction of the free volume filled with water. Thus, the effective porosity is given by [Wang, Wang, and Chen (2001)]:

$$\varepsilon^{eff} = \varepsilon(1-s) \qquad \text{Eq. (4.70)}$$

The dry analysis was based on Um, Wang and Chen (2000), dry porosity considered, $\varepsilon = 0.4$. For, a saturation of $s = 0.25$, Eq.(4.70) gives an effective porosity of 0.3. Similarly, saturation of $s = 0.5$ gives an effective porosity of 0.2. Polarization curve has been drawn for different values of porosity are shown below.

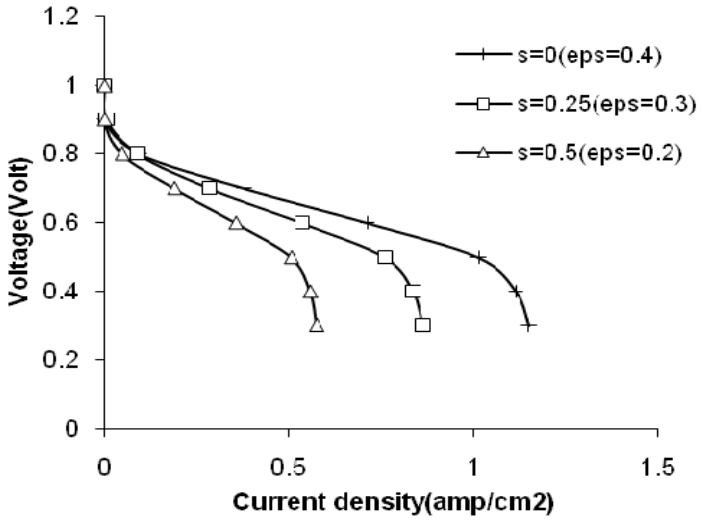

Figure 4.23 Effect of saturation (s) as well as porosity ($\hat{\varepsilon}$) on polarization curve.

With increasing saturation value pores fill with liquid water, so porosity automatically decreases for dry reactant gases in the fuel cell. Due to these phenomena, reacting site will also get less gases and performance of the cell will drop. Porosity variation on polarization curve indicates that with increasing saturation value (that means lowering porosity) will decrease performance of the cell.

Simulation has also been conducted for saturation of $s = 0.875$ which indicates very low effective porosity value of 0.05. During very low porosity value, reactants will face obstacle in going to the reacting catalyst region. In addition, catalyst layer during this very low porosity value will act more like a solid surface for reactant gases with very low tiny pores in it.

Once the physical phenomenon is reflected in the governing equation, the next step is to apply numerical techniques to solve governing equation and boundary conditions. In this work, the CFD program Comsol is used to address this kind of phenomena. When creating a model in Comsol, the typical modeling steps include [Comsol User's guide (2005)]: creating or importing the problem geometry, meshing the geometry, defining the physics on the domains and at the boundaries, solving the model using the proper solver, post processing the solution to see the scenario inside the cell, performing parametric studies.

A single cathode side GDL (gas diffusion layer) has been considered this time with different saturation values at the interface of GDL-GFC and constant mass flux value at the interface of CCL-GDL.

$$-\vec{\nabla} \bullet \left(D_{H_2O}^{l} \vec{\nabla} s \right) = \frac{S_s}{\rho_{H_2O}^{l}} \qquad \text{General equation} \qquad \text{Eq. (4.71)}$$

Here, S_s is source term, which accounts water phase change by evaporation and condensation and water production by electrochemical reaction. Saturation, $s = \frac{V_l}{V_p}$, here, V_l is pore volume occupied

by liquid water and V_p is total pore volume.

$$S_{H_2O} = \frac{M_{H_2O}}{2F} j_c \qquad \text{Eq. (4.72)}$$

For our case, we have considered a single cathode gas diffusion layer (GDL) to simulate two-phase water liquid. As, GDL is considered so for method of simplicity source term due to water phase change during evaporation and condensation is neglected, however source term due to liquid water production after electrochemical reaction is considered.

Liquid water diffusivity,

$$D^l_{H_2O} = \frac{\kappa s^3}{\mu_{H_2O}} \left(\frac{dp_{cap}}{ds} \right) \qquad \text{Eq. (4.73)}$$

For, constant value of slope of capillary pressure, $\left| \frac{dp_{cap}}{ds} \right| = 30321 Pa$ [Nam and Kaviany (2003)]

$$D^l_{H_2O} = \frac{\kappa s^3}{\mu_{H_2O}} \times 30321 \qquad \text{Eq. (4.74)}$$

Assumptions that have been considered for this simulation work are: two-dimensional (2D) simulation is conducted, porous GDL (gas diffusion layer) is only considered for subdomain, water coming to CCL (cathode catalyst layer)-GDL interface due to mass flux of water after electrochemical reaction, electro-osmotic drag and humidified air flow only, Water is considered two phase, GDL-GFC (gas flow channel) interface is variable liquid saturation $s(x, y)$ values, constant value of slope of capillary pressure, $\left| \frac{dp_{cap}}{ds} \right|$

Subdomain equations for this system is:

$$\vec{\nabla} \bullet \left(- D^l_{H_2O} \vec{\nabla} s \right) = 0 \qquad \text{General equation} \qquad \text{Eq. (4.75)}$$

Saturation: $s = \frac{V_l}{V_p}$, here, V_l is pore volume occupied by liquid water and V_p is total pore volume

For, constant value of slope of capillary pressure, $\left|\frac{dp_{cap}}{ds}\right| = 30321Pa$ [Nam and Kaviany (2003)]

Liquid water diffusivity, $D^l_{H_2O} = \frac{\kappa s^3}{\mu_{H_2O}} \times 30321$ where, κ medium permeability, μ is viscosity of liquid water.

Table 4.6: Constants used in simulation

Variable	**Definition**	**Value used in simulation**	**Source**
ρ	Density of water	Variable	NA
F	Faraday Constant	96487 coulomb/mol	Um, Wang, and Chen (2000)
T	Temperature	353 K	Um, Wang, and Chen (2000)
p_{ref}	Reference pressure	101350 Pa	Assumed
M_{H_2O}	Molecular weight of water	0.018 kg/mol	Assumed
γ	Surface tension	0.0719	Um, Wang, and Chen (2000)
θ	Contact angle	114.14^o	Experimental
ε	Porosity of GDL	0.4	Um, Wang, and Chen (2000)
κ	Permeability of GDL	0.0000000000176 m^2	Um, Wang, and Chen (2000)
μ_{H_2O}	Viscosity of water	0.00001 Pa-s	Comsol (2005)

Boundary Conditions for this system are:

$$s = 0, 0.25, 0.5, s = f(y) = \frac{1 + \sin\left(\frac{n\pi y}{L}\right)}{2} \quad \text{GDL-GFC interface} \quad \text{Eq. (4.76)}$$

$$\vec{\nabla} \bullet \left(-D_{H_2O}^{l} \vec{\nabla} s \right) = \frac{\frac{M_{H_2O} j}{2F}}{\rho_{H_2O}^{l}} \qquad \text{CCL-GDL interface} \qquad \text{Eq. (4.77)}$$

The boundary conditions for the other two sides are considered as insulating boundary condition.

In figure 4.23 shows two-dimensional (2D) finite element of gas diffusion layer (GDL) with all boundary conditions.

Liquid Phase Transport model based on Darcy Equation with saturation-capillary pressure function (Leverett Function) [Nam and Kaviany (2003)] is considered. For, variable value of capillary pressure slope, $\frac{dp_{cap}}{ds}$, Leverett Function (J) is used:

$$D_{H_2O}^{l(\theta \approx 114.14)} = -\frac{\gamma s^3 \cos\theta \sqrt{\varepsilon \kappa} (1.417 - 4.240 s + 3.789 s^2)}{\mu_{H_2O}} \qquad \text{Eq. (4.78)}$$

where, κ medium permeability, γ is surface tension, θ contact angle, ε porosity, κ medium permeability, μ is viscosity

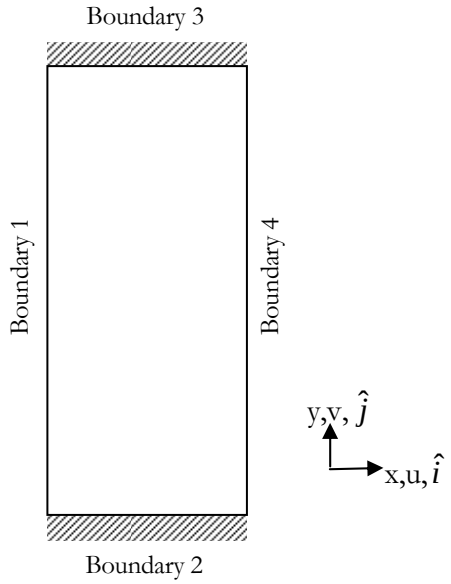

Figure 4.24: Diagram of 2D finite element GDL showing boundary conditions

Equations for Leverett Function:

$$J(s) = 1.417s - 2.12s^2 + 1.263s^3 \quad \text{Eq. (4.79)}$$

Relative permeability for liquid phase, $\kappa_{rl} = s^3$ Eq. (4.80)

Assumptions that have been considered for simulation work for this time are: two-dimensional (2D) simulation is conducted, porous GDL (gas diffusion layer) is only considered for subdomain, water coming to CCL (cathode catalyst layer)-GDL interface due to mass flux of water after electrochemical reaction, electro-osmotic drag and humidified air flow only, water is considered two phase, GDL-GFC (gas flow channel) interface is variable liquid saturation s(x,y) values, variable value of slope of capillary pressure, $\frac{dp_{cap}}{ds}$

$$\vec{\nabla} \bullet \left(- D_{H_2O}^l \vec{\nabla} s \right) = 0 \quad \text{General equation} \quad \text{Eq. (4.81)}$$

Saturation: $s = \frac{V_l}{V_p}$, here, V_l is pore volume occupied by liquid water and V_p is total pore volume

For, variable value of slope of capillary pressure, $\frac{dp_{cap}}{ds} = \left(1.417 - 4.24s + 3.789s^2\right)\gamma \cos\theta \sqrt{\frac{\varepsilon}{\kappa}}$

$$s = 0.5, \quad s = f(y) = \frac{1 + \sin\left(\frac{n\pi y}{L}\right)}{2} \quad \text{GDL-GFC interface} \quad \text{Eq. (4.82)}$$

$$\vec{\nabla} \bullet \left(- D_{H_2O}^l \vec{\nabla} s \right) = \frac{\frac{M_{H_2O} j}{2F}}{\rho_{H_2O}^l} \quad \text{CCL-GDL interface} \quad \text{Eq. (4.83)}$$

The boundary conditions for the other two sides are considered as insulating boundary condition.

Liquid water transport in GDL is analyzed with constant and varying capillary pressure slope.

Saturation values involved in saturation equations are shown in below. Only GDL domain is considered and shown. Left side of the GDL is CCL-GDL interface and right side is GDL-GFC interface. Butler-Volmer equation that is used here: $i = (1-s) i_o \frac{C_R^*}{C_R^{o*}} \left(e^{\frac{\alpha n F \eta}{RT}} - e^{-\frac{(1-\alpha) n F \eta}{RT}} \right)$

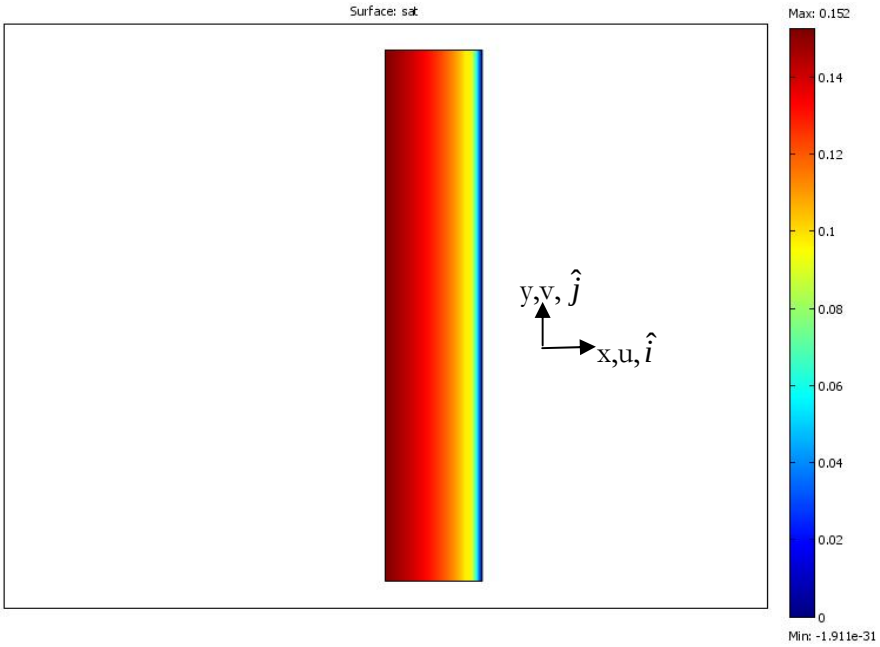

Figure 4.25: Saturation plot for $s = 0$ for constant capillary pressure slope

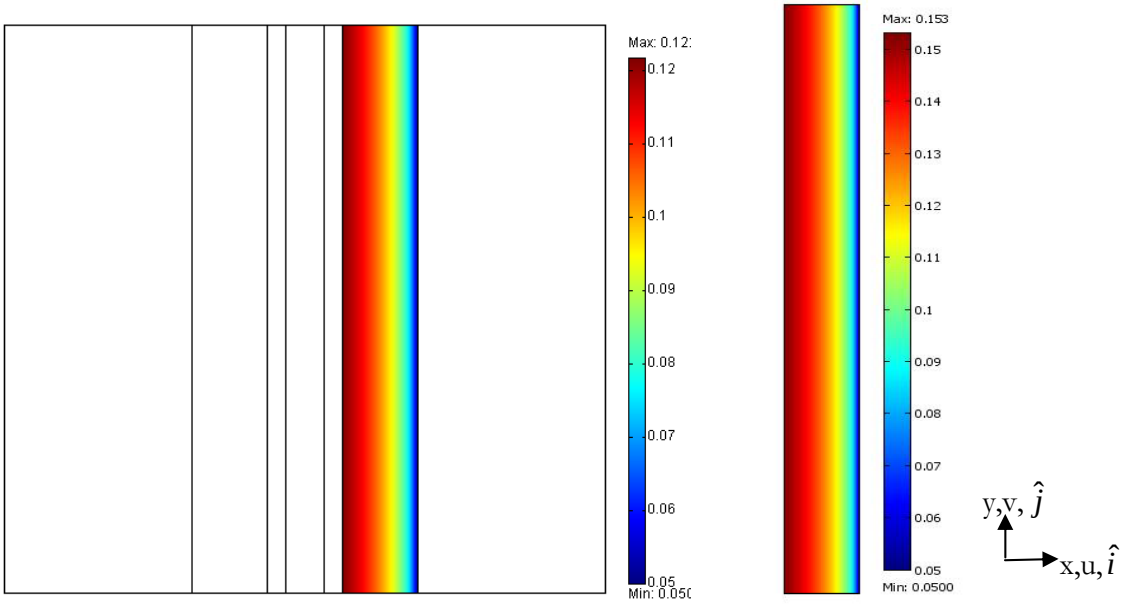

Figure 4.26: Saturation plot for $s = 0.05$ for constant capillary pressure slope.

For saturation value of zero at the interface of GDL-GFC interface Figure 4.25 shows water saturation distribution inside GDL. As saturation (s) is zero (means no saturated liquid water) in the GDL-GFC interface, so no or less saturation is in that side and higher saturation in CCL-GDL interface side. Therefore, there will be flow of saturated liquid water from CCL-GDL interface to GDL-GFC interface.

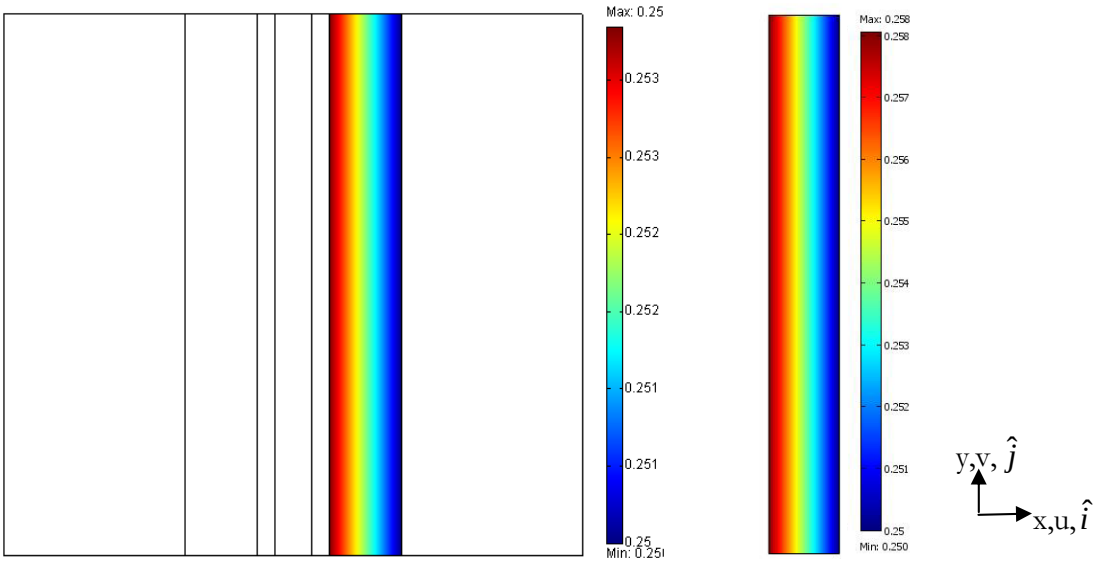

Figure 4.27: Saturation plot for $s = 0.25$ for constant capillary pressure slope.

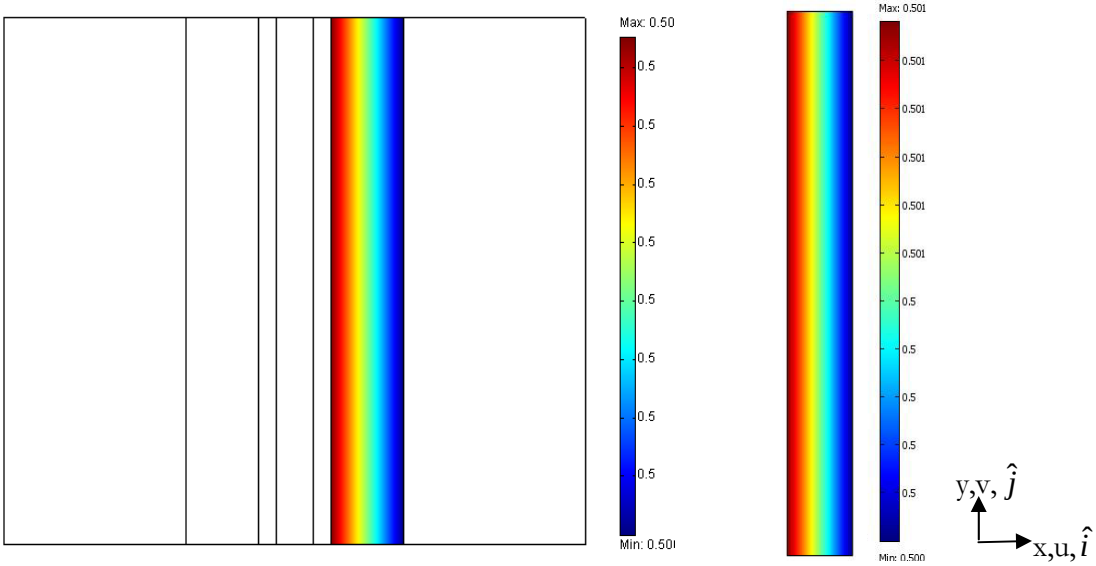

Figure 4.28: Saturation plot for $s = 0.5$ for constant capillary pressure slope.

For saturated liquid water value of one-fourth($s = 0.25$) at the interface of GDL-GFC which means one-fourth of the interface of GDL-GFC is covered with liquid water, Figure 4.27 shows saturation liquid water distribution inside GDL. It has also same direction flow of saturated liquid water from CCL-GDL interface to GDL-GFC interface. As this time there have saturation (liquid water) value at the interface of GDL-GFC so liquid water formation increases near that side compared to zero (0) saturation value at that side.

For saturated liquid water value of half ($s = 0.5$) at the interface of GDL-GFC which means half of the interface of GDL-GFC is covered with liquid water, figure 4.28 shows saturation liquid water distribution inside GDL. It has also same direction flow of saturated liquid water from CCL-GDL interface to GDL-GFC interface.

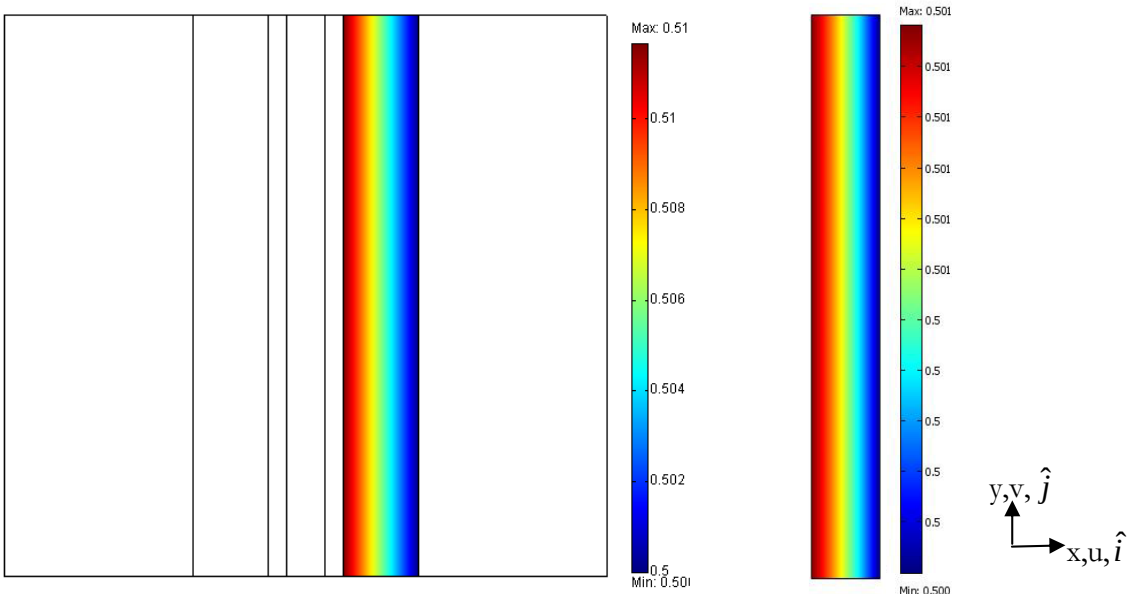

Figure 4.29: Liquid water flux inside GDL for $s = 0.5$ at the interface of GDL-GFC using varying capillary pressure slope.

Figure 4.29 indicates liquid water flux inside GDL for varying capillary pressure slope. It indicates liquid water transport from CCL-GDL interface to GDL-GFC interface.

For saturated liquid water value of one-twentieth ($s = 0.05$) at the interface of GDL-GFC

which means one-twentieth of the interface of GDL-GFC is covered with liquid water, figure 4.30 shows saturation liquid water distribution inside GDL. It has direction flow of saturated liquid water from CCL-GDL interface to GDL-GFC interface.

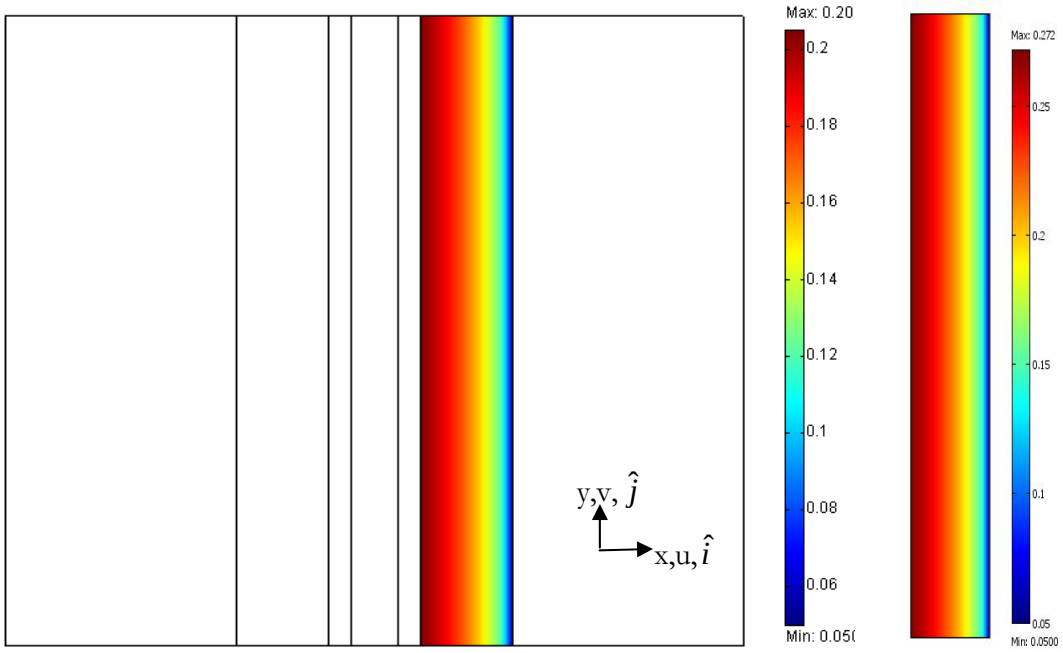

Figure 4.30: Saturation distribution inside GDL for $s = 0.05$ using varying capillary pressure slope.

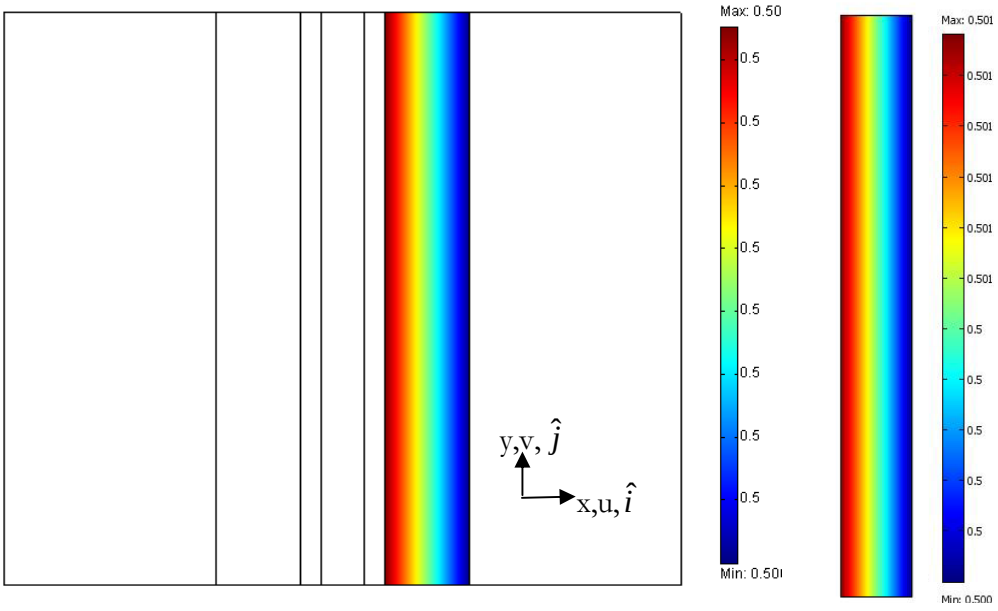

Figure-4.31: Saturation plot for $s = 0.5$ for constant capillary pressure slope.

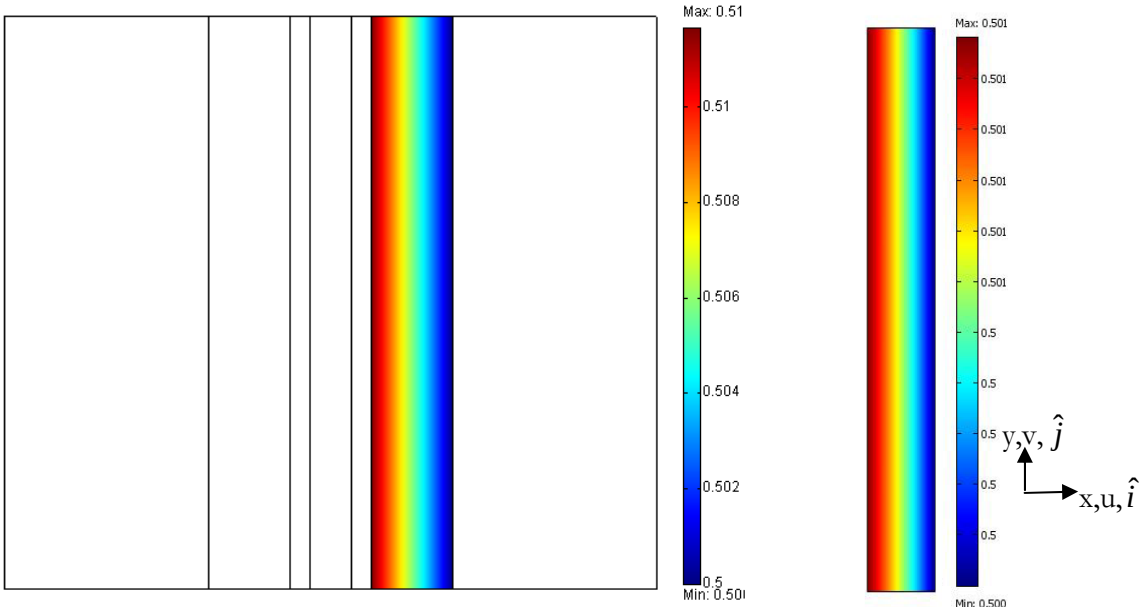

Figure-4.32: Saturation distribution inside GDL for $s = 0.5$ using varying capillary pressure slope.

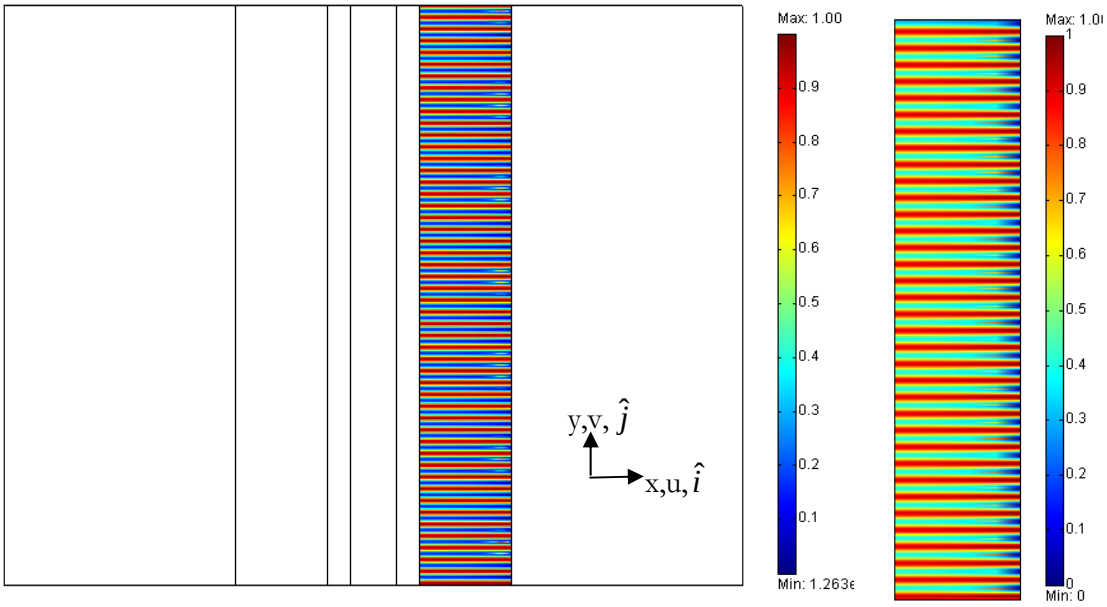

Figure-4.33: Saturation plot with contour plot for a periodic function for constant capillary pressure slope.

Comparing constant and varying capillary pressure slope results indicate almost similar result with a little higher saturation values in varying capillary pressure slope than constant capillary pressure slope. Overall, varying capillary pressure slope is a general case to address liquid water

transport inside GDL.

For saturated liquid water value of half ($s = 0.5$) at the interface of GDL-GFC which means half of the interface of GDL-GFC is covered with liquid water, figure 4.31 shows saturation liquid water distribution inside GDL. It has also same direction flow of saturated liquid water from CCL-GDL interface to GDL-GFC interface. In addition, saturation value increases overall in the GDL.

For a periodic function of $s = f(y) = \dfrac{1+\sin\left(\dfrac{n\pi y}{L}\right)}{2}$ where $n = 70$ pores at the interface of GDL-GFC, L = length of GDL and y is interface surface variable of GDL-GFC, figure 4.33 shows saturation liquid water distribution inside GDL.

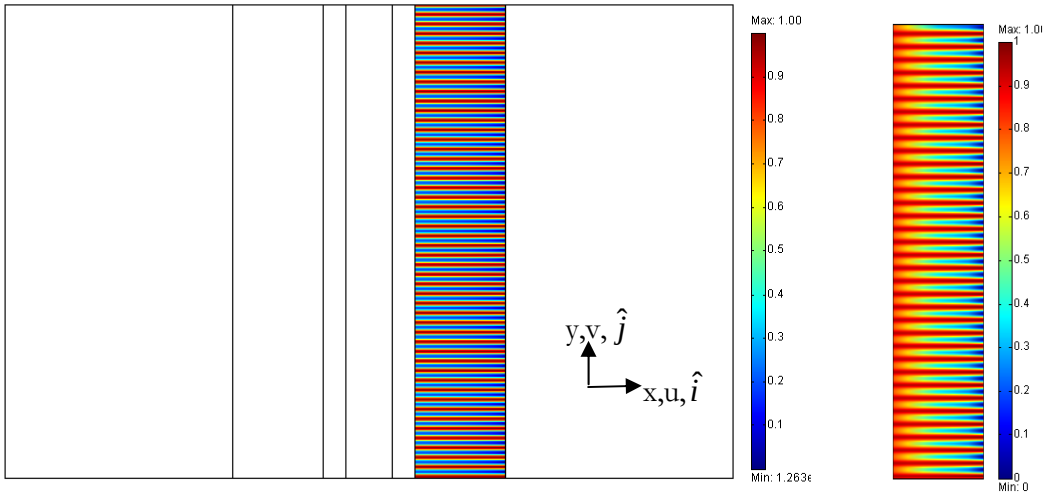

Figure 4.34: Saturation plot for a periodic function of s at the interface of GDL-GFC with contour plot using varying capillary pressure slope.

Figure 4.33 shows that due to periodic boundary condition at the interface of GDL-GFC liquid water saturation have higher value in particular pore sites where periodic function has higher amplitude values. However, lower saturation value in other pore sites where periodic function has lower amplitude values. These figures also indicates varying liquid water dispersions over GDL-GFC interface, which is reasonable as liquid water dispersion will vary due to liquid water generation at the

CCL-GDL interface and transportations through porous GDL. A contour plot, which is taken from the middle at the interface of GDL-GFC, is also shown. Contour plot indicates variation of saturation values non-rectangular shape at the interface of GDL-GFC due to periodic boundary condition.

Figure 4.34 shows that due to periodic boundary condition at the interface of GDL-GFC liquid water saturation have higher value in particular pore sites where periodic function has higher amplitude values. However, lower saturation value in other pore sites where periodic function has lower amplitude values. These figure also indicates varying liquid water dispersions over GDL-GFC interface, which is reasonable as liquid water dispersion will vary due to liquid water generation at the CCL-GDL interface and transportations through porous GDL. A contour plot, which is taken from the middle at the interface of GDL-GFC, is also shown. Contour plot indicates variation of saturation values non-rectangular shape at the interface of GDL-GFC due to periodic boundary condition.

Average value of saturation at the GDL subdomain for saturation value of zero (0) at the interface of GDL-GFC is 0.25, however average saturation value at the GDL subdomain for periodic function at the interface of GDL-GFC is 0.254193.

Average value of saturation at the GDL subdomain for saturation value of 0.5 at the interface of GDL-GFC is 0.501081, however average saturation value at the GDL subdomain for periodic function the interface of GDL-GFC is 0.500541.

Calculated average value of saturation at the GDL-GFC interface which is 0.497472. Value of this periodic function's average saturation at the interface of GDL-GFC indicates very much similar result for saturation value of 0.5.

Results indicate that uniform saturation value boundary condition can be assigned at the

interface of GDL-GFC to simplify the periodic boundary condition at the interface.

Coefficient of diffusivity for GDL, $c_D = \varepsilon^{1.5}$ Eq. (4.84)

Effect of saturation on porosity, $\varepsilon^* = \varepsilon(1-s)$ Eq. (4.85)

Therefore, coefficient of diffusivity for GDL while considering saturation,

$$c_D = [\varepsilon(1-s)]^{1.5} \quad \text{Eq. (4.86)}$$

Average coefficient of diffusivity, c_D is 0.0868 for periodic boundary condition and 0.0894 for saturation value of 0.5 at the interface of GDL-GFC. It seems like they are similar values. As comparing coefficient of diffusivity indicates uniformity at the boundary condition of GDL-GFC, so using uniform saturation boundary condition over the GDL surface is reasonable.

Figure 4.35 shows saturation distribution inside GDL indicating variation of saturation values. This plot indicates that depth of penetration of droplet is very near to GDL-GFC interface.

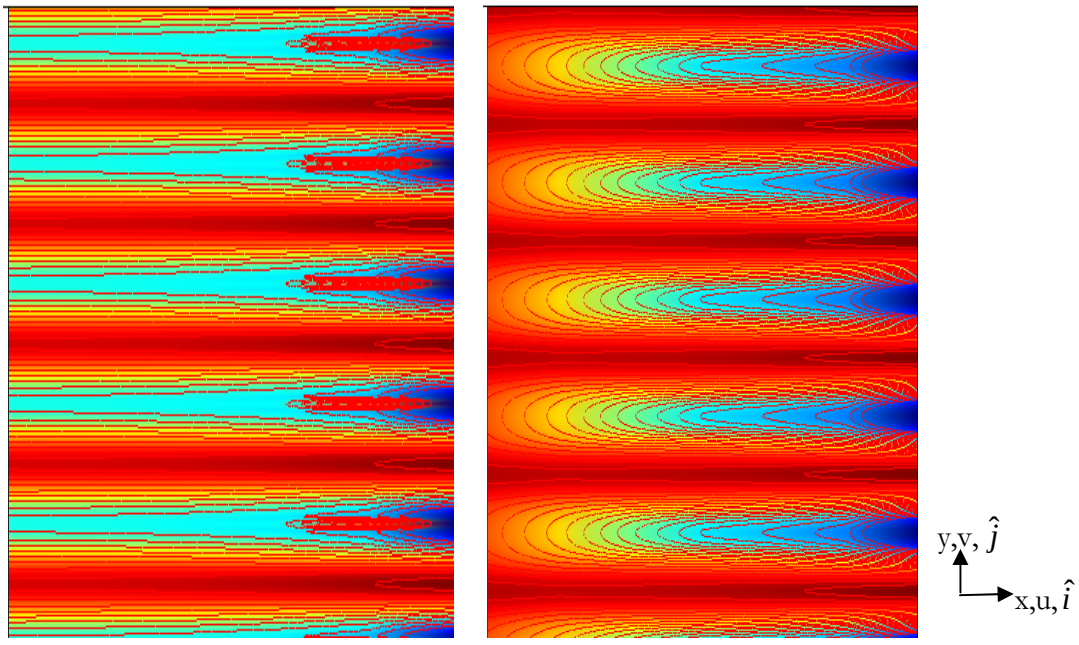

Figure 4.35: Saturation inside GDL for periodic boundary condition at the interface of GDL-GFC (a) constant (b) varying capillary slope.

4.4.1 Conclusion on Liquid Droplet Dispersion at the Interface of GDL-GFC

A two-dimensional (2D) PEMFC CFD model of water transport in the different parts of PEMFC and a single cathode side gas diffusion media of a PEMFC have been conducted. The gas phase transport model coupled to fuel cell electrochemistry and incorporated a predefined value of saturation. Later, the liquid phase transport model based on Darcy equation coupled with saturation-capillary pressure function (Leverett function) has also been conducted in relation with varying capillary pressure slope. A parametric study was conducted in which the GDL porosity was varied to simulate liquid saturation ranging from 0-50 percent. The results show that, at 50 percent saturation, the maximum current density is reduced roughly, by a factor of two. The results from the liquid water modeling suggest that for commonly used Leverett functions describing the saturation or capillary pressure relation, the saturation gradient through the GDL is relatively small and the GDL-GFC interfacial condition essentially determines the saturation value within the GDL. The results from the liquid water study with periodic boundary conditions show that the boundary effects permeate directly through the GDL with limited spreading in the down-the-channel direction. This behavior is consistent with the behavior expected in a thin, semi-hydrophobic GDL material. It is assumed that water dispersion that can be located from this simulation at the interface of GDL-GFC will eventually come to the gas flow channel. It is expected that, this prediction of water saturation inside GDL and at the interface of GDL-GFC could significantly help the operation of PEMFC in practical applications.

C H A P T E R - 5

CONCLUSIONS

This work has produced experimental and analytical tools to aid in the understanding of physical phenomena in Fuel cells. Experimental fixtures to characterize essential physical phenomena for water generation, saturation effect in fuel cell, poisoning, and thermal stress for SOFC manufacturing. Finally, 2D and 3D model for simplification of single channel fuel cell model, transient localized heating to the catalyst layer for CO recovery, thermal stress that developed during SOFC fabrication by High Temperature Vacuum Tube Furnace (HTVTF), and GDL-GFC interfacial conditions were developed. Furthermore, preliminary study on application of APS (Air Plasma Spray(APS) to SOFC and Anode and Cathode adhesion with electrolyte for the determination of parameters involve in manufacturing of components of fuel cell and anode and cathode adhesion with electrolyte that make manufacturing flexibility and adhesion of components of components of fuel cells.

The preliminary study on the air plasma-spray (APS) coating process have identified similarity in manufacturing of zirconia (ZrO_2) electrolyte membrane in SOFC. The XRD data revealed different phases of Al_2O_3 which in the same way can be analyzed for ZrO_2 electrolyte for SOFC.

The preliminary study on adhesion between anode and cathode with electrolyte have identified critical way to tackle adhesion. Microfabrication work has been proposed to deal with adhesion. Cleaning, microfabrication and groove on substrate surface and roughness have revealed possibility of better adhesion when it was deposited by APS alumina or zirconia coating.

The results of the gas flow channel configurations on three (3) designs of bipolar plates: Serpentine channel, Straight channel, and Interdigitated channel experiments successfully demonstrated that an interdigitated anode gas flow channel with a serpentine cathode gas flow

channel enhance performance of fuel cell. For this arrangement, the hydrogen is forced to flow inside the anode porous gas diffusion layer towards the reaction sites. The water flooding is partially eliminated by the using of serpentine bipolar plate in cathode side, due to the high flow speed and thus the capability of blowing the water droplets out of the cell.

The results of pulsed feeding channel pressure swing assessed mitigation of the CO poisoning. The effectiveness of these strategies is demonstrated through experimental work on a Fuel cell. By applying gas flow channel pressure swing, significant enhancement to the carbon monoxide tolerance level of PEMFC was found. These approaches could potentially eliminate the need for an expensive selective oxidizer. The CO poisoning process generally is slow and reversible. After applying a pulsed heating, the transient high temperature in the catalyst layer could help the recovery of the PEMFC from CO poisoning. By using gas flow channel pressure swing, oxygen can easily diffuse into the MEA from the outlet port and promote a quick recovery. Using these operational strategies, a PEMFC could operate continually using a high CO concentration fuel.

The numerical simulation results of single channel were quantified in terms of polarization curve, power density curve, water pattern by mass fraction, water partial pressure in the gas flow channel, fuel utilization rate under different reacting fluid flow rates. Both 2D and 3D simulations were performed. The 2D simulation is mainly used to obtain the detailed flow feature in the regions close to the electrolyte layer. The difference between 2D and 3D for the single channel design is found to be small. The simulation results were compared with the experimental measurements of a single channel PEMFC. The simulations have an agreement with the experimental data.

The simulation results of transient localized heating to the catalyst layer while maintaining the PEMFC membrane at a normal temperature (below 80°C) significantly enhances the carbon

monoxide tolerance level of PEMFCs. After applying a pulsed heating, the transient high temperature in the catalyst layer could help the recovery of the PEMFC from CO poisoning.

The numerical results of High Temperature Vacuum Tube Furnace (HTVTF) for manufacturing of different components of SOFC have revealed that lowering air flow rate and inserting a small pipe inside the first block to blow hot air on the second heat affected zone (HAZ-2) will reduce thermal stress generation inside the tube and eventual fracture of the vacuum tube. Mathematical models are developed to understand the effect of stress concentration arising due to thermal stresses in tube wall and heat-affected-zones (HAZ) of a HTVTF using multiphysics finite element software Comsol [Comsol User's guide (2005)]. Combination of thermal stress with temperature difference determine fracture region.

The simulation results of the transport of reactant and product gases and liquid water between the gas diffusion layer (GDL) and gas flow channel (GFC) have revealed that water dispersion from the GDL-GFC interface extends across the GDL to its other side, and eventually reduces the performance of the PEMFC. As an initial step in describing these transport processes, the gas transport and liquid transport are decoupled and analyzed separately. The model of gas transport processes is coupled to the fuel cell electrochemistry, and the resulting system of equations is solved, using predetermined values of liquid water saturation. The gas transport data obtained from this solution is compared with the established works of others. The liquid transport processes are modeled using the Darcy equation coupled with a saturation-capillary pressure function (the Leverett function) and assuming no phase change. In addition, the boundary conditions for the liquid transport equation are varied in order to show the extent of non-uniformities at the GDL-GFC interface.

C H A P T E R - 6

RECOMMENDATIONS FOR FUTURE WORK

This work has addressed physical phenomena for water generation, saturation effect in fuel cell, poisoning of catalyst layer, 2D and 3D model for simplification of single channel fuel cell model, transient localized heating to the catalyst layer for CO recovery, thermal stress that developed during SOFC fabrication by High Temperature Vacuum Tube Furnace (HTVTF), and GDL-GFC interfacial conditions from an experimental and analytical perspective. There have been significant research work already attempted and considerable progresses have been made. Based on the experience gained during the course of this work recommendations for future work can be made. The proposed future work includes potential improvements to the developed experimental fixtures, future experimentation to further contribute to the understanding of liquid water transport in PEMFCs, and future enhancements to the 2-D and 3D analytical model.

For application of APS to SOFC manufacturing experimental work several of improvements was not done in these areas: this method was used for alumina only, however the method was not used for zirconia that is the main materials for SOFC membrane.

For anode and cathode adhesion with electrolyte membrane, improvements can be done in these areas: due to lack of experimental facility of running, the alumina film over substrate materials and small load cell to measure adhesion by MTS testing machine.

For gas flow channel configurations, improvements can be done in these areas: optimized configurations are considered based on flow rate, water pattern formation and water vapor blowing to gas flow channel, percentage of water in the gas flow channel, steady and transient voltage-current data and different arrangements of three combinations of gas flow channels. However, several other ways optimization can be considered including variation of different kinds of membrane, different

dimension of gas flow channel, and different materials (especially metal) of gas flow channel.

For PEMFC poisoning and recovery, improvements can be done in these areas: depositing of Pt layer over membrane by sputter deposition, and opening and closing valve in the exit port of gas flow channel to control flow of gas based on poisoning.

For PEMFC single channel, improvements can be done in these areas: more fine elements can be considered during simulation, and different dimensions of gas flow channel.

For transient temperature during pulse heating in Fuel Cell poisoning analysis, more fine elements, and different shapes of elements can be considered.

For thermal stress in SOFC fabrication, only numerical simulation work has been done on tube however experimental result will solidify this concept.

For liquid droplet dispersion at the interface of GDL-GFC, no experimental work was done on this. Experimental work will enhance understanding of saturation results. Also transparent like glass made bipolar plate can help observing droplet formation and dispersion at the interface of GDL-GFC.

REFERENCES

1. American History, from http://americanhistory.si.edu/fuelcells/pem/pemmain.htm

2. Andruet R. H. (1998), Special 2-D and 3-D Geometrically Nonlinear Finite Elements for Analysis of adhesively Bonded Joints, Virginia Tech, Thesis, April,

3. ASTM standard tests

4. Badillo C. M., Ageorges H., Chartier T., Coudert J.F., Fauchais P. (2006), Preparation of LaMnO3 perovskite thin films by suspension plasma spraying for SOFC cathodes, Surface & Coatings Technology, 200, 3743 – 3756

5. Bellows R. J., Marucchi-Soos E. P., and Buckley D. T. (1996), Ind. Chem. Eng. Rev., 35, 1235.

6. Bellows R. J., Marucchi-Soos E., and Reynolds R. P. (1998), Electrochem. Solid-State Lett., 1, 69.

7. Benoveda N., Kesler O. (2009), Air plasma spray processing and electrochemical characterization of Cu–SDC coatings for use in solid oxide fuel cell anodes, Journal of Power Sources, 193, 454–46129.

8. Benyoucef A., Klein D., Coddet C., Benyouce B. (2008), Development and characterisation of (Ni, Cu, Co)-YSZ and Cu-Co-YSZ cermets anode materials for SOFC application, Surface & Coatings Technology, 202, 2202–2207

9. Bernardi D. M. and Verbrugge M.W. (1991), Mathematical model of a gas diffusion electrode bonded to a polymer electrolyte, AIChe Journal, 37, 1151-1163

10. Białucki P., Kozerski S. (2006), Study of adhesion of different plasma-sprayed coatings to aluminium, Surface & Coatings Technology, 201, 2061–2064.

11. Bird R. B., Stewart W. E. and Lightfoot E. N. (1960), Transport Phenomena, John Wiley & Sons,

12. Brandner M., Bram M., Froitzheim J., Buckremer H.P., Stöver D. (2008), Electrically Conductive Diffusion barrier layers for Metal-Supported SOFC, Solid State Ionics, 179, 1501–1504

13. Broka (1995), Characterisation of the components of the proton exchange membrane fuel cell, Techn Lic. Thesis, Royal Institute of Technology, Stockholm.

14. Caron N., Bianchi L., Me´thout and S. (2008), Development of a Functional Sealing Layer for SOFC Applications, Journal of Thermal Spray Technology, 598–602, Volume 17(5-6)

15. Catalyst and Surface Chemistry Lab (2009) from

http://catal.snu.ac.kr/research%20data/MCFC.htm

16. Changjing F., Kening S., Derui Z. (2006), Effects of La, Sro.2MnF(e) 03- Protective Coatings on SOFC Metallic Interconnects, Journal of Rare Earths, 24, 320 – 326

17. Chen B. (1999), Crack Path Selection in Adhesively Bonded Joints, Virginia Tech, Thesis, June,

18. Chen K.S., Kikner M.A. and Noble D. R. (2005), Simplified models for predicting the onset of liquid water droplet instability at the gas diffusion layer/gas flow channel interface, International Journal of energy research; 29:1113-1132

19. Cheng Y.L., Chen L.D., and Seaba J. P. (1999), Fuel Cell Power for Transportation, SAE, SP-1425, 55,

20. Comsol User's guide (2005), Chemical Engineering Module Model Library, Comsol Inc.

21. Coppo M. (2005), PhD thesis, Politecnico Di Torino (2005), Dipartimento di Energetica, April 13.

22. Crowe B.J. (1973), Fuel Cells: A survey, NASA Report no.SP-5115,Washington, DC

23. CSA company (2003), from http://www.spice.or.jp/~fisher/sofc.html#descript

24. Curtiss C. F., and Bird R. B. (1999), Multicomponent Diffusion, Ind. Eng. Chem. Res., pp. 2515-2522, vol. 38.

25. DeLuca S. J., Voorhees K. J. (1993), A comparison of products from an air atmosphere tube furnace with a vacuum Curie-point pyrolyzer: Implications for biodetection, Journal of Analytical and Applied Pyrolysis, Volume 24, Issue 3, Pages 211-225.

26. Demirbas A. (2002), Production of sodium carbonate from soda ash via flash calcination in a drop tube furnace, Chemical Engineering and Processing, Volume 41, Issue 3, Pages 215-221.

27. Deuflhard P. (1974), A modified Newton method for the solution of ill-conditioned systems of nonlinear equations with application to multiple shooting, Numer. Math., 22, pp. 289-315.

28. Dhar H.P., Christner L.G., Kush A.K. (1987), Journal of The Electrochemical Society, V 134, N 12, Dec, P 3021-3026

29. Dhar H. P., Christner L. G., Kush A. K., and Maru H. C. (1986), J. Electrochem. Soc., 133, 1574.

30. Fauchais P, Salas R E., Delbos C, Tognonvi M, Rat V, Coudert J F and Chartier T (2007), Suspension and solution plasma spraying of finely structured layers: potential application to SOFCs, J. Phys. D: Appl. Phys. 40, 2394–2406

31. Fauchais P., Salas R. E., Rat V., Coudert J.F., Caron N., and Te´ne`ze K. W. (2008), Parameters Controlling Liquid Plasma Spraying: Solutions, Sols, or Suspensions, Volume 17, page 31–59

32. Fehringer G., Janes S., Wildersohn M., Clasen R. (2004), Proton—conducting ceramics as electrode/electrolyte—materials for SOFCs: Preparation, mechanical and thermal-mechanical properties of thermal sprayed coatings, material combination and stacks, Journal of the European Ceramic Society, 24, 705–715

33. FEMLAB User's guide (2005), Chemical Engineering Module Model Library, Comsol Inc.,

34. Fogler H. S. (1999), Elements of chemical reaction engineering. Third edition, Printice Hall.

35. Fox A.C., Clyne T.W. (2004), Oxygen transport by gas permeation through the zirconia layer in plasma sprayed thermal barrier coatings, Surface and Coatings Technology, 184, 311–321

36. Fu C., Sun K., Chen X., Zhang N., Zhou D. (2008), Effects of the nickel-coated ferritic stainless steel for solid oxide fuel cells interconnects, Corrosion Science, 50, 1926–1931

37. Fu C.J., Sun K.N., Zhang N.Q., Chen X.B., Zhou D.R. (2008), Evaluation of lanthanum ferrite coated interconnect for intermediate temperature solid oxide fuel cells, Thin Solid Films, 516, 1857–1863

38. Fuel Cell Technologies, Inc. from
http://www.fuelcelltechnologies.com/fuelcell/products/single_cell_hardware.asp

39. Fukunaga H., Ihara M., Sakaki K., Yamada K. (1996), Relationship between overpotential and the three phase boundary length, Solid State Ionics, v 86-88, n pt 2, p 1179-1185

40. Futerko P. and Hsing I-M. (2000), Two-Dimensional Finite Element Method study of the Resistance of Membranes in polymer electrolyte fuel cells, Electrochimica Acta, 45, 1741-1751.

41. Gao W., Liao H.L., Coddet C. (2008), Plasma spray synthesis of $La_{10}(SiO_4)_6O_3$ as a new electrolyte for intermediate temperature solid oxide fuel cells, Journal of Power Sources, 179, 739–744

42. Gasteiger H. A., Markovic N. M., and Ross P. N. (1995), J. Phys. Chem., 99, 8290.

43. Gitzhofer F. and Jia L. (2008), Induction Plasma Technology Applied to Materials Synthesis for Solid Oxide Fuel Cells, Int. J. Appl. Ceram. Technol., 5 [6] 537–547

44. Goodman M., Trent, McNeil S.R., Zee J.W., Shimpalee V, Khan J. A. (2004), Effect of Bipolar Plate Cooling on Fuel cell heat generation, Proceedings of HT-FED04, 2004 ASME Heat Transfer/ Fluid Engineering Summer Conference, Paper no. HT-FED04-56707, July 11-15, Charlotte, North Carolina

45. Gottesfield S., Halpert G., and Landgrebe A. (1995), Vol. 95-23, pp.115-126

46. Grgur B. N., Markovic N. M., and Ross P. N. (1999), J. Electrochem. Soc., 146, 1613.

47. Guo S.M., Hasan A.B.M. (2009), ASME Journal of Fuel Cell Science and Technology, Vol.6, No.1, 011022.

48. Hasan A.B.M. (2005), LSU, Mechanical Engineering Department, Thesis, December.

49. Hasan A.B.M. (2007), M.Eng. Thesis, Virginia Tech.

50. Hasan A.B.M., Guo S.M., S.V.E. (2005), IMECE2005: ASME International Mechanical Engineering Congress and Exposition, Nov 5-11, Orlando, Florida. Paper No.: IMECE2005-81268, pp. 429-435

51. He W., Yi J. S.and Nguyen T. V. (2000), Two-phase flow model of the cathode of PEM fuel cells using interdigitated flow fields, AIChe Journal, 46, 2053-2063.

52. Hsing I.M., Futerko P. (2000), Two-dimensional simulation of water transport in polymer electrolyte fuel cells, Chemical Engineering Science, 55, 4209-4218

53. Huang Q.A., Berghuas J.O., Yang D., Yick S., Wang Z., Wang B., Hui R. (2008), Polarization analysis for metal-supported SOFCs from different fabrication processes, Journal of Power Sources, 177, 339–347

54. Huia R., Berghausb J.O., Petit C.D., Qua W., Yicka S., Legouxb J.G., Moreaub C. (2009), High performance metal-supported solid oxide fuel cells fabricated by thermal spray, Journal of Power Sources, 191, 371–376

55. Humfeld G. R. (1997), Mechanical Behavior of Adhesive Joints Subjected to Thermal Cycling, Virginia Tech, Thesis, February 7,

56. Hwang C., Tsai C.H., Lo C.H., Sun C.H. (2008), Plasma sprayed metal supported YSZ/Ni–LSGM–LSCF ITSOFC with nanostructured anode, Journal of Power Sources, 180, 132–142

57. Hwang C., Yu C. (2007), Formation of nanostructured YSZ/Ni anode with pore channels by plasma spraying, Surface & Coatings Technology, 201, 5954–5959

58. Inbody M. A., Vanderborgh N. E., Hedstrom J. C., and Tafoye J. I. (1996), Fuel Cell Seminar, P, 624

59. Johnson Matthey plc, History of Fuel Cells, Retrieved on 2007-05-27.

60. Ju H., Meng H., and Wang C.Y. (2005), A single-phase, non-isothermal model for PEM fuel cells, International Journal of Heat and Mass Transfer, Vol. 48, pp.1303-1315.

61. Kang H.K., Taylor P.R., and Lee J.H. (2003), Characterization of La0.8Sr0.2MnO3 Produced

by a Reactive DC Thermal Plasma Spray System, Plasma Chemistry and Plasma Processing, Vol. 23, No. 2, June

62. Khor K.A., Yu L.G., Chan S.H., Chen X.J. (2003), Densification of plasma sprayed YSZ electrolytes by spark plasma sintering (SPS), Journal of the European Ceramic Society, 23, 1855–1863

63. Kim S., Kwon O., Kumar S., Xiong Y., Lee C. (2008), Development and microstructure optimization of atmospheric plasma-sprayed NiO/YSZ anode coatings for SOFCs, Surface & Coatings Technology, 202, 3180–3186

64. Kim J.H., Songa R.H., Songa K.S., Hyunb S.H., Shin D.R., Yokokawa H. (2003), Fabrication and characteristics of anode-supported flat-tube solid oxide fuel cell, Journal of Power Sources, 122, 138–143

65. Kulikovsky A.A. (2003), Quasi-3D modeling of water transport in polymer electrolyte fuel cells, Journal of the electrochemical society, 150(11) A 1432-A1439

66. Kwon O., Kumar S., Park S., Lee C. (2007), Comparison of solid oxide fuel cell anode coatings prepared from different feedstock powders by atmospheric plasma spray method, Journal of Power Sources, 171, 441–447

67. Lang M., Franco T., Schiller G. and Wagner N. (2002), Electrochemical characterization of vacuum plasma sprayed thin-film solid oxide fuel cells (SOFC) for reduced operating temperatures, Journal of Applied Electrochemistry, 32: 871–874,

68. Larringz Y. and Norby T. (2000), Spinel and Perovskite Functional Layers Between Plansee Metallic Interconnect (Cr-5 wt % Fe-1 wt % Y2O3) and Ceramic (La0.85Sr0.15)0.91MnO3 Cathode Materials for Solid Oxide Fuel Cells, Journal of The Electrochemical Society, 147 (9), 3251-3256

69. Lee CI, Chu HS (2007), Effects of cathode humidification on the gas-liquid interface location in a PEM fuel cell, Journal of Power Sources, 161 (2): 949-956 OCT 27.

70. Lee W.K., Zee J.W. V., Murthy M. (2003), Fuel Cells, v 3, n 1-2, August, p 52-58

71. Li C.J., Li C.X., Long H.G., Xing Y.Z., Yang G.J. (2008), Performance of tubular solid oxide fuel cell assembled with plasma-sprayed Sc2O3–ZrO2 electrolyte, Solid State Ionics, 179, 1575–1578

72. Li C.J., Li C.X., Ning X.J. (2004), Performance of YSZ electrolyte layer deposited by atmospheric plasma spraying for cermet-supported tubular SOFC, Vacuum 73, 699–703

73. Li C.J., Li C.X., Xing Y.Z., Gao M., Yang G.J. (2006), Influence of YSZ electrolyte thickness on the characteristics of plasma-sprayed cermet supported tubular SOFC, Solid State Ionics, 177, 2065–2069

74. Li C.J., Li C.X., Wang M. (2005), Effect of spray parameters on the electrical conductivity of plasma-sprayed La1xSrxMnO3 coating for the cathode of SOFCs, Surface & Coatings Technology, 198, 278– 282

75. Li P. W., and Chyu M.K. (2004), Mass transfer Enhancement for Improving the Performance of Polymer Electrolyte Fuel Cells, Proceedings of HT-FED04, 2004 ASME Heat Transfer/ Fluid Engineering Summer Conference, Paper no. HT-FED04-56217, July 11-15, Charlotte, North Carolina

76. Li Z.Z., De-yuan L., Shui-yong W. (2006), High temperature performance of arc-sprayed aluminum bronze coatings for steel, Trans. Nonferrous Met. SOC. China, 16, 868-872

77. Lim C., Wang C.Y. (2004), Effects of hydrophobic polymer content in GDL on power performance of a PEM Fuel cell, Electrochimica Acta, 49, 4149-4156

78. Lim D.P., Lim D.S., Oh J.S., Lyo I.W. (2005), Influence of post-treatments on the contact resistance of plasma-sprayed La0.8Sr0.2MnO3 coating on SOFC metallic interconnector, Surface & Coatings Technology, 200, 1248–1251

79. Lu G.Q. and Wang C.Y. (2004), Electrochemical and flow characterization of a direct methanol fuel cell, Journal of Power Sources, 134, 33–40

80. Lounamaa N., Aass J. U., Kühne J. , Persson T. (1963), The elimination of the getter effect in the determination of gases in metals by the vacuum fusion method, Analytica Chimica Acta, Volume 29, Pages 267-271.

81. Marr C. and Li X. (1999), Composition and performance modeling of catalyst layer in a proton exchange membrane fuel cell, J. Power Sources, 77, 17-27

82. Materials properties data from www.matweb.com.

83. Mench M.M., Boslet S., Thynell S., Scott J. and Wang C.Y. (2001), Experimental Study of a Direct Methanol Fuel Cell, the 199th Electrochemical Society Meeting, Princeton, NJ.

84. Meredith R.E. and Tobias C.W. (1962), Conduction in heterogeneous systems. In: C.W. Tobias, Editor, Advances in Electrochemistry and Electrochemical Engineering, Interscience Publishers, New York.

85. Microelectronics Manufacturing from bmrc.berkeley.edu/courseware/ICMfg92/

86. MII Lecture (2007), Virginia Tech.

87. Mochida A., Kudo K., Mizutani Y., Hattori M., Nakamura Y. (1997), Transient heat transfer analysis in vacuum furnaces heated by radiant tube burners, Energy Conversion and Management, Volume 38, Issues 10-13, Pages 1169-1176.

88. Motupally S., Becker A. J., Weidner J.W. (2000), Diffusion of water in nafion 115 membranes,

J. Electrochem. Soc., 147, 3171-3177

89. Nam J. H., Kaviany M. (2003), Effective diffusivity and water-saturation distribution in single- and two-layer PEMFC diffusion medium, International Journal of Heat and Mass Transfer, 46, 4595-4611

90. NASA Glenn Research Center, from
http://www.grc.nasa.gov/WWW/Electrochemistry/images/fuel_cell.jpg

91. Nguyen T.L., Honda T., Kato T., Iimura Y., Kato K., Negishi A., Nozzki K., Shiono M., Kobayashi A., Hosoda K., Cai Z., and Dokiyab M. (2004), Fabrication and Characterization of Anode-Supported Tubular SOFCs with Zirconia-Based Electrolyte for Reduced Temperature Operation, Journal of The Electrochemical Society, 151 ~8! A1230-A1235,

92. Nie H., Huang W., Wen T.L., Tu H., Zhan Z. (2002), LSM cathodes for SOFC prepared by plasma spraying, Journal of Materials Science Letters, 21, 1951 – 1953

93. Nie H.W., Wen T.L., Tu H.Y. (2003), Protection coatings for planar solid oxide fuel cell interconnect prepared by plasma spraying, Materials Research Bulletin, 38, 1531–1536

94. Ning X.J., Li C.X., Li C.J., Yang G.J. (2006), Modification of microstructure and electrical conductivity of plasma-sprayed YSZ deposit through post-densification process, Materials Science and Engineering A, 428, 98–105

95. Ning X.J., Li C.X., Li C.J., Yang G.J. (2006), Effect of powder structure on microstructure and electrical properties of plasma-sprayed 4.5 mol% YSZ coating, Vacuum, 80, 1261–1265,

96. Nishida R., Kakinuma K., Nishino H., Kamino T., Yamashita H., Watanabe M., Uchida H. (2009), Synthesis of nickel nanoparticles supported on hollow samaria-doped ceria particles via the solution-spray plasma technique: Anode catalysts for SOFCs, Solid State Ionics, 180, 968–972

97. O'Hayre R., Cha S.W., Colella W., Prinz F. (2005), Fuel Cell Fundamentals, December.

98. Pissanetzky S. (1980), Numerical simulation of the transient temperature distribution inside a close-packed array of cylindrical tubes during heating and cooling under high vacuum, Nuclear Engineering and Design, Volume 56, Issue 2, February Pages 359-368.

99. Pissanetzky S., Cingolani H., Volpi R., Almagro J. C. (1981), Numerical simulation of the transient temperature distribution within the cladding material during annealing in a high vacuum furnace, Nuclear Engineering and Design, Volume 65, Issue 1, Pages, 141-150.

100. Prater K. B. (1994), Power sources, Vol.51, pp.129

101. Quad Group Inc.

102. Rose L., Kesler O., Tang Z., Burgess A. (2007), Application of sol gel spin coated yttria-stabilized zirconia layers for the improvement of solid oxide fuel cell electrolytes produced by atmospheric plasma spraying, Journal of Power Sources, 167, 340–348

103. Schiller G., Henne R.H., Lang M., Ruckdaschel R. and Schaper S. (2000), Development of vacuum Plasma sprayed thin-film SOFC for reduced operating temperature, Fuel Cells Bulletin No. 21

104. Schmidt V. M., Oetjen H.-F., and Divisek J. (1997), J. Electrochem. Soc., 144, L237.

105. Segall A.E. (2006), Manufacturing defects and the evidence of thermomechanical fatigue in a ceramic vacuum furnace tube, Engineering Failure Analysis, Volume 13, Issue 7, Pages 1184-1190.

106. Strumpf H. J., Stillwagon T. L., Kotchick D. M., Coombs M. G. (1988), Advanced industrial ceramic heat pipe recuperators, Heat Recovery Systems and CHP, Volume 8, Issue 3, Pages 235-246.

107. Song Y., Fenton J. M., Kunz R. H., Bonville L.J., Williams M.V. (2005), Journal of the Electrochemical Society, v 152, n 3, p A539-A544

108. Song Y., Xu H., Wei Y., Kunz R.H, Bonville L.J., Fenton J.M. (2006), Journal of Power Sources, v 154, n 1, Mar 9, p 138-144

109. Springer T.E., Wilson M.S., Gottesfeld S. (1993), Modeling and experimental diagnostics in polymer electrolyte fuel cells, J. Electrochem. Soc., 140 3513–3526.

110. Springer T.E., Zawodiski T.A., Gottesfield S. (1991), J. Electrochem. Soc., 136, 2334.

111. Su A., Weng F.B., Hsu C.Y., Chen Y.M. (2006), Studies on flooding in PEM fuel cell cathode channels, International Journal of Hydrogen Energy, Vol. 31, pp. 031-1039.

112. Surface engineering forum from http://www.gordonengland.co.uk/ps.htm

113. Suwanwarangkul R., Croiset E., Fowler M.W., Douglas P.L., Entchv E., Douglas M.A. (2003), Journal of Power Sources, 122 9-18,

114. Te´ne`ze K. W., Caron N., and Alexandre S. (2008), Gas Permeability of Porous Plasma-Sprayed Coatings, Volume-17, page 902–907

115. Ticianelli E.A., Derouin C.R., and Srinivasan S. (1988), J. Electroanal. Chem., 251, 275.

116. To´tha S., Fqlea M., Veresa M., Selmanb J.R., Arconc D., Po´ csika I., Koo´sa M. (2005), Influence of amorphous carbon nano-clusters on the capacity of carbon black electrodes, Thin Solid Films, 482, 207– 210

117. Um S. and Wang C. Y. (2000), Three dimensional analysis of transport and reaction in proton

exchange membrane fuel cells, in Proc. of the ASME Heat Transfer Division, Orlando, FL., Nov.

118. Um S., Wang C. Y. and Chen K. S. (2000), Computational fluid dynamics modeling of proton exchange membrane fuel cells, Journal of Electrochemical Society, Vol.147, pp4485-4493.

119. Urian R. C., Gulla A. F., Mukerjee S. (2003), Journal of Electroanalytical Chemistry, 554-555, 307-324

120. Vaßen R., Kaßner H., Stuke A., Hauler F., Hathiramani D., Stöver D. (2008), Advanced thermal spray technologies for applications in energy systems, Surface & Coatings Technology, 202, 4432–443

121. Waldbillig D., Kesler O. (2009), The effect of solids and dispersant loadings on the suspension viscosities and deposition rates of suspension plasma sprayed YSZ coatings, Surface & Coatings Technology, 203, 2098–2101

122. Waldbilling D., Kesler O. (2009), Characterization of metal-supported axial injection plasma sprayed solid oxide fuel cells with aqueous suspension plasma sprayed electrolyte layers, Journal of Power Sources, 191, 320–329

123. Wang Y. and Coyle T.W. (2008), Optimization of Solution Precursor Plasma Spray Process by Statistical Design of Experiment, Volume 17, page 692–699

124. Wang Y. and Coyle T.W. (2007), Solution Precursor Plasma Spray of Nickel-Yittia Stabilized Zirconia Anodes for Solid Oxide Fuel Cell Application, Journal of Thermal Spray Technology, 16, page 898–904

125. Wang Y. and Wang C. Y. (2007), Two-phase Transients of Polymer Electrolyte Fuel Cells, Journal of Electrochemical Society, Vol. 154, pp. B636-B643.

126. Wang Y. and Wang C.Y. (2005), Simulation of Flow and Transport Phenomena in a Polymer Electrolyte Fuel Cell under Low-Humidity Operation, Journal of Power Sources, Vol. 147, pp. 148-161.

127. Wang Z. H., Wang C.Y., and Chen K.S. (2001), Two-phase flow and transport in the air cathode of proton exchange membrane fuel cells, J. Power sources , Vol. 94.

128. Wasak H., Guo S.M., Turan A. (2005), the Ninth International Symposium on Solid Oxide Fuel Cells (SOFC IX), The 207th Meeting of The Electrochemical Society, Québec City Convention Centre, May 15-20,

129. Wantanabe M., Yamashita H., Chen X., Yamanka J., Kotobuki M., Suzuki H., Uchida H. (2007), Nano-sized Ni particles on hollow alumina ball: Catalysts for hydrogen production, Applied Catalysis B: Environmental, 71, 237–245

130. Weng F.B., Su A., Hsu C.Y., Lee C.Y. (2006), Study of water-flooding behavior in cathode

channel of a transparent proton-exchange membrane fuel cell, Journal of power sources.

131. White B.D., Kesler O. (2008), Implications of electronic short circuiting in plasma sprayed solid oxide fuel cells on electrode performance evaluation by electrochemical impedance spectroscopy, Journal of Power Sources, 177, 104–110

132. White B.D., Kesler O., Rose L. (2008), Air plasma spray processing and electrochemical characterization of SOFC composite cathodes, Journal of Power Sources, 178, 334–343

133. Wikipedia (2009) from http://en.wikipedia.org/wiki/Image:Alkalinecell.png

134. Wilson M.S., Springer T.E., Davey J. and Gottesfeld S. (1995), Alternative Flow-Field and Backing Concepts for Polymer Electrolyte Membrane Fuel Cells, Electrochemical Soc. Proc. Ed.

135. Xia W. S., Zhang H. O., Wang G. L. and Yang Y. Z. (2009), Functionally Graded Layers Prepared by Atmospheric Plasma Spraying for Solid Oxide Fuel Cells, Advanced Engineering Materials, 11, No. 1—2

136. Xing Y.Z., Li C.J., Li C.X., Yang G.J. (2008), Influence of through-lamella grain growth on ionic conductivity of plasma-sprayed yttria-stabilized zirconia as an electrolyte in solid oxide fuel cells, Journal of Power Sources, 176, 31–38

137. Yamaguchi I., Sohma M., Tsukada K., Kondo W., Kamiya K., Mizuta S., Kumagai T., Manabe T. (2006), Preparation of high-Jc Y123 films on CeO2-buffered sapphire substrates by MOD using a low-cost vacuum technique, Physica C: Superconductivity, Volumes 445-448, 1, Pages 603-607.

138. Yang Y.J., Wen T.L., Tu H., Wang D.Q., Yang J. (2000), Characteristics of lanthanum strontium chromite prepared by glycine nitrate process, Solid State Ionics, 135, 475–479

139. Yang Y.Z, Zhang H.O., Wang G.L., and Xia W.S. (2007), Fabrication of Functionally Graded SOFC by APS, Volume 16, page 768–775

140. Yang W., Li M. (2008), Effect of remelting process on characterization of air-plasma sprayed Fe67.5Ni23.5B9 alloy coatings onto 1Cr18Ni9Ti stainless steel, Journal of materials processing technology.

141. Yoon Y., Lee W.Y., Park G.G., Yang T.H., Kim C.S. (2004), Effects of channel configurations of flow field plates on the performance of a PEMFC, Electrochimica Acta, Vol.50, pp.709–712.

142. Zee J.W., Shimpalee V., Khan J.A. (2004), Effect of Bipolar Plate Cooling on Fuel cell heat generation, Proceedings of HT-FED04, ASME Heat Transfer/ Fluid Engineering Summer Conference, No. HT-FED04-56707, July 11-15, Charlotte, North Carolina.

143. Zhang B., Wang Y., Wang X., Chen X., Feng J. (1995), Determination of antimony, arsenic, bismuth, selenium, tellurium and tin by low pressure atomic absorption spectrometry with a quartz

tube fur. atomizer and hydride gener. with air add., Talanta, Volume 42, Issue 8, Pages 1095-1098.

144. Zhang C., Li C.J., Liao H., Planche M.P., Li C.X., Coddet C. (2008), Effect of in-flight particle velocity on the performance of plasma-sprayed YSZ electrolyte coating for solid oxide fuel cells, Surface & Coatings Technology, 202, 2654–2660

145. Zhang C., Li W.Y., Liao H., Li C.J., Li C.X., and Coddet C. (2007), Microstructure and Electrical Conductivity of Atmospheric Plasma-Sprayed LSM/YSZ Composite Cathode Materials, Volume 16, page 1005–1010

146. Zhang F.Y., Yang X.G. and Wang C.Y. (2006), Liquid Water Removal from a Polymer Electrolyte Fuel Cell, Electrochem. Soc., Volume, 153, Issue 2, pp. A225-A232

147. Zhu H., Kee R.J. (2003), A general mathematical model for analyzing the performance of fuel-cell membrane-electrode assemblies, Journal of Power Sources, Vol. 117, No. 1-2, pp. 61-74.

APPENDIX-A: PERMISSION

Permission Letter-1

From: Beth Darchi <DarchiB@asme.org>

Date: Tue, Dec 8, 2009 at 2:08 PM

Subject: permissions to add works

Dear Mr. Hasan:

It is our pleasure to grant you permission to use the following ASME papers:

- "Proton Exchange Membrane Fuel Cell High Carbon Monoxide Tolerance Operation using Pulsed Heating and Pressure Swing," by Guo, S.M, and Hasan, A.B.M., Journal of Fuel Cell Science and Technology, Vol. 6, No.1, 2009,
- "The Effects of Feeding Configurations to Water Flooding and General Performance of a Proton Exchange Membrane Fuel Cell," by Hasan, A.B.M., Guo, S.M., and Ekkad, S.V., IMECE2005: ASME International Mechanical Engineering Congress and Exposition, Vol. 45, pp. 429-435

cited in your letter for inclusion in a dissertation entitled EXPERIMENTAL AND NUMERICAL ANALYSIS OF FUEL CELLS to be published by Louisiana State University.

As is customary, we ask that you ensure full acknowledgment of this material, the author(s), source and ASME as original publisher on all printed copies being distributed.

Many thanks for your interest in ASME publications.

Sincerely,

Beth Darchi

Permissions & Copyrights

ASME, 3 Park Avenue

New York, NY 10016

T: 212-591-7700

F: 212-591-7841

E: darchib@asme.org

Permission Letter-2

From: Permissions Europe/NL <Permissions.Dordrecht@springer.com>

Date: Fri, Dec 11, 2009 at 7:50 AM

subjectRE: permissions to add works

mailed-byspringer.com

Dear Mr. Hasan,

With reference to your request (copy herewith) to reprint material on which Springer Science and Business Media controls the copyright, our permission is granted, free of charge, for the use indicated in your enquiry.

This permission

- allows you non-exclusive reproduction rights throughout the World.

- permission includes use in an electronic form, provided that content is

* at intranet;

- excludes use in any other electronic form. Should you have a specific project in mind, please reapply for permission.

- requires a full credit (Springer/Kluwer Academic Publishers book/journal title, volume, year of publication, page, chapter/article title, name(s) of author(s), figure number(s), original copyright notice) to the publication in which the material was originally published, by adding: with kind permission of Springer Science and Business Media.

The material can only be used for the purpose of defending your dissertation, and with a maximum of 40 extra copies in paper.

Permission free of charge on this occasion does not prejudice any rights we might have to charge for reproduction of our copyrighted material in the future.

Kind regards,

Estella Jap A Joe

Springer

Rights & Permissions

-

Van Godewijckstraat 30 | 3311 GX

P.O. Box 990 | 3300 AZ

Dordrecht | The Netherlands

fax +31 (0) 78 657 6377

estella.japajoe@springer.com

APPENDIX-B: LIST OF PUBLICATIONS ARISING FROM THIS RESEARCH

Journal Publications

1. Effects of Heat Affected Zones Temperature on the General Performance of High Temperature Vacuum Tube Furnace, Hasan, A.B.M., Wahab, M. A, and Guo, S.M., Journal of Structural Durability & Health Monitoring (SDHM), Vol.4, No.4, pp. 231-239, 2008

2. Proton Exchange Membrane Fuel Cell High Carbon Monoxide Tolerance Operation using Pulsed Heating and Pressure Swing**,** Guo,S.M, Hasan, A.B.M., ASME Journal of Fuel Cell Science and Technology, Vol.6, No.1, pp. 011022-1-6, 2009

3. Analysis of Fracture in High-Temperature Vacuum Tube Furnace, Hasan, A.B.M., Guo, S.M., and Wahab, M A, Journal of Failure Analysis and Prevention, Vol.9, No.3, pp. 262-269 , 2009.

4. Fuel Cell Performance Augmentation: Gas Flow Channel Design for Fuel Optimization, Hasan, A.B.M., Guo, S.M., and Wahab, M.A., Journal of Fluid Dynamics & Materials Processing (FDMP), Vol.5, No.4, pp. 399-409, 2009.

5. Behavior Analysis of a Prototypical Delayed Dynamical System, Hasan, A.B.M., Wahab, M. A, and Guo, S.M. (paper submitted to Journal of Computer Modeling in Engineering & Sciences)

Referred Conference Proceedings

1. Simulations of Dimensional Effects in Solid Oxide Fuel Cell, Hasan, A.B.M., Ekkad, S.V., and Mensah,P., HT2005: ASME Summer Heat Transfer Conference, San Francisco ,California, USA. July 17-22, 2005, Advanced Energy Systems Division, AES, Vol. 4, pp. 11-16, 2005

2. The Effects of Feeding Configurations to Water Flooding and General Performance of a Proton Exchange Membrane Fuel Cell, Hasan, A.B.M., Guo,S.M., and Ekkad, S.V., IMECE2005: ASME International Mechanical Engineering Congress and Exposition, Nov 5-11, 2005, Orlando, Florida, Vol. 45, pp. 429-435, 2005

3. Metal Surface Cleaning Using Electro-Plasma Process, David, R, Nettles, O, Liu, R, Hasan, A.B.M., Guo,S.M., and Wahab, M. A., Symposium of Fracture Mechanics of Welded Structures and Surface Coatings and Surface Cleaning Mechanics, First American Academy of Mechanics Conference, June 17-20, 2008, New Orleans, Louisiana.

4. Modeling of a Proton Exchange Membrane Fuel Cell, Hasan, A.B.M., Guo, S.M., Wahab, M.A.,The Seventeenth Annual International Conference on Composites/Nano Engineering (ICCE - 17), July 26 – August 1, 2009,Hawaii, USA.

VITA

A.B. Mahmud Hasan was born in Bangladesh. He is the youngest son of his parents, Late Alhaj Md. Habibur Rahman and Mrs. Begum Nurjahan. He completed his high school from Notre Dame College, Dhaka, Bangladesh. After successfully completing his high school study, he attended Bangladesh University of Engineering & Technology (BUET), where he received his Bachelor of Science degree in mechanical engineering in August 2001. After one year, working in BUET and another year in industry he entered a master's program of study at LSU in Fall 2003. After completion of that study, in Spring 2006 Hasan entered the graduate program in the Mechanical Engineering Department at Virginia Tech and completed another master's degree. Later Hasan entered in a doctoral program in LSU in Spring 2008 and hopes to complete it soon. Hasan also wrote some short stories in several magazines in his country.